

Scanning tunneling microscopy of single-molecule
magnets and hybrid-molecular magnets:
Two approaches to molecular spintronics

Inaugural-Dissertation

zur

Erlangung des Doktorgrades

der Mathematisch-Naturwissenschaftlichen Fakultät

der Universität zu Köln

vorgelegt von

Volkmar Heß

aus Erfurt

Köln 2016

Berichterstatte: PD Dr. Daniel Bürgler
(Gutachter)
Prof. Dr. Michely

Tag der mündlichen Prüfung: 25.01.2016

Kurzzusammenfassung

Die molekulare Spintronik vereint die Vorteile der Spintronik und der molekularen Elektronik in einem neuen Forschungsgebiet mit dem Ziel sowohl der Verbesserung bestehender als auch der Entwicklung neuartiger elektronischer Bauteile. Die Entwicklung und Untersuchung der Eigenschaften von molekularen Magneten und deren schlussendliche Verwendung in Bauteilen ist ein Hauptziel der molekularen Spintronik. Zwei verschiedene Arten von molekularen Magneten sind dafür aussichtsreiche Kandidaten: Einzelmolekülmagnete und molekulare Hybridmagnete. Beide stellen ideale Bausteine für Spintronikbauteile dar. Die Herstellung von Spintronikbauteilen erfordert die Abscheidung von molekularen Magneten auf Oberflächen. Da die Wechselwirkung zwischen Oberflächen und Molekülen jedoch hochkomplex ist, ist ein grundlegendes Verständnis dieser Phänomene unumgänglich für die erfolgreiche Verwendung von molekularen Magneten.

Um das Verständnis der Molekül-Oberflächen-Wechselwirkung zu verbessern, wurden beide Ansätze zu molekularen Magneten in dieser Dissertation untersucht. Da Oberflächen sehr anfällig für Verschmutzung sind, wurden diese Experimente im Ultrahochvakuum durchgeführt. Um bessere Einblicke in solche Systeme und deren Adsorptionseigenschaften zu erlangen, wurden ihre strukturellen, elektronischen und magnetischen Eigenschaften auf einer mikroskopischen Längenskala mit Rastertunnelmikroskopie (RTM) und -spektroskopie (RTS) untersucht.

Die Wechselwirkung zwischen Einzelmolekülmagneten und Oberflächen wurde exemplarisch an der Abscheidung von $\{\text{Ni}_4\}$ auf Au(111) untersucht. $\{\text{Ni}_4\}$ ist ein kürzlich synthetisierter Einzelmolekülmagnet mit einem kubanen $\{\text{Ni}_4^{\text{II}}(\mu_3\text{-Cl})_4\}$ Kern, welcher für die magnetischen Eigenschaften verantwortlich ist [1]. Der magnetische Kern wird von organischen Liganden mit einer Thioether-Funktionalisierung stabilisiert. Da Thioether-Funktionalisierungen in früheren Experimenten weitestgehend vernachlässigt wurden, wurde die Abscheidung von $\{\text{Ni}_4\}$ aus Lösung auf Au(111) und die daraus resultierenden Adsorptionseigenschaften mit RTM und Röntgenphotoelektronenspektroskopie (XPS) untersucht. Beide Methoden finden deutliche Indizien für eine Loslösung der Liganden vom magnetischen Kern während der Adsorption. Der magnetische Kern bleibt dabei jedoch möglicherweise strukturell intakt. Versuche, die losgelösten Liganden durch *in-situ* Anlassen zu desorbieren und den magnetischen Kern mit RTM abzubilden, waren nicht erfolgreich. Stattdessen führt das Anlassen zum Zerfall des magnetischen Kerns und zu sehr wahrscheinlich Schwefel induzierten Rekonstruktionen der Au(111) Oberfläche. Als ein Ergebnis dieser Untersuchung konnten neue Strategien vorgeschlagen werden, welche die Loslösung von Liganden in zukünftigen Experimenten verhindern.

In einem alternativen Ansatz wird die Wechselwirkung zwischen Molekülen und Oberflächen für die Entstehung von molekularen Hybridmagneten ausgenutzt. In diesem Ansatz können vergleichsweise stabile nichtmagnetische Moleküle verwendet werden. Die Wechselwirkung führt dann zu einem magnetischen Molekül-Oberflächen-Hybrid oder "molekularen Hybridmagneten".

Für das in diesem Fall benötigte magnetische Substrat wurde das gut verstandene Fe/W(110)-System ausgewählt und mit spinpolarisierter RTM (SP-RTM) charakterisiert. Die Herstellung von geeigneten magnetischen Spitzen für SP-RTM ist aufgrund der

schlechten Vorhersehbarkeit und Reproduzierbarkeit nicht trivial. Die Charakterisierung von SP-RTM Spitzen zeigte, dass Cr-bedampfte Spitzen die für nachfolgende Experimente benötigte Magnetisierungsrichtung aufweisen. Weiterhin wurde eine Spinpolarisation von bis zu 12,4 % für das Gesamtsystem Spitze-Probe nachgewiesen.

Triphenyl-Triazin (TPT) wurde exemplarisch für eine Studie zu molekularen Hybridmagneten ausgewählt. TPT besteht aus verschiedenen aromatischen Ringen, was im Zusammenhang mit der Entstehung von molekularen Hybridmagneten noch nicht untersucht wurde. Der erste Schritt in dieser Untersuchung ist die Bestimmung der Adsorptionsposition und -geometrie mithilfe von RTM. Ein Vergleich mit Dichtefunktionaltheorie (DFT) Simulationen, erstellt von Kollegen aus dem PGI-1, bestätigte, dass die experimentell gefundene Adsorptiongeometrie die höchste Adsorptionsenergie besitzt. Die elektronischen Eigenschaften von TPT auf Fe/W(110) wurden mit RTS untersucht und zeigen stark verbreiterte Zustände, was auf eine Chemisorption hindeutet. Anschließend wurde die spinabhängige Hybridisierung mittels SP-RTM untersucht. Dabei wird in Übereinstimmung mit DFT-Rechnungen eine stark orts- und energieabhängige Spinpolarisation des molekularen Hybridmagneten aufgedeckt. Die Resultate dieser Studie eröffnen neue Möglichkeiten zur Optimierung der Eigenschaften von organisch-ferromagnetischen Grenzschichten durch die Realisierung variierender Adsorptionsgeometrien.

Abstract

Molecular spintronics attempts both to improve the properties of current electronic devices and develop completely new devices by combining the advantages of molecular electronics and spintronics into one research field. Investigating and evaluating the properties of molecular magnets and to eventually employ them in devices is a major goal of molecular spintronics. Two different kinds of molecular magnets are promising candidates for device development: Single-molecule magnets (SMMs) and hybrid-molecular magnets. Both are ideal building blocks for spintronic devices, such as spin-transistors and spin-valves. However the fabrication of devices requires the deposition on surfaces. Due to the interaction between molecules and surfaces being highly complex, only a fundamental understanding of these phenomena will eventually lead to the successful application of molecular magnets in devices.

To improve the understanding of the molecule-surface interaction both approaches have been investigated experimentally in this dissertation. Since surfaces are prone to contamination, these experiments were conducted in ultra-high vacuum. To gain more insight in such systems and to understand the adsorption phenomena, their structural, electronic and magnetic properties were studied on a microscopic scale with scanning tunneling microscopy (STM) and spectroscopy (STS).

The interaction between SMMs and surfaces was exemplarily studied by depositing $\{\text{Ni}_4\}$ on Au(111). $\{\text{Ni}_4\}$ is a recently synthesized SMM where a cubane $\{\text{Ni}_4^{\text{II}}(\mu_3\text{-Cl})_4\}$ core is responsible for the magnetic properties [1]. The magnetic core is protected by organic ligands exhibiting a thioether surface functionalization. Since thioether functionalized ligands had been widely neglected in earlier experiments, the deposition of $\{\text{Ni}_4\}$ on Au(111) from solution and the resulting adsorption phenomena were studied by XPS and STM. Both methods revealed strong evidence for a ligand detachment during adsorption. The magnetic core however might be still structurally intact as indicated by XPS. Attempts to desorb the detached ligands and to subsequently image the magnetic core with STM by *in-situ* post-annealing were unsuccessful. Instead the post-annealing lead to the decomposition of the magnetic core and to a most likely sulfur induced reconstruction of the Au(111) surface. As a results of this study new strategies have been proposed to avoid the ligand detachment in future experiments.

In a complementary approach the interaction between molecules and surfaces is exploited for the formation of hybrid-molecular magnets. Here, comparatively stable non-magnetic molecules are deposited on magnetic surfaces. The interaction leads to a magnetic molecule-surface hybrid, or "hybrid-molecular magnet".

This approach requires a magnetic substrate. For this task the well known Fe/W(110) system was chosen and characterized by spin-polarized STM (SP-STM). The fabrication of suitable magnetic tips for SP-STM is a well known challenge due to its poor predictability and reproducibility. The characterization of tips was performed by SP-STM measurements on the Fe/W(110) system and reveals that Cr-coated tips exhibit the required out-of-plane magnetization direction for the following experiments on hybrid-molecular magnet systems. Furthermore an effective spin polarization of up to 12.4 % for the whole tip-sample tunnel junction was found.

For a study concerning the properties of a hybrid-molecular magnet system, triphenyl-

triazine (TPT) was chosen. TPT extends previous studies by exhibiting different aromatic rings in one molecule. As the first step of the investigation the adsorption position and geometry was determined by STM. A comparison with density functional theory (DFT) calculations made by colleagues from the PGI-1 confirms the experimentally found geometry to be highest in adsorption energy. The electronic properties of TPT on Fe/W(110) were investigated by STS and reveal highly broadened states, indicating a strong chemisorption. Finally, the spin dependent hybridization was studied by SP-STM. This study reveals a highly site and energy dependent spin polarization in good agreement with DFT calculations. The results of this study reveal a new route for designing the properties of organic-ferromagnetic interfaces by realizing varying adsorption geometries.

Contents

1	Introduction	1
2	Scanning Tunneling Microscopy	5
2.1	Modes of operation	5
2.2	The one dimensional tunneling effect	8
2.3	Perturbation theory approach	9
2.4	Scanning tunneling spectroscopy	10
2.5	Spin polarized tunneling	13
3	Molecular spintronics	17
3.1	Properties of molecules	19
3.1.1	Electronic properties	19
3.1.2	Magnetic properties of Single Molecule Magnets	20
3.2	Molecule-Surface Interaction	23
3.2.1	Adsorption phenomena	23
3.2.2	Molecules on magnetic surfaces	26
3.2.3	Experimental confirmation	28
3.2.4	SP-STM experiments of molecules on surfaces	31
3.3	Molecule deposition	33
3.3.1	<i>In-situ</i> techniques	33
3.3.2	<i>Ex-situ</i> techniques	33
3.4	{Ni ₄ } SMM	34
3.5	Triphenyl-triazine	36
4	Experimental methods	39
4.1	NSCT vacuum system	39
4.2	{Ni ₄ }/Au(111) sample preparation	41
4.2.1	Preparation of Au(111)	41
4.2.2	Deposition of {Ni ₄ }	42
4.3	TPT/Fe/W(110) sample preparation	42
4.3.1	Preparation of W(110)	42
4.3.2	Fe thin film depostion	43
4.3.3	TPT deposition	44

4.4	STM tip preparation	44
4.4.1	Tungsten tips	44
4.4.2	Tips for SP-STM	46
5	{Ni₄} on Au(111)	49
5.1	XPS results	50
5.1.1	As-deposited state	50
5.1.2	Post-annealed states	51
5.1.3	Decomposition upon in-situ post-annealing	54
5.2	STM results	55
5.2.1	As-deposited state	55
5.2.2	Post-annealing at 590 K	55
5.2.3	Post-annealing at 680 K	57
5.2.4	Structure models of the sulfur overlayers	58
5.3	Conclusion	60
6	Fe/W(110) imaged with SP-STM	61
6.1	Topography and growth of Fe/W(110)	62
6.2	Electronic and magnetic properties	63
6.3	Fe/W(110) imaged with different STM tips	66
6.3.1	Tips without magnetic sensitivity	66
6.3.2	Fe-coated tips	67
6.3.3	Cr-coated tips	68
6.4	Conclusion	73
7	TPT on Fe/W(110)	75
7.1	Adsorption of TPT on Fe/W(110)	76
7.1.1	Adsorption characteristics	76
7.1.2	Adsorption position and geometry	78
7.1.3	Comparison with DFT	80
7.2	Electronic properties of TPT/Fe/W(110)	82
7.2.1	Influence of adsorption orientation	83
7.2.2	Site dependent LDOS of TPT	84
7.2.3	Topography images and dI/dV maps	87
7.3	TPT on Fe/W(110) imaged by SP-STM	88
7.3.1	Spin dependent hybridization	89
7.3.2	Adsorption orientation of TPT in SP-STM	91
7.3.3	Possible interaction of chirality and magnetism	92
7.4	Energy and site dependent spin polarization	94
7.5	Conclusion	98
8	Summary and Outlook	101
	Appendices	105

A	107
A.1 Electrochemical analysis of a Ni ₄ -functionalized gold electrode	107
A.2 Domain wall fitting	108
A.3 Electronic properties of isolated TPT	110
A.4 Site dependent LDOS and PDOS of TPT/Fe/W(110)	111
9 Bibliography	113

Chapter 1

Introduction

In 1965 Gordon Moore made the observation that the integration density of circuits in computing hardware doubled roughly every two years. More than half a century "Moore's law" is still valid today, illustrating the enormous success of Si-based semiconductor technology. While this trend might hold up for a couple of more years, conventional Si-based semiconductor technology will inevitably hit a physical limit for miniaturization.

To satisfy the constantly increasing demand for computational power and storage capacity while reducing electrical power consumption at the same time, new technologies, phenomena and materials are currently explored. The further miniaturization of the so far very successfully employed top-down photolithography processes is limited by the wavelength of the used light. One promising approach for reaching smaller structures is assembling devices from molecular building blocks. The most obvious advantage of molecules is their small size of typically several nanometers. Significant progress has been made concerning the understanding of the electronic properties of molecules. Single molecules have been investigated in break junctions [2] and junctions grown by electromigration [3] and revealed interesting effects like Coulomb blockade or single atom Kondo effects [3]. Furthermore, molecular wires with appealing transport properties have been successfully synthesized [4] and highlight the possibilities of "molecular electronics".

The basically unlimited tuneability of molecules allows to integrate completely new or significantly improved functionalities into electronic devices. Molecules have been shown to work as light emitters [5], solar cells [6], gas sensors [7] or nano-magnets [8]. All these exciting properties are topped off with a low-cost and high-purity synthesis.

Another promising idea to extend current technology is to use the spin of electrons in addition to their charge as additional degree of freedom for information processing. This approach, named "spintronics", promises lower power consumption and the non-volatility of information stored in spins [8]. The field of spintronics originates from the discovery of the Giant magnetoresistance 1988 by Albert Fert [9] and Peter Grünberg [10]. This discovery led to the development of read-heads for hard disk drives which increased the density of storage media by several orders of magnitude. Due to the significance of their discovery Grünberg and Fert were awarded the Nobel prize in physics in 2007. Generally the aim of spintronics is to set, manipulate and detect the orientation of electron spins. Magnetic

materials are a cornerstone for spintronics since they can be used for all aforementioned tasks.

Molecular electronics and spintronics are not exclusive. In fact, the application of molecules in spintronics promises many advantages, such as high spin life times due to the low spin-orbit-coupling in organic molecules [11]. Thus eventually the field of "molecular spintronics" was born. One of the main quests in this field is this research area is the search for the smallest magnetic unit as building block for devices. Molecular spintronics offers two separate approaches for obtaining such nano-magnets.

The first approach employs molecules which exhibit magnetic properties by themselves. One class of molecules with interesting magnetic properties are single-molecule magnets (SMMs) [8]. SMMs are metal-organic compounds exhibiting both magnetic moment and anisotropy. Such molecules show a slow relaxation of the magnetization and below a certain temperature (*i.e.* the blocking temperature) behave similar to macroscopic magnets. Due to their size SMMs exhibit blocking temperatures up to a few 10 K and thus behave superparamagnetic at room temperature. Despite great efforts of chemists to synthesize SMMs with higher blocking temperatures, significant improvements are still elusive. Well known examples of SMMs are the archetypical Mn_{12} [12] and the late lanthanide doubledecker phthalocyanines such as TbPc_2 [13]. The appealing magnetic properties of SMMs make them ideal candidates for the realization of future technologies, particularly for quantum computing [14].

In order to use SMMs for devices, they need to be deposited on conductive electrodes. However, the interaction of molecules with surfaces is very complex and leads often to detrimental effects, such as decomposition or loss of magnetic properties [15]. In order for such approaches to eventually be implemented in real devices it is of utmost importance to understand adsorption and related phenomena.

The second approach for designing nano-magnets exploits the strong interaction between molecules and surfaces. Originally, the deposition of organic molecules on magnetic surfaces was studied as a means to design the electronic properties of organic-ferromagnetic interfaces [16]. Following experiments discovered that a strong interaction between molecules and magnetic surfaces leads to the formation of "hybrid-molecular magnets": molecule-surface hybrids with magnetic properties by themselves. The potential of this approach has been impressively demonstrated by magneto-transport measurements on molecule-surface hybrid systems at 250 K [17]. Since magnetic thin films exhibit significantly higher Curie temperatures than SMMs, devices operating above room temperature appear plausible. As such the second approach to molecular nano-magnets avoids the need for low temperatures of a few 10 K.

In the case of hybrid-molecular magnets the interaction between molecule and surface basically defines the properties of the hybrid. Consequently, understanding the interaction between molecules and surfaces and especially the spin dependent hybridization are important for the realization of hybrid-molecular magnets.

The benefits offered by the succesful realization of either approach seem tremendous. However, before the widespread application of molecules in spintronic devices is possible many challenges need to be overcome. As already insinuated perhaps the biggest obstacle is the controlled deposition of molecules on surfaces and understanding the resulting

interaction. The interaction between molecules and surfaces leads often to hybrids which do not show any resemblance to the previously separated systems. Finding and evaluating strategies for a controlled deposition of molecules on surfaces and predicting the results of the molecule-surface interaction are major goals of fundamental research.

This dissertation investigates the adsorption of two molecules on surfaces and the resulting interaction with scanning tunneling microscopy (STM). The two studied systems are

1. a SMM with the chemical formula $[\text{Ni}(\mu_3\text{-Cl})\text{Cl}(\text{HL}\cdot\text{S})]_4$ with $\text{HL}\cdot\text{S} = \text{C}_{11}\text{H}_{15}\text{NOS}$, abbreviated $\{\text{Ni}_4\}$, on Au(111) and
2. the polyaromatic non-magnetic triphenyl-triazine ($\text{C}_{21}\text{H}_{15}\text{N}_3$, abbreviated TPT) on Fe/W(110).

Each system exemplarily represents one of the approaches to nanoscopic magnets in molecular spintronics. By investigating the adsorption and the resulting phenomena on the microscopic scale new information is obtained for finding strategies to overcome the aforementioned obstacles. STM was chosen for investigating these systems since it is able to reveal the structural, electronic and magnetic properties of nanoscopic objects. The second chapter in this thesis describes the principles of STM operation and gives a theoretical background necessary for understanding later measurements.

Subsequently the third chapter introduces molecular spintronics in more detail: All concepts and mechanisms important for this thesis as well as deposition techniques for molecules are discussed. Furthermore, both molecules investigated in this thesis, $\{\text{Ni}_4\}$ and TPT, are introduced.

The fourth chapter discusses the UHV system used for the STM investigation and sample preparation. Additionally the sample preparation and STM tip preparation methods are presented.

The results of the $\{\text{Ni}_4\}$ deposition on Au(111) are presented in chapter 5. $\{\text{Ni}_4\}$ was synthesized by Kirill Monakhov from the Prof. Kögerler Group at RWTH Aachen university and Alessio Ghisolfi from the Prof. Braunstein group at university of Strassbourg [1]. Since $\{\text{Ni}_4\}$ uses a new type of surface functionalization, this study focusses on the adsorption characteristics and the resulting adsorption phenomena. The investigation was performed by a combination of STM and X-ray photoelectron spectroscopy (XPS).

For the formation of hybrid-molecular magnets, a magnetic substrate is required. Thus chapter 6 discusses the properties of the chosen Fe/W(110) substrate. It is an excellent substrate for SP-STM investigations due to its appealing electronic and magnetic properties. Furthermore, the SP-STM operation using Fe- and Cr-coated tips is established. The properties of these tips, such as magnetization direction and effective spin polarization, were characterized by the Fe/W(110) system.

The properties of TPT on Fe/W(110), a hybrid-molecular magnet system, are investigated in chapter 7. This chapter discusses the adsorption position and geometry, the electronic properties and the spin polarization of TPT on the double layer Fe/W(110). The results are compared with DFT calculations from Rico Friedrich, Vasile Caciuc and Nicolae Atodiresei from PGI-1 in the Forschungszentrum Jülich. The investigation of

TPT/Fe/W(110) reveals a new way for designing the properties of organic-ferromagnetic interfaces by realizing varying intra-molecular adsorption geometries.

Chapter 8 summarises the results of this thesis and gives an outlook for future experiments.

Chapter 2

Scanning Tunneling Microscopy

For a very long time in history, humans were limited to examine things with their eyes only. Things not visible to the naked eye simply remained inexplorable. This changed with the invention of optical microscopes, opening up whole new worlds to investigate and enabling many scientific breakthroughs. Unfortunately, due to the diffraction limit, technical limitations set aside, it is impossible to reach resolutions below 200 nm with conventional optical microscopes, leaving another fascinating world, the world of atoms and molecules, completely out of reach. This situation changed with the invention of the scanning tunneling microscope (STM) by Binnig and Rohrer in 1981 [18, 19]. Only five years later they were awarded the Nobel Prize in physics for their discovery. Since then, the idea of investigating surfaces by measuring the interaction between a sample and a probe has been extended to a multitude of other techniques.

2.1 Modes of operation

In STM the tunneling current between the sample and a probe is used to map the sample surface on an atomic level. A scheme of a typical STM setup is shown in Fig. 2.1. In order for tunneling to occur, the electrically biased probe, usually a sharp metallic tip, has to be brought very close to the sample surface. The tip is moved by high precision piezo elements (red), probes the sample surface by measuring the tunneling current.

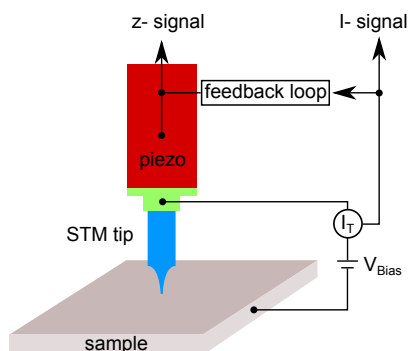


Figure 2.1: Schematic STM setup. An electrically biased tip (light blue) is brought very close to the sample (grey). The tip, being moved by high precision piezo elements (red), probes the sample surface by measuring the tunneling current.

piezo elements and probes the sample surface by measuring the tunneling current. The exponential relationship (derived in section 2.2) between tunneling current and distance between tip and sample allows the reconstruction of the sample surface from the magnitude of the tunneling current. Originally mainly used for investigating the topography, the possibility to probe the local density of states (LDOS) of a sample surface with extremely high spatial resolution is the main reason STM is still exceptionally powerful today.

The STM can be operated in different modes. To get a better understanding of STM functionality, the modes used during this work are explained in the following subsections.

Constant current mode

In constant current mode (CCM) a bias voltage V_{Bias} is applied to the tip and a setpoint value for the tunneling current I_{T} is defined. A feedback system is used to keep the tunneling current constant. If due to the topography of the sample or a change in the LDOS the current exceeds (drops below) the setpoint value, the tip is retracted from (brought closer to) the surface by high precision piezo elements. At every image point (x,y) the z -position (*i.e.* the height) of the tip is recorded. In a first approximation CCM images represent the sample topography. In the early stages STM was often used to determine the topography of sample surfaces. Most notably it revealed the structure of the peculiar Si(111) 7×7 reconstruction [20].

However, as will be shown in section 2.3, STM is not sensitive to the topography only but also to the LDOS. By keeping the current constant, STM measures actually isosurfaces of the LDOS near the Fermi level where all electronic states in the energy interval $[E_{\text{F}}; E_{\text{F}} + eV_{\text{Bias}}]$ contribute to the tunneling current.

Naturally, the LDOS is influenced by the sample topography, but especially for flat surfaces on atomic length scales, effects originating from a varying LDOS become more prominent and might not be of topographic origin. A typical example for this effect are oxygen adsorbates on metallic substrates: Although they are on top of the substrate they can appear as depressions. Images acquired in CCM will be referred to as topography images in this work.

Constant height mode

In constant height mode (CHM) a bias voltage V_{Bias} is applied to the tip and the surface is scanned without feedback loop at a constant height, while the change in current is recorded. Since samples are rarely completely flat, an electronic correction of the local sample slope is necessary. At every image point (x,y) the variation in tunnel current is recorded and used for reconstructing the sample surface. In contrast to CCM, the image is not taken at an isosurface of the LDOS, but at varying LDOS at the same tip-sample distance. Since no feedback is used, images in CHM can be acquired faster. CHM is only applicable to rather smooth surfaces. Thus, CHM is occasionally used to achieve extremely high resolution on nanoscopic objects (*e.g.* molecules or atomic resolution on surfaces). Due to its high sensitivity to thermal drift and piezo creep, CHM is limited to a narrow range of applications.

I(V) Spectroscopy

The possibility to resolve the sample LDOS on a sub-nanometer level in definable energy intervals is one of STMs biggest assets. The sample LDOS can be accessed by sweeping the bias voltage and recording the resulting tunneling current. The tunneling current as function of bias voltage $I(V_{\text{Bias}})$ gives information about the integrated density of states in the interval $[E_{\text{F}}; E_{\text{F}} + eV_{\text{Bias}}]$, similar to both previously mentioned operation modes. Direct access of the electronic states in a definable energy interval can be obtained by applying a small high-frequency AC modulation V_{mod} to the bias voltage and detecting the response via lock-in technique. The sampled energy interval is given by $[E_{\text{F}} + eV_{\text{Bias}} \pm eV_{\text{mod}}]$. The response of the lock-in amplifier corresponds to the n^{th} derivative of the tunneling current with respect to the bias voltage, where n is given by the detection of the n^{th} harmonic order of the modulation voltage. The first two derivatives are of special physical importance. The first derivative dI/dV gives insight into the differential conductivity, while the second derivative d^2I/dV^2 yields information about inelastic tunneling processes. During this PhD only the first derivative was detected. The physical foundation of scanning tunneling spectroscopy will be discussed in detail in section 2.4.

The spectroscopy functionality of the STM is typically used in two different ways:

1. Maps of differential conductivity
2. Point spectroscopy

Maps of differential conductivity (abbreviated: dI/dV maps) are recorded simultaneously to standard CCM or CHM images by lock-in technique and are used to image the spatial variation of the LDOS. A typical application of dI/dV maps is to spatially resolve certain electronic states, such as molecular orbitals.

dI/dV maps recorded in CCM reveal the differential conductivity in the energy interval $[E_{\text{F}} + eV_{\text{Bias}} - eV_{\text{mod}} : E_{\text{F}} + eV_{\text{Bias}} + eV_{\text{mod}}]$ measured on the isosurface defined by the bias voltage. dI/dV maps recorded in CHM show the LDOS at a certain tip-sample separation. CHM dI/dV maps are rarely used because a distinction between topographic and electronic features is generally not possible. Additionally the long integration time of lock-in amplifiers nullifies the speed advantage of CHM.

The ability to move the tip with sub-nanometer precision is exploited in the I(V) point spectroscopy mode. The tip is stabilized at a distance d between tip and sample, defined by V_{stab} and I_{stab} . After stabilizing the feedback loop is turned off and d is kept constant. Then the voltage is swept in defined bias window and the response, *i.e.* current and dI/dV signal, is recorded. This method reveals the energy resolved LDOS near the Fermi level at a well defined point. Therefore this method is ideally suited to investigate the electronic properties of nanoscopic objects, such as single atoms or molecules.

For all measurements presented in this thesis, the following parameters were used: $f_{\text{mod}} = 4111 \text{ Hz}$ and $V_{\text{mod,rms}} = 30 \text{ mV}$.

2.2 The one dimensional tunneling effect

The one dimensional tunneling effect occurring at a potential barrier can be used as a very simple approximation to describe the operation principle of STM. By using this simple model an expression for the tunnel current is derived showing the exponential relation on the tip-sample separation. Thus let us consider the following potential $V(z)$ [21]:

$$V(z) = \begin{cases} V_0 > 0 & \text{for } 0 < z < d \\ 0 & \text{else.} \end{cases} \quad (2.1)$$

A classical particle with the energy $E < V_0$ could not overcome this barrier and would be reflected as shown in Fig. 2.2a. In quantum mechanics however, due to the wave nature of matter, particles can penetrate the barrier and move into the third region (Figure 2.2b). To understand this phenomenon, let us consider an one dimensional Schroedinger equation:

$$\left[-\frac{\hbar^2}{2m} \frac{d^2}{dz^2} + V(z) \right] \varphi(z) = E\varphi(z) \quad (2.2)$$

The solutions of Eq. 2.2 are

$$\varphi(z) = \begin{cases} Ae^{+ikz} + Be^{-ikz} & \text{for region I} \\ Ce^{+\kappa z} + De^{-\kappa z} & \text{for region II} \\ Ee^{+ikz} & \text{for region III.} \end{cases} \quad (2.3)$$

with $k = \sqrt{2mE}/\hbar$ and $\kappa = \sqrt{2m(V_0 - E)}/\hbar$. The probability density to observe the particle at a point z in the classically forbidden region is proportional to $|\varphi(z)|^2 e^{-2\kappa z}$, which has a non-zero value and thereby confirms the possibility of quantum mechanic particles to penetrate or even cross (*i.e.* tunnel through) the barrier. The transmission coefficient T to tunnel through the barrier is defined as:

$$T = \frac{|E|^2}{|A|^2} \quad (2.4)$$

The coefficients in Eq. 2.3 can be found by evaluating boundary and consistency conditions. Under the assumption of a thick and high barrier ($\kappa d \gg 1$), which is reasonable for typical STM operation conditions, the transmission coefficient can be expressed as

$$T \approx \frac{16k^2\kappa^2}{(k^2 + \kappa^2)^2} \cdot e^{-2\kappa d} \quad (2.5)$$

In STM the barrier thickness d is the distance between tip and sample and the barrier height κ is the average work function of tip and sample. Since $I \propto T$, Eq. 2.5 shows that the tunneling current depends exponentially on the tip-sample distance. As a rule of thumb, if the distance is decreased by 1 Å (0.1 nm) the tunneling current increases by a factor of 10. This dependency explains the extremely high spatial resolution of STM down to several picometer. Furthermore it emphasizes the importance of the last atom of the tip, since it will contribute the most to the tunneling current.

This model, however, is a strong simplification as the electronic structure of both tip and sample have been neglected. By taking the electronic structure of tip and sample into account one can derive a more realistic STM model.

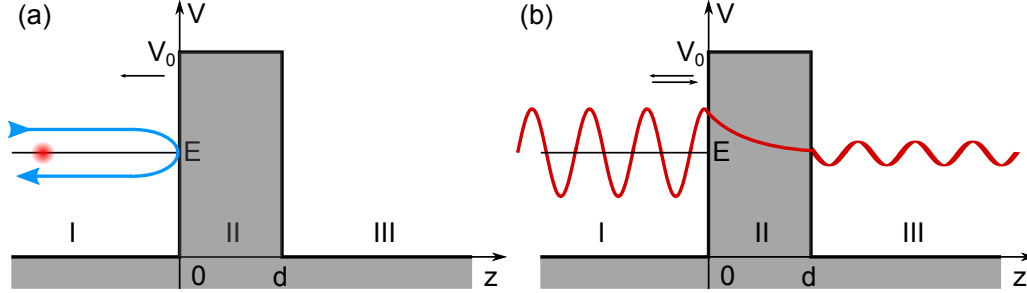


Figure 2.2: (a) A classic particle with energy $E < V_0$ can not pass the barrier (region II) and is reflected. (b) A quantum mechanics particle with energy $E < V_0$ has a certain non-zero probability to penetrate the barrier and reach region III by tunneling.

2.3 Perturbation theory approach

In 1961 Bardeen formulated a perturbation theory approach [22] to explain the observed tunneling effects in Giaever's metal-insulator-metal experiments [23]. This approach uses independent wavefunctions for both electrodes and the perturbation originates from the interaction of these two subsystems, rather than from an external potential. The transmission probability (similar to Eq. 2.4) between two planar electrodes with the wavefunctions Ψ_μ and Ψ_ν respectively is given by the tunneling matrix element:

$$M_{\mu\nu} = -\frac{\hbar^2}{2m} \int (\Psi_\mu^* \nabla \Psi_\nu - \nabla \Psi_\mu \Psi_\nu^*) dS \quad (2.6)$$

where the integration is performed over a separation surface between the electrodes. The elastic tunneling current at a bias voltage V , assuming low temperatures and $M_{\mu\nu}$ being constant in the investigated energy interval, can be found by integrating over all relevant states:

$$I = \frac{4\pi e}{\hbar} \int_0^{eV} \rho_\mu(E_F - eV + \epsilon) \rho_\nu(E_F + \epsilon) |M_{\mu\nu}|^2 d\epsilon \quad (2.7)$$

with $\rho_{\mu,\nu}$ being the density of states (DOS) of the electrodes. Applied to STM we get:

$$I \propto \int_0^{eV} \rho_T(E_F - eV + \epsilon) \rho_S(E_F + \epsilon) d\epsilon \quad (2.8)$$

with ρ_S (ρ_T) being the DOS of sample (tip). Eq. 2.8 lays the foundation of every realistic STM description since it shows that the tunneling current is proportional to the convolution of tip and sample DOS. The determination of $M_{\mu\nu}$ requires exact knowledge of the wavefunctions of both electrodes, which in STM is generally not possible. The tip DOS is

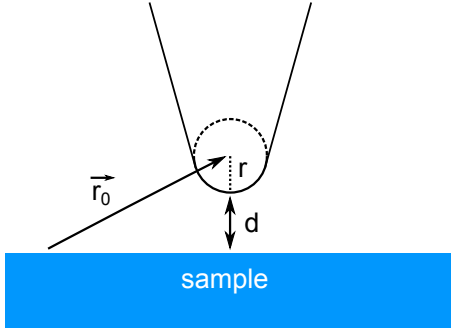


Figure 2.3: In the model of Tersoff and Hamann [24], the tip apex is approximated as a sphere of radius r . The tip is at a position \vec{r}_0 with a tip-sample separation d .

strongly influenced by the tip geometry which is rather irreproducible due to its fabrication process and is prone to changes during experiment.

In 1983 Bardeen's theory was expanded explicitly to STM by Tersoff and Hamann [24] by approximating the tip apex as a sphere with radius r (Fig. 2.3). Furthermore, the wavefunctions of the tip are assumed to be only s -waves and thus to exhibit no energy dependency for small bias voltages. As a result, the tunnel spectra are not affected by the tip and the tunneling current for a tip at position \vec{r}_0 can be expressed as:

$$I(\vec{r}_0, V) \propto V \cdot \rho_S(\vec{r}_0, E_F) \quad (2.9)$$

with ρ_S being the DOS of the sample. Eq. 2.9 implies that images recorded in the constant-current mode can be interpreted as isosurface of the sample LDOS ρ_S at the Fermi level.

As a result of the calculations of Tersoff and Hamann, STM should be able to achieve atomic resolution on surfaces with significant enough electronic corrugation. The experimentally observed corrugation of the Au(110) 2×1 and Au(110) 3×1 surface reconstructions [24] were successfully predicted by the Tersoff and Hamann model. However, also non-reconstructed atomically corrugated surfaces with small DOS corrugations, such as Al(111) [25], have been imaged by STM with atomic resolution. This behavior can be understood when considering that typical tip materials such as tungsten and platinum basically only have d -states at the Fermi level. These "spatially sharper" orbitals allow atomic resolution on materials with small electronic corrugation themselves. Since the assumption of only s -states contributing to the tip DOS made in Ref. [24] only holds to a limited degree, tunneling matrix elements for p - and d -states were later calculated by Chen [26].

2.4 Scanning tunneling spectroscopy

The ability of STM to probe the sample LDOS on a sub-nanometer level is a strong asset. To understand such spectra additional considerations are necessary. One important, so far neglected factor is the energy dependence of the tunneling transmission. In order to account for that Ukraintsev [27] introduced a transmission coefficient $T(E, V, S)$ into Eq. 2.8:

$$I \propto \int_0^{eV} \rho_T(E_F - eV + \epsilon) \rho_S(E_F + \epsilon) T(\epsilon, V, S) d\epsilon \quad (2.10)$$

T can be estimated for a trapezoidal barrier by using the semiclassical Wentzel-Kramers-Brillouin approximation:

$$T(E, V, d) \simeq \exp \left\{ -2d \left[\frac{2m}{\hbar^2} \left(\Phi + \frac{eV}{2} - (E - E_{||}) \right) \right]^{1/2} \right\} \quad (2.11)$$

with the average workfunktion $\Phi = (\Phi_t + \Phi_s)/2$ and the tip-sample separation d . Equation 2.11 shows that the transmission probability of the tunnel barrier exhibits an exponential dependence on the bias voltage V and total energy E . $E_{||}$ is the component of electron energy parallel to the junction interface and can be assumed to be neglectable small [27].

The implications of including this transmission coefficient in Eq. 2.10 are illustrated in Fig. 2.4. Tip and sample are represented by 1D energy diagrams and exhibit different work functions Φ_t and Φ_s respectively. According to previous assumptions the DOS of the tip is considered to be constant. The sample DOS is represented by the red curve. In Fig. 2.4a both systems are separated and do not interact with each other. In Fig. 2.4b, the tip is brought in to tunnel contact, which leads to an alignment of the Fermi levels of tip and sample. In Fig. 2.4c a negative bias voltage is applied to the tip. As a result electrons from the tip tunnel into unoccupied states of the sample. Fig. 2.4d depicts the case of a positively biased tip, where electrons from occupied states of the sample tunnel into the tip. In both cases, electrons close to the Fermi level of the negative electrode will contribute the most to the tunnel spectra (indicated by thicker arrows). This can be intuitively understood since they need to overcome a smaller energy barrier. Especially the case depicted in Fig. 2.4c is important for real STM experiments and will be discussed in the context of the TPT on Fe/W(110) in section 7.2.2. At negative bias voltages the influence of tip electronic states in tunnel spectra is significant larger then for positive bias voltages.

To deconvolute the sample DOS from the tip DOS the first derivative of Eq. 2.10 is analyzed [27]:

$$\begin{aligned} \frac{dI(V, S)}{dV} \propto & \rho_S(E_F - eV) \rho_T(E_F) T(eV, V, S) \\ & + \int_0^{eV} \rho_T(E_F + \epsilon) \rho_S(E_F - eV + \epsilon) \frac{d}{dV} T(\epsilon, V, S) d\epsilon \\ & + \int_0^{eV} \rho_T(E_F + \epsilon) T(\epsilon, V, S) \frac{d}{dV} \rho_S(E_F - eV + \epsilon) d\epsilon \end{aligned} \quad (2.12)$$

If we again assume a constant tip LDOS and a constant transmission coefficient in the investigated energy range only the first term of Eq. 2.12 is left and we obtain:

$$\frac{dI(V)}{dV} \propto \rho_S(E_F - eV) \quad (2.13)$$

Eq. 2.13 states that by measuring the dI/dV signal we gain direct insight into the sample LDOS. In contrast to Eq. 2.9, the validity of Eq. 2.13 is not restricted to small bias voltages. Although the previously made assumptions seem like gross oversimplifications, the experimentally obtained data confirms reasonably well this model. However, both neglected

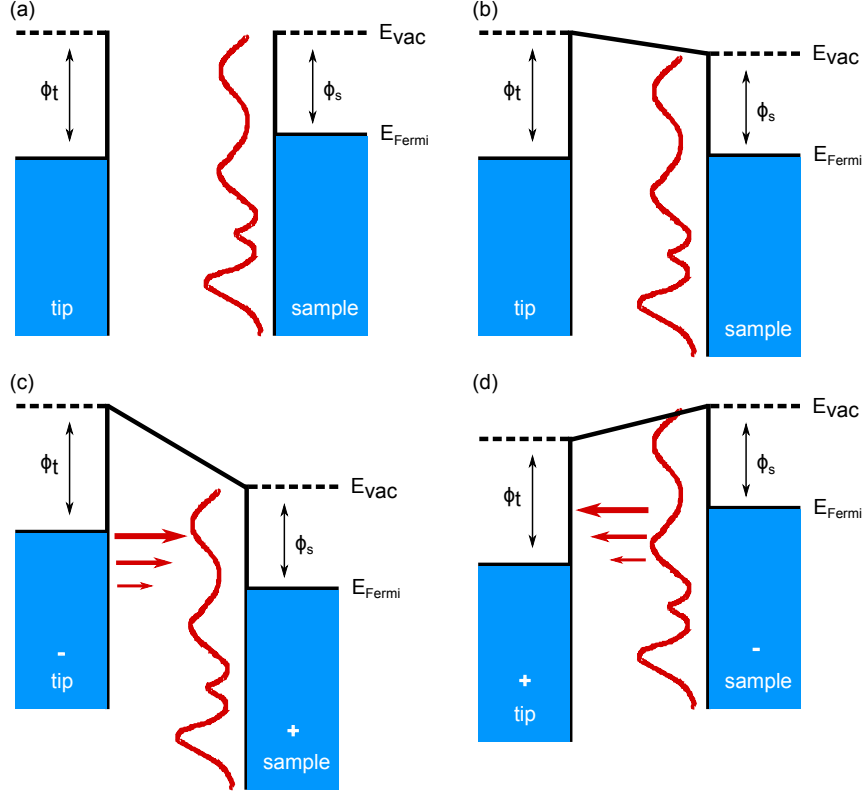


Figure 2.4: Scheme of the tunnel processes in a spectroscopy measurement. (a) depicts both electrodes as separate systems. (b) depicts both electrodes in contact and equilibrium. The Fermi levels are aligned. (c) A negative bias is applied to the tip. Electrons from the tip tunnel into unoccupied sample states (d) A positive bias is applied to the tip. Electrons from occupied sample states tunnel into the tip. Adapted from [28].

terms in Eq. 2.12 contribute as background to tunnel spectra. Several normalization methods have been developed to account for this problem [27, 29, 30]. An often used method for normalization is to divide the dI/dV signal by the I/V signal, as it gives a "relatively direct measure of the surface DOS" [30]. The qualitative character of measurements is however not affected by normalization, thus only raw spectra are presented in this thesis.

Experimentally the dI/dV signal is detected by lock-in technique. A small high-frequency AC modulation voltage V_{mod} is added to the bias voltage V_{Bias} . By using a Taylor series for the tunneling current we the following equation:

$$I(V_{\text{Bias}} + V_{\text{mod}}\cos(\omega t)) = I(V_{\text{Bias}}) + \frac{dI(V_{\text{Bias}})}{dV}V_{\text{mod}}\cos(\omega t) + \frac{d^2I(V_{\text{Bias}})}{2dV^2}V_{\text{mod}}^2\cos^2(\omega t) + \dots \quad (2.14)$$

The dI/dV signal is extracted by detecting the first harmonic with a lock-in amplifier.

2.5 Spin polarized tunneling

Up until now the spin of the electrons involved in the tunneling processes has been completely neglected. Magnetic materials exhibit a different DOS for each spin channel. The different DOS for both spin channels of 3d ferromagnets is explained by the Stoner criterion. The spin channels can be shifted with respect to each other if the increase in kinetic energy is compensated by a decrease in potential energy due to the exchange interaction (Fig. 2.5). The degree of difference of both DOS at a certain energy is measured by the spin polarization P :

$$P = \frac{\rho_{\uparrow} - \rho_{\downarrow}}{\rho_{\uparrow} + \rho_{\downarrow}} \quad (2.15)$$

with ρ_{\uparrow} (ρ_{\downarrow}) being the DOS of spin up (spin down) electrons.

Spin polarized tunneling was observed for the first time by Tedrow and Meservey in 1971 [31] between a magnetic and a superconductive electrode in a planar Al-Al₂O₃-Ni junction. The first transport experiments with two magnetic electrodes were conducted by Julliere in Fe/Ge/Co junctions in 1975 [32]. It was found that the tunneling current depends on the relative orientation of the magnetization of both electrodes. This effect is known today as "tunneling magnetoresistance" (TMR). Slonczewski [33] formulated the following expression for the TMR conductivity σ :

$$\sigma = \sigma_0(1 + P_S P_T \cos\theta) \quad (2.16)$$

P_T and P_S denote the polarization of both electrodes (in case of STM: tip and sample). θ is the angle between both electrode magnetization directions and σ_0 an average conductivity. Three cases are of special interest:

$$\sigma = \begin{cases} \sigma_0(1 + P_S P_T) & \text{for } \theta = 0^\circ \\ \sigma_0 & \text{for } \theta = 90^\circ \\ \sigma_0(1 - P_S P_T) & \text{for } \theta = 180^\circ \end{cases} \quad (2.17)$$

The conductivity is highest if the magnetization directions of both electrodes are aligned parallel and lowest for an antiparallel alignment. This behaviour is illustrated in Fig. 2.5, where two ferromagnetic electrodes are in tunnel contact and a bias voltage V is applied between them. Fig. 2.5a depicts the case of parallel alignment. The DOS of states for spin down (\downarrow) at the Fermi level in both electrodes is considerably higher than for spin up electrons (\uparrow). As a result the amount of initial and final states available for transport is high. Thus this orientation leads to a high current of spin down electrons. Conversely, the DOS at the Fermi level in both electrodes for spin up electrons is low and only a few initial and final states are accessible for transport. Therefore spin up electrons contribute significantly less to the total tunneling current.

In the case of antiparallel alignment (Fig. 2.5b), the DOS for spin down electrons is high in the first electrode but low in the second electrode. Although many initial states are available, the low amount of final states limits the tunnel current. Conversely for spin up the DOS in the first electrode is low but high in the second, resulting in few initial but

many final states. Therefore the tunneling current in both channels is small and the overall conductivity of the junction low.

If the magnetizations are orthogonal to each other, there will be no additional contribution to the tunnel current. All in all, Eq. 2.17 has an important implication for STM: Tip and sample ideally should have the same axis magnetization, since *e.g.* a tip with only in-plane components will not be able to investigate out-of-plane magnetic features of a sample.

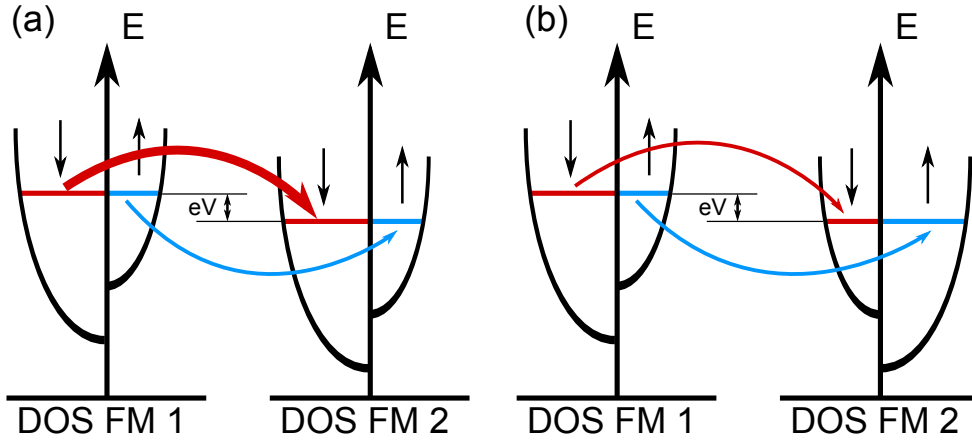


Figure 2.5: Schematic representation of the TMR effect. Tunneling occurs when a bias voltage V is applied to the second electrode. (a) The electrodes are aligned parallel. The DOS for spin down electrons at the Fermi level is significantly higher than for spin up electrons. There is a high tunnel current of spin down electrons, because much more initial and final states for transport are available (red arrow). (b) The electrodes are aligned antiparallel. The number of initial and final states is always high in one electrode but low in the other. Thus, the tunneling current is low for both spin species. As a consequence the total tunneling current is higher in a parallel configuration compared to an antiparallel configuration ($I_{\uparrow\uparrow} > I_{\uparrow\downarrow}$).

By using the parallel and antiparallel case in Eq. 2.17, we can define the effective polarization of the tunnel barrier:

$$P_{\text{eff}} \equiv P_S P_T = \frac{\sigma_{\uparrow\uparrow} - \sigma_{\uparrow\downarrow}}{\sigma_{\uparrow\uparrow} + \sigma_{\uparrow\downarrow}} \quad (2.18)$$

The previous considerations helped to understand spin-polarized tunneling and the TMR. However, to understand spin polarized tunneling in STM an extension of the Tersoff and Hamann model [24] is required. First we consider the energy integrated local density of states $\tilde{\rho}_S(\vec{r}_t, V)$:

$$\tilde{\rho}_S(\vec{r}_t, V) = \tilde{\rho}_{S,\uparrow} + \tilde{\rho}_{S,\downarrow} \quad (2.19)$$

and introduce the energy integrated local spin density of states $\tilde{m}_S(\vec{r}_t, V)$:

$$\tilde{m}_S(\vec{r}_t, V) = \tilde{\rho}_{S,\uparrow} - \tilde{\rho}_{S,\downarrow} \quad (2.20)$$

Both quantities are energy integrated in the interval $[E_F; E_F + eV]$. By assuming a constant, but non-zero tip spin density of states $m_T = \rho_{T,\uparrow} - \rho_{T,\downarrow}$ and LDOS $\rho_T = \rho_{T,\uparrow} + \rho_{T,\downarrow}$, as well as s -waves of the same decay length ($\kappa = \kappa_\uparrow = \kappa_\downarrow$), Wortmann *et al.* [34] were able to derive an equation for the tunneling current in SP-STM:

$$I(\vec{r}_t, V, \theta) \propto \rho_T \tilde{\rho}_S(\vec{r}_t, E_F + eV) + m_T \tilde{m}_S(\vec{r}_t, E_F + eV) \cos \theta(\vec{r}_t) \quad (2.21)$$

The first and second term in Eq. 2.21 denote the spin averaged and spin polarized tunneling current respectively. By using the definition for spin polarization P given in Eq. 2.15 we can rewrite Eq. 2.21 into:

$$I(\vec{r}_t, V, \theta) \propto I_0 \left[1 + \cos(\theta(\vec{r}_t)) P_T \tilde{P}_S(\vec{r}_t, E_F + eV) \right] \quad (2.22)$$

The first successful SP-STM experiment was conducted by Wiesendanger *et al.* 1990 [35]. They were able to detect alternating step heights on Cr(001) surface, which could be attributed to opposite out-of-plane magnetic domains on neighboring Cr(001) terraces. Starting from the Julliere expressions (Eq. 2.16 and 2.5) they derived an equation for the effective spin polarization:

$$P_{eff} \equiv P_T P_S = \frac{\exp(A\sqrt{\Phi}\Delta s) - 1}{\exp(A\sqrt{\Phi}\Delta s) + 1} \quad (2.23)$$

with the barrier height Φ , which for most metals is approximately 4 eV, an experimental constant $A \approx 1 \text{ eV}^{-1/2}/\text{\AA}$ and the height difference of opposite domains Δs . Wiesendanger *et al.* [35] observed a $\Delta s = 0.2 \text{ \AA}$, which yields an effective spin polarization of roughly 20 %.

Under certain circumstances the observation of a spin polarization in energy integrated STM operation modes, such as CCM, is challenging. If the integration is performed over many states with no or even opposite spin polarization the effective spin polarization can be largely diminished. Since dI/dV measurements can be performed in definable energy intervals, they are immensely helpful to reveal the magnetic properties of samples. By differentiation of Eq. 2.22 we get:

$$\frac{dI(\vec{r}_t, V, \theta)}{dV} \propto \rho_T \rho_S(\vec{r}_t, E_F + eV) + \cos \theta(\vec{r}_t) P_T P_S(\vec{r}_t, E_F + eV) \quad (2.24)$$

Similar to Eq. 2.22 the first part of Eq. 2.24 describes the spin averaged contribution and the second term the magnetic contribution. In Eq. 2.24 ρ_S and P_S are only evaluated in the energy interval $[E_F + eV_{\text{Bias}} - V_{\text{mod}}; E_F + eV_{\text{Bias}} + V_{\text{mod}}]$.

Due to all the previously mentioned possibilities, SP-STM is a very helpful tool to investigate the magnetic properties of samples. SP-STM played a crucial role in understanding many magnetic thin film systems, such as Fe/W(110) [36, 37], Fe/Ir(111) [38], Co/Cu(111) [37, 39] and Co/Ir(111) [37, 40]. Even more than standard STM, SP-STM depends on a skillful preparation of tips 4.4.2. Due to this, SP-STM is a very challenging experimental technique and only employed by a few groups worldwide on a regular basis.

Chapter 3

Molecular spintronics

The constant demand for increasing computational power and storage capacity while reducing electrical power consumption at the same time is a strong driving force in science and research. Spintronics is an approach to improve traditional electronics by using the electron spin as an additional degree of freedom for information processing. On a fundamental level the mechanisms of generating, manipulating and detecting spin polarized or pure spin currents are the main research areas in spintronics. Research on a more applied level focuses on the search and characterisation of suitable materials and the fabrication of devices.

The advantages of spintronic devices are manifold. One well known example (spintronic device) is magnetic random-access memory (MRAM), an alternative to dynamic random access memory (DRAM), which offers non-volatility of saved information and lower power consumption by writing data via spin transfer torque (STT). Today, several devices exploiting spintronic-based technologies are commercially available. Most notably among those are modern hard disk drives, which are based on the giant magnetoresistance effect (GMR), discovered independently by Peter Grünberg [10] and Albert Fert [9].

A fundamental problem in spintronics is the generation of spin polarized currents. Magnetic materials are a natural choice in this regard because their spin dependent density of states at the Fermi Level can result in spin polarized currents. Furthermore, various techniques have been investigated to generate spin polarized or pure spin currents in non-magnetic materials. One common and well understood technique is optical pumping, which uses circular polarized to selectively excite one spin species. Spin polarizations of up to 40 % have been achieved by optical pumping GaAs [41]. Other techniques include "spin pumping", where a magnetic material is excited with microwave radiation and the resulting precession induces a spin separation [42, 43] or using the spin Hall effect [44].

Due to these techniques the use of magnetic materials for spintronic devices is not a necessary requirement. However, the rich diversity of magnetic materials makes their use almost always beneficial. Moreover, the list of potentially suitable materials is still expanding and most recent additions include for example multiferroic insulators [45] or molecules [8, 11]. In fact the incorporation of molecules into spintronics appears so beneficial that it spawned its own scientific field: "molecular spintronics". Advantages for using

molecules in spintronic applications include the possibility of downscaling devices to the single nanometer-regime and the related significant improvement in energy efficiency.

On the quest to find the smallest possible magnet from which the fabrication of devices is reasonable, molecules appear as the most promising candidates. The major advantage to their competitors, single atoms and nanoparticles, lies in the high functionalizability of molecules. Magnetic molecules exhibit defined anisotropies. Furthermore the surface binding and spacing between molecules can be engineered by introducing suitable peripheral linkers. Especially in contrast to nanoparticles, molecules are additionally perfectly monodisperse. Atoms on surfaces have been successfully demonstrated as possible building blocks for all-spin logic gates [46], but lack the versatility of molecules. The fabrication of spintronic devices with molecules is possible via two approaches:

1. deposit magnetic molecules on non-magnetic surfaces or
2. deposit non-magnetic molecules on magnetic surfaces.

Before discussing the characteristics of each approach in detail, a fundamental understanding of the properties of molecules is required (section 3.1). Especially the electronic properties of molecules strongly influence the interaction with surfaces and are altered by it at the same time (section 3.1.1).

The next section (3.1.2) discusses the magnetic properties of "single-molecule magnets" (SMMs), which are an important class of molecules for the first approach. SMMs exhibit an intrinsic magnetic moment and anisotropy. Below their blocking temperature they behave similar to macroscopic magnets. This behaviour makes them an ideal building block for spintronic devices. In fact spin valves using TbPc₂ SMMs attached to a carbon nanotube between non-magnetic electrodes have already successfully demonstrated [47]. These exciting properties lead to an enormous scientific interest in SMMs [8, 11].

Regardless of the chosen route, the interaction between surface and molecule is always highly important since it can lead to considerably different properties of both the adsorbed molecule and the surface when compared to the separate systems. Therefore a basic understanding of the involved processes is necessary and is presented in section 3.2.1.

One problem inhibiting the widespread use of SMMs in spintronic devices is their low blocking temperature. The "drosophila" SMM, {Mn₁₂}, has a blocking temperature around 4 K [8], other SMMs like TbPc₂ reach up to 40 K [13]. Despite great efforts to synthesize SMMs with blocking temperatures closer to room temperature, no significant breakthroughs were achieved. The second, "reverse", approach was conceived to evade this problem by depositing non-magnetic molecules on magnetic materials, typically thin films. Magnetic thin films, depending on their thickness exhibit Curie temperatures ranging from 200 K for several layers thick films to well above room temperature for nm-thick films. In certain cases the interaction between molecule and surface leads to the formation of "hybrid-molecular magnets", which can have comparable properties to standard SMMs but exhibit clearly higher blocking temperatures. That this method is a viable approach has been impressively demonstrated by recent reports both experimentally [17] and theoretically [48]. The properties of such hybrid systems are analysed in section 3.2.2.

Another general problem both approaches are facing is the controlled deposition of molecules on surfaces. Since molecules exhibit widely varying properties, different depositing techniques have been developed. An overview of relevant techniques will be given in section 3.3.

The last sections in this chapter introduce the molecules investigated in this PhD thesis: the SMM $\{\text{Ni}_4\}$ complex in section 3.4 and the non-magnetic aromatic TPT in section 3.5.

3.1 Properties of molecules

This section gives an introduction into the electronic properties of molecules in general and the magnetic properties of a certain class of molecules, so called single-molecule magnets.

3.1.1 Electronic properties

The electronic properties of molecules are defined by wavefunctions, so called "molecular orbitals", which are associated with a discrete energy. As an approximation molecular orbitals can be obtained as linear combination of the atomic orbitals (LCAO method) of the atomic constituents of the molecule [49]. The electron wavefunctions of the atomic constituents A and B ($\Psi_{A,B}$) can either form a singlet ($\Psi_A - \Psi_B$) or triplet state ($\Psi_A + \Psi_B$). In the singlet case the resulting molecular orbital is lower in energy than both the constituents orbitals and thus has a "bonding" character. The bonding character is also confirmed by an increased charge density between the atoms involved in this bond. This behaviour is shown in Fig. 3.1 for the H_2 molecule.

Contrarily, in the triplet case the resulting molecular orbital will be higher in energy, thus an "antibonding" orbital is formed. A nodal plane separates the cores involved in the bond, where the wavefunction is zero. In the case of the H_2 molecule, the population of the antibonding orbital leads to dissociation of the bond.

The symmetry of the formed orbital is another important aspect. Two cases are of special relevance: σ -orbitals are formed if the resulting molecular orbital is symmetric under rotation about the internuclear axis. σ -orbitals originate from the overlap of two s -orbitals, two p_i -orbitals with i being an interatomic axis or any combination of atomic orbitals as long as the resulting molecular orbital is symmetric under rotation about the internuclear axis. Bonding σ -orbitals have no nodal plane, whereas antibonding σ -orbitals have one nodal plane perpendicular to the internuclear axis. The bonding and antibonding orbitals in Fig. 3.1 are typical examples for σ -molecular orbitals formed from two overlapping s -atomic orbitals.

In contrast, π -orbitals are non-symmetric under rotation about the internuclear axis. Bonding π -orbitals are separated by one nodal plane (along the internuclear axis), antibonding π -orbitals by two (one along and one perpendicular to the internuclear axis). π -bonds arise if two lobes of an orbital of one constituent overlap with two lobes of an orbital of the other constituent. Typically π -bonds are formed by the overlap of two p_i -atomic orbitals overlap, if i denotes an orbital perpendicular to the interatomic axis. In flat molecules, such as *e.g.* benzene, π -molecular orbitals are formed from the perpendicular to the molecular plane lying p_z -atomic orbitals.

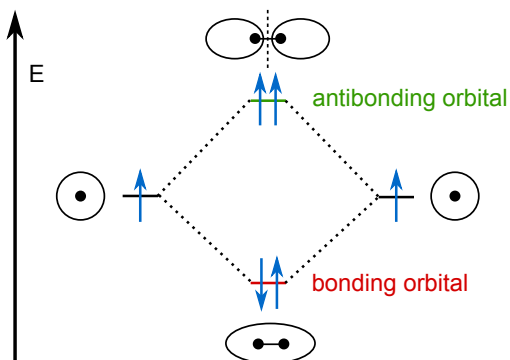


Figure 3.1: Formation of bonding and antibonding molecular orbitals illustrated for the H_2 molecule. The bonding orbital (red) is lower in energy than the groundstate level in the isolated atoms. The bonding orbital is characterised by an increased charge density between the H nuclei. Contrarily, the antibonding orbital (green) is higher in energy than the groundstate level in the isolated atoms. A nodal plane (dashed line), where the charge density is zero, separates both nuclei.

One important result from the symmetry is the spatial position of molecular orbitals. While σ -orbitals are located in the plane of a molecule, π -orbitals extend into the space perpendicular to the molecular plane¹.

Two molecular orbitals are of special significance when discussing the electronic properties of molecules: the "highest occupied molecular orbitals" (HOMO) and the "lowest unoccupied molecular orbitals" (LUMO). The HOMO and LUMO can be considered to be the molecular equivalents to the top of the valence and the bottom of the conduction band in solids. The energy gap between HOMO and LUMO is responsible for many physical properties of the molecule.

In comparison to molecules, metals have completely different electronic properties. They exhibit quasi continuous "band-like" energy levels and a high density of states at the Fermi Energy (E_F). As will be shown in section 3.2.1 many effects arise from the fundamental difference in the electronic properties of molecules and metals.

3.1.2 Magnetic properties of Single Molecule Magnets

Certain molecules exhibit intrinsic magnetic properties. Single molecule magnets (SMM) are a class of metalorganic compounds with an intrinsic magnetic moment, anisotropy and a slow magnetization relaxation at low temperatures. Below a characteristic temperature (*i.e.* blocking temperature) they behave similar to macroscopic magnets (*e.g.* showing an hysteresis curve). Due to their size of typically 1 to 10 nm, they additionally exhibit interesting quantum phenomena, such as the quantum tunneling of the magnetization. SMMs are envisioned to play a key part in the advancement of molecular spintronics, because they show great prospects as basic units for quantum information processing [14] or high density storage applications. To get more insight on the magnetic properties of SMMs let us consider a spin hamiltonian [8]:

$$\mathcal{H} = DS_z^2 + E(S_x^2 - S_y^2) + g\mu_B\mu_0\mathbf{S}\mathbf{H} \quad (3.1)$$

where S_x, S_y, S_z are the spin components, D and E are magnetic anisotropy constants and $g\mu_B\mu_0\mathbf{S}\mathbf{H}$ describes the Zeeman energy associated with the applied magnetic field \mathbf{H} .

¹This implies that in STM mostly π -orbitals will contribute to the tunnel current.

The energy landscape of a SMM with $D < 0$ and the easy axis lying along the z -direction is shown in Fig. 3.2a. For a magnetization reversal the spin has to climb up and down (indicated by green arrows in Fig. 3.2a) all $(2S+1)$ states of this double well-like potential with a total barrier height of DS_z^2 . Thus, the relaxation time follows a thermally activated law [8]. The average time τ_N between two magnetization reversals is defined as:

$$\tau_N = \tau_0 \cdot \exp\left(\frac{E_{\text{bar}}}{k_B T}\right) \quad (3.2)$$

with τ_0 being the attempt frequency (typically 10^9 s^{-1}), E_{bar} the barrier height for magnetization reversal, k_B the Boltzmann constant and T the measurement temperature. Only if the time necessary for a measurement τ_m is smaller than τ_N , measurements without thermally induced magnetization reversal processes are possible. The blocking temperature T_B is defined as the temperature where $\tau_m = \tau_N$:

$$T_B = \frac{E_{\text{bar}}}{k_B \ln\left(\frac{\tau_m}{\tau_0}\right)} \quad (3.3)$$

It is important to remember that T_B depends on the timescale of the measurement process, which can vary significantly for different techniques.

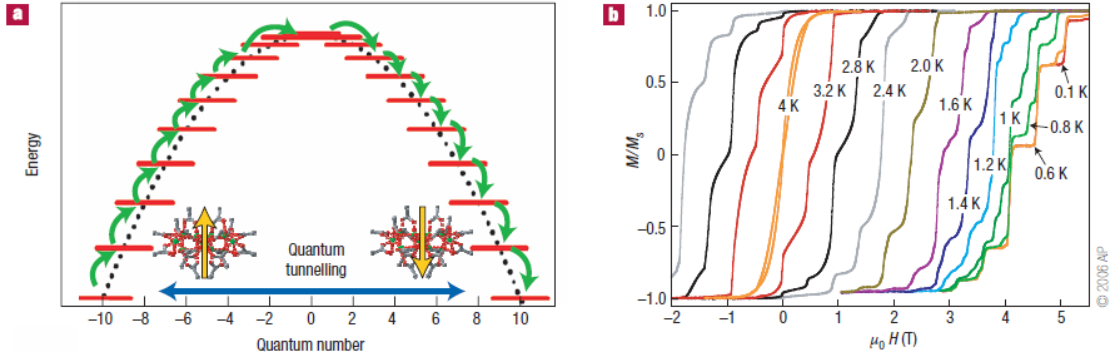


Figure 3.2: a) shows the double well-like potential typical for SMMs. Classically, to get from one side to the other some sort of external energy input, by *e.g.* phonon excitations, is necessary (indicated by green arrows), but in SMMs, due to their small size, tunneling between the levels can occur at resonant magnetic fields (indicated by blue arrow). b) shows the hysteresis curve of a crystallized $\{\text{Mn}_{12}\}$ SMM at low temperature. The sweep rate of the magnetic field is kept constant at 2 mT s^{-1} . At 4 K the hysteresis curve starts to open and widens with decreasing temperature. Below 1 K, indicated by the black arrows, quantum tunneling of the magnetization is observed. Taken from [8].

Fig. 3.2b shows the hysteresis curve of a crystallized SMM. At 4 K (at a magnetic field sweep rate of 2 mT s^{-1}) the relaxation is slow enough that a hysteresis curve can be observed. With decreasing temperature the hysteresis curve widens. The small size of SMMs gives rise to an additional magnetization reversal process by tunneling. The energy

levels in Fig. 3.2a shift in respect to each other if an external magnetic field is applied. For certain magnetic fields (*i.e.* resonance fields) the levels align properly and the magnetization can reverse by tunneling (blue arrow in Fig. 3.2a). This phenomenon was experimentally confirmed by the observation of sudden changes in the hysteresis curve below 1 K, indicated by the black arrows in Fig. 3.2b.

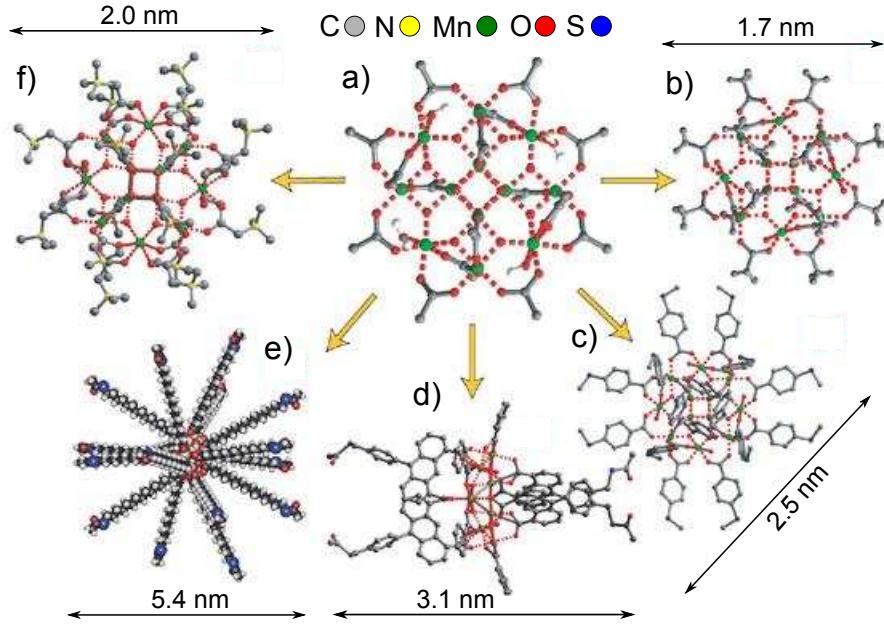


Figure 3.3: Overview of $\{\text{Mn}_{12}\}$ complexes with different ligands for surface functionalization. a) shows the bare magnetic functional unit $[\text{Mn}_{12}\text{O}_{12}(\text{CH}_3\text{COO})_{16}(\text{H}_2\text{O})_4]$ with very basic, minimal ligands. b)-f) show different ligands attached to Mn_{12} , highlighting the extreme functionalizability of molecules. b) shows the original Mn_{12} synthesized in [50]. Chemical formulas for b)-f) can be found in [8]. Taken from [8].

The first molecule synthesized with SMM properties was the $\{\text{Mn}_{12}\}$ compound in 1980 [50]. $\{\text{Mn}_{12}\}$ has 8 Mn^{III} ions with $S = 2$ and 4 Mn^{IV} ions with $S = 3/2$. The Mn^{III} and Mn^{IV} ions couple antiferromagnetically, resulting in a spin groundstate of $M_S = 10$. The functional unit, the magnetic core, of $\{\text{Mn}_{12}\}$ is shown in Fig. 3.3a. Attached to the central functional unit are suitable organic linkers, so called "ligands". Ligands help stabilizing the functional unit and can be tailored to exhibit other desired properties. Typically, ligands exhibit a surface functionalization in order to deposit SMMs on surfaces in a controlled way. The ligands are usually only modified in the periphery in order to avoid changes to coordination sites. Fig. 3.3b-f shows examples of $\{\text{Mn}_{12}\}$ with different ligands and emphasizes one of the major advantages of SMMs when compared to single atoms on surfaces as smallest magnets from which the fabrication of devices is possible. This high functionalizability allows to tailor molecular properties according to the desired

application. A more detailed discussion of the problems related to the successful deposition of molecules on surfaces and how to select an appropriate ligand is given in section 3.3. A major part of the investigation of $\{\text{Ni}_4\}$ in chapter 5 is related to this problem.

3.2 Molecule-Surface Interaction

Understanding the molecule-surface interaction is very complex, but crucial for the development of molecular spintronic devices. Thus considerable scientific work has been aimed to improve the understanding of these phenomena. This section provides the necessary background for understanding the experiments described in chapter 5 and 7 and gives an overview over important work already performed in this particular area.

3.2.1 Adsorption phenomena

In order to use molecules as building block in electrical devices, molecules need to be deposited on conductive surfaces. Thus it is necessary to study the adsorption phenomena of molecules on conductive surfaces. As illustrated in section 3.1.1 the electronic properties of molecules and metals are completely different. Molecules exhibit discrete molecular orbitals, whereas metals have quasi-continuous band like states. A schematic of both separated systems is shown in Fig. 3.4a.

When a molecule adsorbs on a metal surface both systems will interact with each other. Two main consequences (Fig. 3.4d) arise from this interaction [51]:

1. The previously infinite lifetime (τ) of the molecular state is now finite. This leads to a broadening of $\Gamma \approx \hbar/\tau$ of the molecular state.
2. The molecular energy level shifts from its isolated gas-phase value ϵ_0 to ϵ_{eff} . Among other factors the metal DOS determines the size of the shift [51, 52].

The strength of the interaction depends on both the properties of the molecule and the surface. Generally, one distinguishes between two cases: physisorption (weak interaction) and chemisorption (strong interaction).

In physisorption (Fig. 3.4b), long-range attractive van der Waals (vdW) forces are responsible for the molecule-surface-bond [53] which result in a weak interaction between both systems. The properties of molecule and surface are only slightly changed. The molecular orbitals are broadened to some degree (*i.e.* Γ is small) but retain their discrete character. On polarizable surfaces, due to the additional adsorbate-substrate image potential, an HOMO-LUMO gap renormalization can occur [54, 55].

In contrast, chemisorption (Fig. 3.4c) is characterized by a strong chemical bond between molecule and surface. The increased interaction between molecule and substrate leads to the formation of a new quantum mechanical system in which hybrid adsorbate-surface states are formed (*i.e.* Γ is large). The DOS of the hybrid is defined by mixed electronic states without any resemblance to the states of the separated systems [56, 57]. The resulting hybrid states are usually strongly broadened and have no molecular character anymore. It

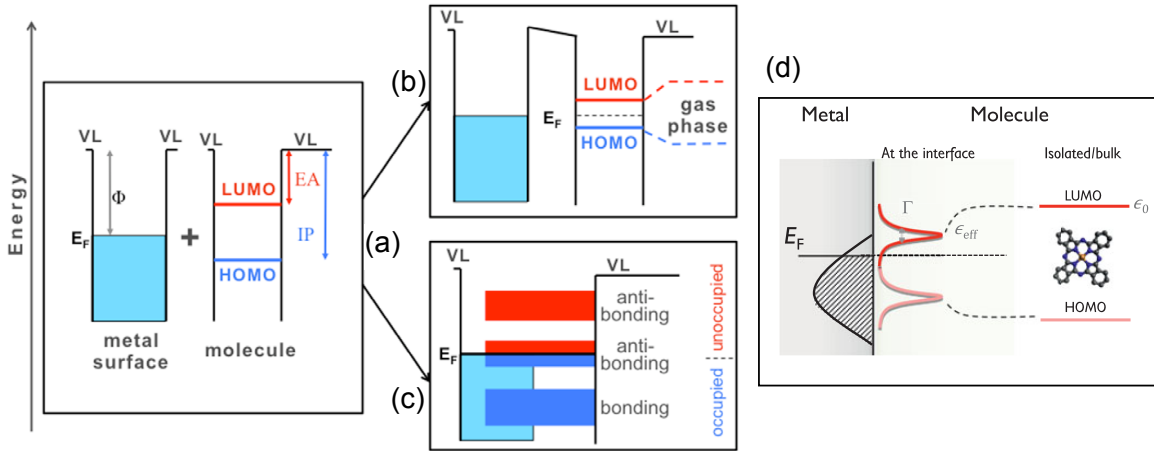


Figure 3.4: Molecule surface interaction: a) shows both isolated systems with EA: electron affinity, IP: ionization potential, VL: vacuum level. b) depicts the physisorption case: HOMO and LUMO are slightly broadened and move closer to the Fermi energy. c) depicts the chemisorption case: molecular orbitals and substrate states hybridize and form new strongly broadened states. The original molecular-like character vanishes. d) showcases the two general consequences of molecule-surface interaction: a shift and broadening of molecular energy levels. a)-c) taken from [49], d) taken from [51].

is important to keep in mind that also the surface atoms involved in the chemical bond with the molecule may have significantly altered properties.

Furthermore, during chemisorption other additional effects like electron transfer or straining intramolecular bonds can take place, further affecting the electronic properties of the hybrid. These effects can be detrimental (*e.g.* molecular decomposition, loss of certain properties) or beneficial (*e.g.* by forming hybrid-molecular magnets or leading to interfaces with high spin polarization).

As a rule of thumb the adsorption energy gives a good indication of the interaction strength in an adsorption process. For small molecules, such as benzene or cyclooctatetraene, physisorption is characterized by adsorption energies around 100 meV and chemisorption above 1 eV.

Due to the rich fundamental physics involved, but also as necessary step for device development, the interaction between molecules and surfaces has attracted a lot of scientific interest. Exemplarily, one comprehensive study investigated the adsorption characteristics of cyclooctatetraene (COT) on different surfaces both experimentally and by density functional theory (DFT) simulations [58]. COT is an organic non-aromatic molecule consisting of a ring of eight carbon atoms which is buckled in gas phase. The coinage metals gold, silver and copper were chosen as substrates because they can be considered representative for materials with different reactivity.

For COT on Au(111) DFT calculations (Fig. 3.5c-e) yield a low adsorption energy of 162 meV. COT adsorbs in a non-flat adsorption position, similar to its gas phase geometry, with a molecule surface separation of 2.86 Å. The density of states (DOS) of COT on

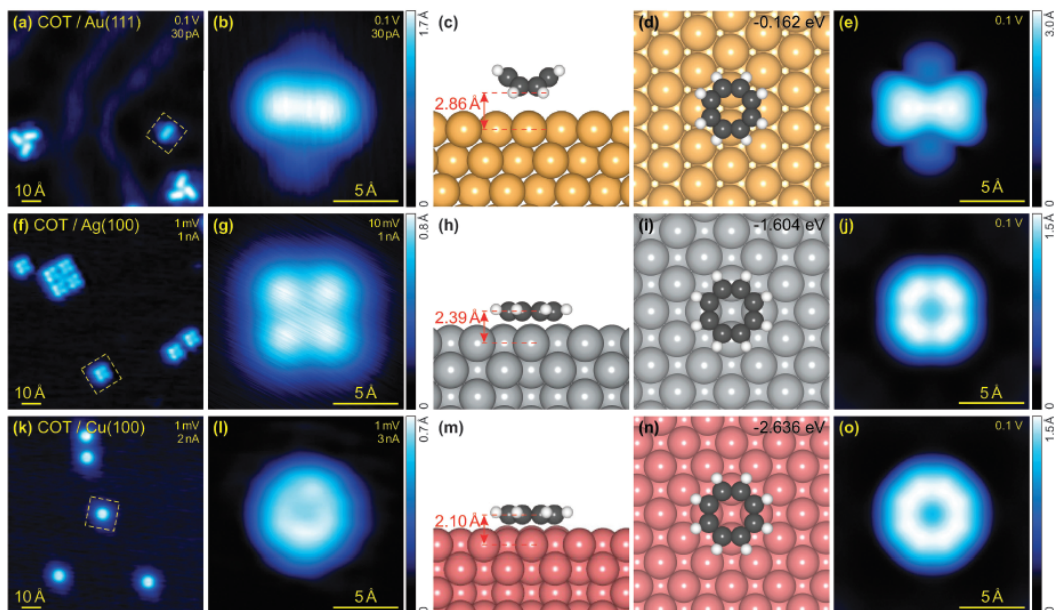


Figure 3.5: Molecule surface interaction: comparison between theory and experiment. a)-e) COT on Au(111) f)-j) COT on Ag(100), k)-o) COT on Cu(100). First column (a,f,k): overview STM image, second column (b,g,l): single molecule STM image, third column (c,h,m): side view of DFT geometry, fourth column (d,i,n): top view of DFT geometry, fifth column (e,j,o): simulated STM image by DFT. Taken from [58].

Au(111) exhibits still discrete molecular orbital-like states and is similar to the DOS of COT in gas phase [58]. All observations are characteristic for physisorption.

However, if COT is deposited on the more reactive Ag(100) (Fig. 3.5h-j) DFT simulations show a significantly different behaviour: the adsorption energy is considerably higher (1.604 eV) and the molecule surface separation is lower (2.39 Å). Furthermore the molecule is forced into a flat adsorption geometry. Due to the higher reactivity of Ag(100) compared to Au(111) in the previous case, the interaction between molecule and surface is much stronger and typical chemisorption is observed. DFT calculations for COT on the even more reactive Cu(100) reveal a similar situation, with the expected behaviour of an even higher adsorption energy (2.636 eV) and an even lower molecule surface separation (2.1 Å). In both cases the DOS of COT exhibits only very broadened states, which have no similarity to the original DOS. The effects observed in the cases of COT/Ag(100) and COT/Cu(100) can be considered the typical result of chemisorption. Theoretically COT could become an aromatic molecule by charge transfer, which would also lead to a flat geometry. However, the DFT calculations showed no significant charge transfer. Thus, the flat geometry of COT on Ag(100) and Cu(100) results only from the hybridization with the respective surfaces and showcases again the multitude of possible changes in molecular properties. All predictions made by the DFT calculations could be qualitatively confirmed with STM measurements (first and second columns of Fig. 3.5).

Similar studies have been performed with various molecules on the Cu(111) surface [59] and second monolayer (ML) Fe/W(110) [60]. The effects discussed in this chapter highlight the enormous variety and tuneability of molecules on surfaces.

3.2.2 Molecules on magnetic surfaces

By applying the principles described in the previous section to molecules on magnetic surfaces one can try to design "hybrid-molecular magnets": molecule-surface hybrids with magnetic features. In contrast to SMMs, magnetic thin films have significantly higher Curie temperatures. For example, the Curie temperature of one layer iron on W(110) is 230 K [61], three layers of iron on Cu(001) reach 420 K [62]. Therefore, devices using hybrid-molecular magnets appear to have significantly better chances to operate at temperatures above room temperature.

The last section discussed the hybridization of molecules with non-magnetic surfaces. Since the DOS of non-magnetic substrates is not spin polarized, the new hybrid-molecular states are also spin degenerated. In contrast, molecules adsorbed on a magnetic surface are subjected to a spin dependent hybridization as shown in in Fig. 3.6a. Thus, both the level broadening $\Gamma^{\uparrow,\downarrow}$ and the energy level shift $\Delta E^{\uparrow,\downarrow} = \epsilon_{\text{off}}^{\uparrow,\downarrow} - E_F$ are now spin dependent. The size of these effects depends on the coupling strength between molecule and surface. If several layers of molecules are deposited on a FM surface, the different layers experience

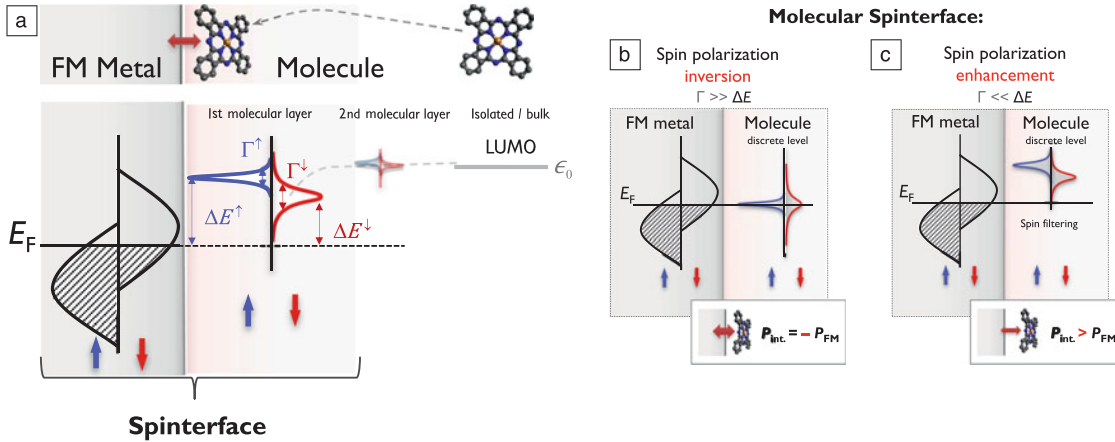


Figure 3.6: a) Spin dependent hybridization of a molecule with a ferromagnetic surface. The LUMO of the molecule is spin split, *i.e.* $\Gamma^{\uparrow} \neq \Gamma^{\downarrow}$ and $\Delta E^{\uparrow} \neq \Delta E^{\downarrow}$. The second layer of molecules is only weakly coupled to the FM surface. Thus the effects are smaller. The first layer of molecules and the topmost surface layer form a new electrode, named "spinterface", with a spin dependent DOS and considerably different properties than both isolated systems. b) For $\Gamma \gg \Delta E$ the spin polarization of the hybrid-molecular magnet is inverted when compared to the FM surface c) For $\Gamma \ll \Delta E$ the spin polarization of the hybrid-molecular magnet is enhanced when compared to the FM surface. Additionally a spin-filter functionality can arise. Taken from [51].

different couplings to the surface. Generally the first molecular layer exhibits the strongest coupling, while the coupling strength between second molecular layer and FM surface is already considerably lower. As a consequence, the spin dependent hybridization is weaker, *i.e.* the differences between the respective level broadenings and energy shifts are smaller. The properties of hybrid-molecular magnets are significantly different than the properties of both isolated systems.

The spin polarized DOS $D_{\text{int}}^{\uparrow(\downarrow)}$ of such hybrid-molecular magnets can be expressed by a Lorentzian distribution [51, 63]:

$$D_{\text{int}}^{\uparrow(\downarrow)}(E) = \frac{\Gamma^{\uparrow(\downarrow)}/2\pi}{(E - \epsilon_{\text{eff}}^{\uparrow(\downarrow)}) + (\Gamma^{\uparrow(\downarrow)}/2)^2} \quad (3.4)$$

Following this definition the effective spin polarization is determined by:

$$P_{\text{int}} = \frac{D_{\text{int}}^{\uparrow} - D_{\text{int}}^{\downarrow}}{D_{\text{int}}^{\uparrow} + D_{\text{int}}^{\downarrow}} \quad (3.5)$$

Now two cases are of special interest. For $\Gamma \gg \Delta E$, Eq. 3.4 leads to $D_{\text{int}}^{\uparrow(\downarrow)} \approx 1/\Gamma^{\uparrow(\downarrow)}$. This situation is depicted in Fig. 3.6b. The FM electrode exhibits a higher DOS for spin down than for spin up electrons at the Fermi level. The spin dependent hybridization leads thus to a strong broadening for spin down molecular states and a smaller broadening to spin up molecular states. As a consequence of this $D_{\text{int}}^{\uparrow(\downarrow)} \propto 1/D_{\text{FM}}^{\uparrow(\downarrow)}$. Using both expressions in Eq. 3.5 yields [51]:

$$P_{\text{int}} = -\frac{\Gamma^{\uparrow} - \Gamma^{\downarrow}}{\Gamma^{\uparrow} + \Gamma^{\downarrow}} \approx -\frac{D_{\text{FM}}^{\uparrow} - D_{\text{FM}}^{\downarrow}}{D_{\text{FM}}^{\uparrow} + D_{\text{FM}}^{\downarrow}} = -P_{\text{FM}} \quad (3.6)$$

Thus for $\Gamma \gg \Delta E$ the hybrid-molecular magnet exhibits an inversion of the spin polarization compared to the ferromagnetic substrate. This case is mainly expected for intermediate to strong surface-molecule couplings [51].

The opposite case of $\Gamma \ll \Delta E$, which is mostly presumed in weakly coupled molecule-surface hybrids, is depicted in Fig. 3.6c. Here, Eq. 3.4 leads to $D_{\text{int}}^{\uparrow(\downarrow)} \approx \Gamma^{\uparrow(\downarrow)}/(\Delta E^{\uparrow(\downarrow)})^2$. Since the broadening is small the new electrode's DOS is proportional to the original FM electrode's DOS: $D_{\text{int}}^{\uparrow(\downarrow)} \propto D_{\text{FM}}^{\uparrow(\downarrow)}/(\Delta E^{\uparrow(\downarrow)})^2$. Thus the spin polarization of the hybrid-molecular magnet can be expressed as [51]:

$$P_{\text{int}} \approx \frac{\frac{\Gamma^{\uparrow}}{\Delta E^{\uparrow 2}} - \frac{\Gamma^{\downarrow}}{\Delta E^{\downarrow 2}}}{\frac{\Gamma^{\uparrow}}{\Delta E^{\uparrow 2}} + \frac{\Gamma^{\downarrow}}{\Delta E^{\downarrow 2}}} > P_{\text{FM}} \quad (3.7)$$

Consequently this case leads to a higher spin polarization of the hybrid-molecular magnet compared to the ferromagnetic substrate. Furthermore, if ΔE^{\uparrow} and ΔE^{\downarrow} are considerably different a spin filter effect can arise, as will be shown in the next section.

3.2.3 Experimental confirmation

The theoretical considerations of the previous section were remarkably confirmed by Raman *et al.* [17] and Callsen *et al.* [48]. Callsen *et al.* [48] studied the adsorption of 2,2-paracyclophane (PCP) molecules on a monolayer Fe/W(110) with DFT. PCP is an organic, non-magnetic, biplanar π -conjugated molecule (Fig. 3.7a). DFT simulations revealed that the lower benzene ring of PCP couples strongly to the iron substrate. The four iron atoms binding with PCP have drastically changed magnetic properties (Fig. 3.7b). While the magnetic moment is reduced, the coupling strengths and anisotropy energies are increased. This leads to an increase in coercive field and Curie temperature (Fig. 3.7c,d). This effect was named "magnetic hardening" and demonstrates how the properties of magnetic thin films can be enhanced by the chemisorption of non-magnetic molecules.

While the increase in Curie temperature and coercive field are already impressive results, the PCP/Fe/W(110) system offers another important feature. The lower benzene ring of PCP is strongly hybridized with the Fe surface, whereas the upper benzene ring is only slightly affected by the interaction with the surface and retains its discrete molecular like states. As predicted in Fig. 3.6c, the weak coupling between the magnetic surface and the molecule causes spin-split molecular states. In the case of PCP/Fe/W(110) the LUMO is spin-split by 65 meV [48] which leads to a spin-filter functionality, similar to ferromagnetic insulators such as EuO [64].

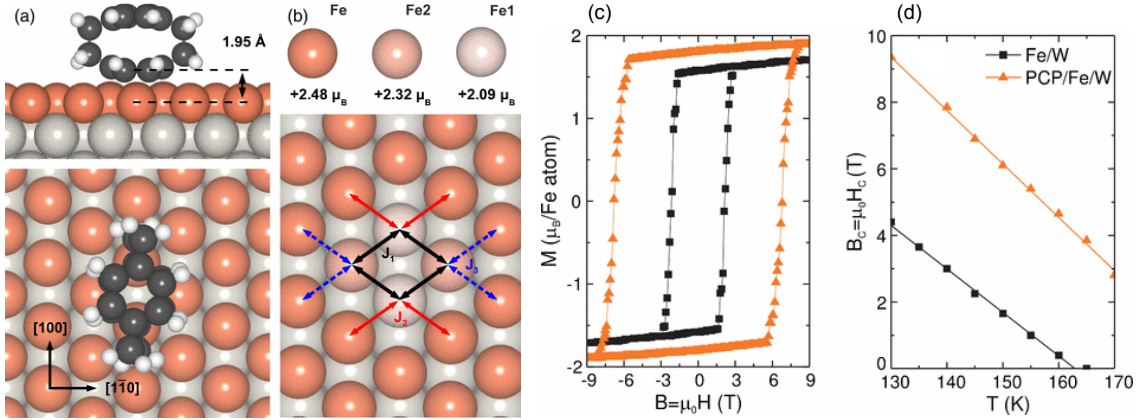


Figure 3.7: a) Adsorption position of PCP on Fe/W(110). Four iron atoms are directly involved in the bond to PCP. b) The Fe/W(110) surface without PCP. The magnetic moments, couplings strengths and anisotropy energies of the four affected iron atoms are changed when compared to unaffected Fe atoms. c) Hysteresis curve of Fe/W(110) (black) and PCP/Fe/W(110) (orange). d) Temperature dependency of the critical magnetic field. The hybrid system exhibits a higher Curie temperature and higher coercive field. Taken from [48].

All effects predicted theoretically in [48, 51] could be experimentally verified by Raman *et al.* [17]. They fabricated a device with a cobalt bottom electrode and copper top electrode separated by a 40 nm thick layer of non-magnetic, charge-neutral zinc-methyl-phenalenyl

(ZMP) molecules. A scheme of the device is shown in Fig. 3.8a. Although only one magnetic electrode was used, this device showed a magnetoresistance of 25 % at 4.2 K and 22 % at 250 K.

This behaviour is explained by the formation of hybrid-molecular magnets at the interface resulting from the hybridization of the surface layer of the cobalt electrode with the first layers of ZMP molecules. Accordingly the observed magnetoresistive effect was named interface magnetoresistance (IMR). The magnetization of the interface layer can be switched independently from that of the underlying substrate and does so at considerably higher magnetic fields.

The resistance of such a device, cooled down to 4.2 K in a magnetic field of 550 Oe, in dependence of the applied magnetic field is shown in Fig. 3.8c. Two switching processes are observed at ± 38 Oe, which can be unambiguously attributed to the switching of the cobalt electrode. However, the interface layer switching process is observed at 600 Oe. The formation of an interface layer which switches at a coercive field 15 times higher than the bulk electrode was a truly unexpected discovery. A scheme of the magnetization direction for both layers in dependence of the applied external magnetic field is shown in Fig. 3.8d.

The properties of the hybrid interface layer was also studied by DFT. The system used for DFT analysis is shown in Fig. 3.8b and consists of several layers of cobalt and two ZMP molecules forming a dimer. The lower molecule in contact with the cobalt surface, named "magnetic molecule" in Fig. 3.8b, forms a hybrid-molecular magnet. The p_z orbitals of the "magnetic molecule" hybridize strongly with the d -states of the substrate and form broad hybrid bands with bonding and antibonding character [16]. The spin-unbalanced DOS of this hybrid is shown as green graph in Fig. 3.8e. Furthermore the hybridization induces a transfer of a magnetic moment of $0.11 \mu_B$ from the surface to the molecule, which is coupled antiferromagnetically to the Co surface. At the same time the magnetic moment of the Co surface atoms is reduced to $1.7 \mu_B$ (bulk: $1.9 \mu_B$). More importantly, due to the hybridization with ZMP, the magnetic anisotropy energy (MAE) of the Co surface atoms is significantly increased ($K_{\text{sur}} \approx 180 \mu\text{eV}$, $K_{\text{bulk}} = 19 \mu\text{eV}$) while the coupling strength between the Co surface and Co bulk (J_{\perp}) is strongly reduced. These changes explain the formation of a magnetic interface layer which is only weakly coupled to the bulk and exhibits a higher coercive field.

However, the formation of an independently switchable interface layer does not explain the IMR alone. For an accurate description it is necessary to consider the second layer of ZMP molecules too. These molecules are physisorbed on top of the "magnetic molecule" (see Fig. 3.8b). Similar to [48] their electronic states retain their molecular character, but are spin-split and therefore act as spin-filter. The DOS of the "spin-filter molecule" is plotted in Fig. 3.8e with purple lines. The LUMO which is mainly responsible for transport is spin-split by 140 meV. This direction of spins preferred by the "spin-filter molecule" is always aligned antiparallel with the interface layer. Since the Co bottom electrode is independently switchable from the interface layer an antiparallel or parallel alignment of "spin-filter molecule" and Co electrode is possible. This determines the resistance of the junction². A scheme of the DOS responsible for the tunnel transport processes between the

²Cobalt has a negative spin polarization at the Fermi level. Therefore the majority spin species is

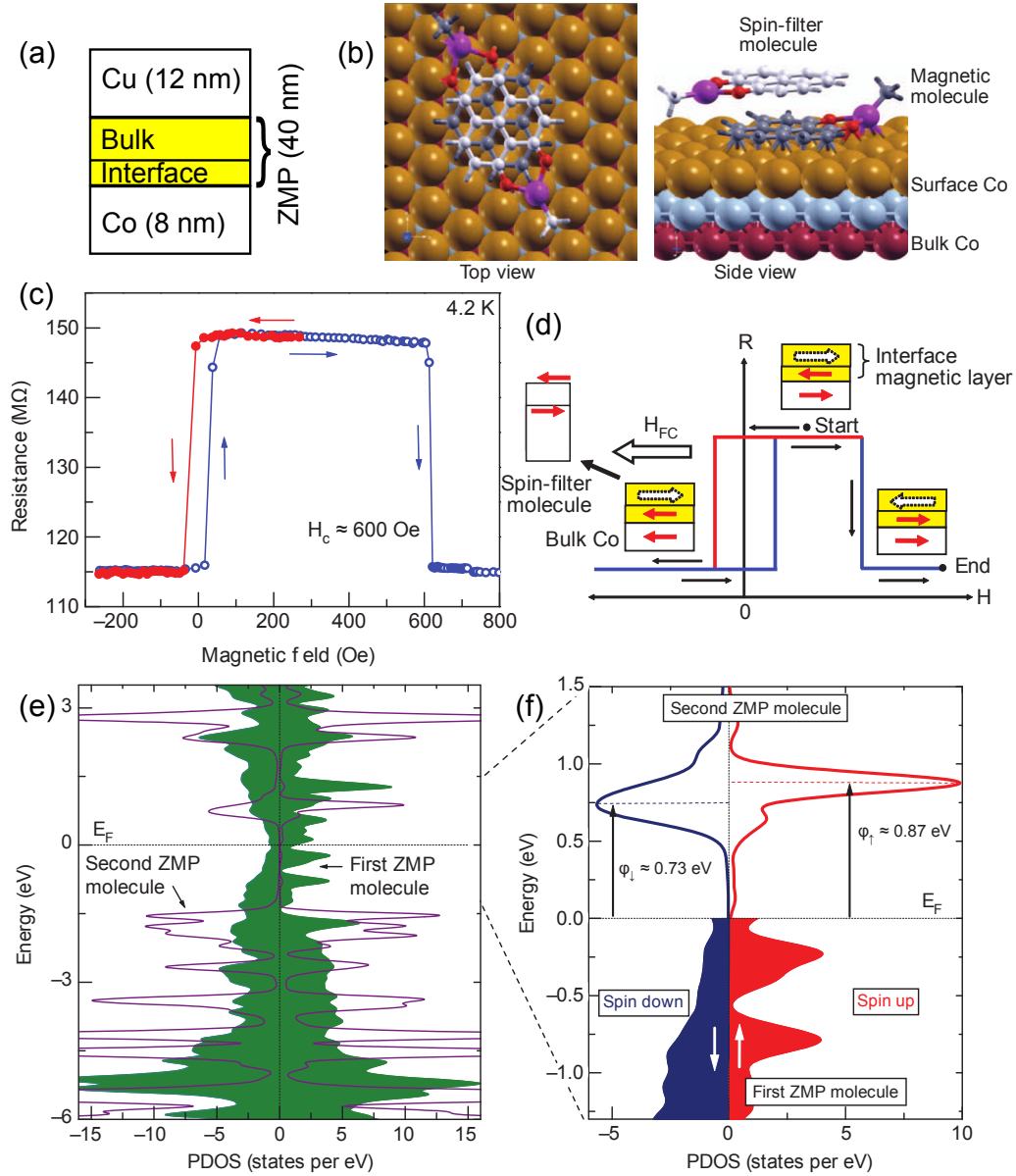


Figure 3.8: a) Scheme of the vertical-junction molecular device. b) Top view (left) and side view (right) of the ZMP "dimer" adsorbed on Co surface. c) Resistance vs magnetic field: showing the switching of the Co electrode at ± 38 Oe. The interface layer switches at considerably higher fields (600 Oe). d) Scheme of c) with respective magnetization directions. The inset on the left shows the different tunneling barriers for each spin species, due to physisorbed ZMP acting as spin-filter. e) PDOS of chemisorbed (green) and physisorbed ZMP (purple). f) Origin of the spin-filter functionality. Adapted from [17].

opposite as shown in Fig. 3.8d

”magnetic” and ”spin-filter molecule” is shown in Fig. 3.8f.

While all previously mentioned observations are in itself of high scientific value, the fact that the devices described in [17] operated also at 250 K made them even more valuable for applied research and additionally emphasized the true strength of this approach. By studying the interaction of molecules with magnetic surfaces we might be able to derive guidelines for further improving the properties of similar devices. Excellent tools for this task are STM and SP-STM which allow to investigate the electronic and magnetic properties respectively of such systems with high spatial resolution.

3.2.4 SP-STM experiments of molecules on surfaces

The first successful SP-STM experiment of molecules on a magnetic substrate was reported by Iacovita *et al.* [65]. They deposited cobalt phthalocyanine (CoPc) molecules on double layer Co islands on Cu(111). The Co islands are usually single-domain and have an out-of-plane magnetization. For molecules on islands with opposite domains they found a difference in conductivity above the Co atom of the CoPc. DFT calculations suggest a ferromagnetic coupling of the Co atom in CoPc to the Co island.

Similar experiments were conducted later in the Wiesendanger group with H_2Pc on the second ML Fe/W(110) [16] and CoPc on Co/Ir(111) [66] where, in contrast to Iacovita *et al.* [65], the spin polarization of the complete molecules was investigated. In [66] a spatial dependency of the spin polarization was observed: While the Co atom of the CoPc has a negative spin polarization, the peripheral benzene rings showed a positive spin polarization. Furthermore, for certain bias voltages a spin polarization was observed for the magnetic substrate, but not for the CoPc, confirming that the spin polarization is highly energy dependent.

The influence of the completely organic H_2Pc on the second ML Fe/W(110) was studied in [16]. The top image in Fig. 3.9 shows a SP-STM overview topography image where the characteristic alternating out-of-plane magnetic domains of the second ML Fe/W(110) are clearly visible. The influence of the magnetization direction of the Fe/W(110) substrate³ on the electronic properties of H_2Pc is significant:

As shown in Fig. 3.9a and b H_2Pc appears completely different on opposite domains. The spin polarization in Fig. 3.9c was obtained by expanding the procedure described in [35] to whole STM image, *i.e.* subtracting Fig. 3.9a from Fig. 3.9b. Fig. 3.9c reveals an inversion of the spin polarization on the hybrid-molecular magnet compared to the clean iron substrate as expected for strong a coupling between molecule and surface. The spin polarization for benzene on the second ML Fe/W(110) was calculated by DFT and agrees qualitatively with what was observed for the peripheral benzene rings in the H_2Pc .

The spin-splitting of molecular orbitals was observed for the first time for C_{60} on Cr(001) [67]. This study revealed hybrid states with a spin-splitting of roughly 450 meV and confirmed that both cases described by theory in section 3.2.2 can be found in SP-STM experiments.

³The electronic and magnetic properties of the double layer Fe/W(110) system are discussed in detail in chapter 6.

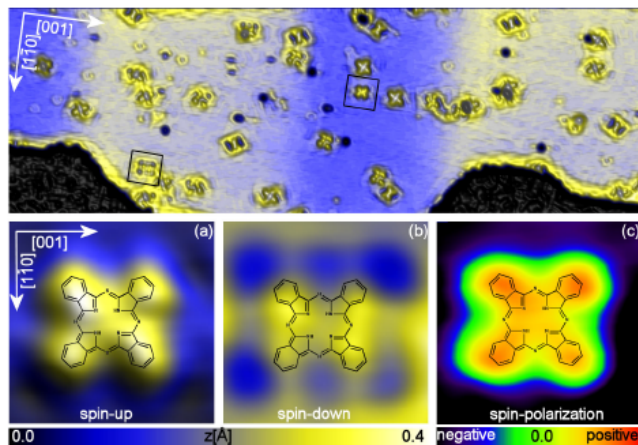


Figure 3.9: Top: SP-STM overview topography image ($V_{\text{Bias}} = 50 \text{ mV}$) of H_2Pc on the second ML Fe/W(110) showing several magnetic domains. (a) and (b) show H_2Pc in the same adsorption position on opposite magnetic domains. (c) is a difference image $[(a) - (b)]$ and shows qualitatively the spin polarization of H_2Pc on the second ML Fe/W(110). Taken from [16].

The previously discussed experimental studies show that the effects induced by molecules on magnetic surfaces include the inversion, attenuation or amplification of the spin polarization of the surface and highlight once again the versatility of molecules. The next step in the direction of device development is to investigate the switching behaviour of these hybrid-molecular magnets. One important step in this direction was done by Brede *et al.* [68]. They deposited coronene on Fe/Ir(111) and investigated the switching behavior of the resulting hybrid-molecular magnets with SP-STM by applying external magnetic fields. The average coercive field of coronene on Fe/Ir(111) was determined to be 1.25 T. Furthermore, instead of coronene, small graphene flakes with diameters of five to ten nanometer were deposited on Fe/Ir(111). The switching field for the graphene hybrid-molecular magnets almost always exceeded the experimental limit of 6.5 T. This confirmed experimentally that hybrid molecular magnets can be switched by external magnetic fields and that the necessary switching field depends on the size of the unit.

In the case of [68] the external magnetic field was applied to the whole sample, which leads to the switching of all hybrid-molecular magnets. For devices, however, one would like to be able to address single hybrid-molecular magnets. One possibility could be to apply the magnetic field only locally, similar to standard hard disc drives. However, in most experimental setups this approach is rather challenging. Another method, spin-transfer torque, uses spin polarized currents to modify the magnetic orientation of nanoscopic objects. This technique has been successfully demonstrated with SP-STM for Fe/W(110) nanoparticles [69] and artificially constructed nanomagnets consisting of five to seven Fe atoms on Cu(111) [70]. The switching of single hybrid-molecular magnets or SMMs without switching the underlying magnetic substrate has not yet been demonstrated.

3.3 Molecule deposition

Surfaces are very sensitive to contamination. Therefore the investigation of surfaces is typically conducted in an environment where contamination is strongly reduced: ultrahigh vacuum (UHV). UHV is the vacuum regime with pressures lower 10^{-9} mbar where samples can be investigated for at least several hours before notable contamination sets in. *In-situ* sample preparation including molecule deposition in UHV leads to very defined systems and is highly desirable in research. In certain cases, *ex-situ* sample preparation techniques can lead to comparable good results.

3.3.1 *In-situ* techniques

Common techniques for preparing thin film systems under UHV conditions for non-molecular materials, like metals or insulators, are electron beam evaporation or magnetron sputtering. Both methods are not suitable for molecule deposition, since the involved high energy electrons or ions will lead to the decomposition of molecules. However, a related method, sublimation, can be used. Molecules are usually available in powder form. This powder is heated in a crucible until the molecules eventually sublime. This technique can be used in UHV and is an excellent way for preparing clean and highly defined samples.

Unfortunately this method is only applicable to very few molecules. Many molecules decompose, by *e.g.* breaking intra-molecular bonds, before sublimating. Especially large and fragile molecules are prone to this behaviour. For such cases other in-situ techniques have been developed, like pulse injection [71, 72], electrospray [73] or dry imprint [74]. In pulse injection, molecules in a solution are injected into the UHV system. Ideally the solvent evaporates immediately and only the molecule is deposited on the sample, but usually co-deposition can not be avoided [72]. This technique requires extremely pure solvents to reduce sample contamination and high pumping power in the UHV system. The electrospray technique is an improvement of the pulse injection method. Similarly, molecules in solution are injected into the UHV system, but once in UHV they are ionized and decelerated by electric fields before hitting the sample. This method allows the deposition of more fragile molecules compared to pulse injection but requires considerably more experimental effort. The dry imprint technique uses a stamp to transfer molecules from it to the sample. While having been successfully demonstrated with TbPc₂ [74], this technique has not seen widespread use, since it is not possible to deposit an exact amount of molecules and the reusability is limited.

The stability of molecules on surfaces is potentially influenced by the adsorption, kinetic and thermal energy. However, both kinetic and thermal energy are in almost all cases considerably lower than the adsorption energy. The stability of molecules in dependence of the adsorption energy has been subject of extensive studies [8].

3.3.2 *Ex-situ* techniques

As previously mentioned many bulky or fragile molecules can not be sublimated in UHV. Unfortunately many SMMs belong to this category. Since they are already magnetic

themselves, *ex-situ* deposition on an inert non-magnetic metallic surface, *e.g.* gold or highly oriented pyrolytic graphite (HOPG), is a viable alternative. In this case the deposition is usually carried out from solution. Here, either a droplet of solution is deposited on the sample and the solvent is allowed to evaporate or the substrate is completely immersed in solution. To guarantee a grafting to the surface, it is necessary for these molecules to exhibit a special functionalization. These methods allow the fabrication of samples which are clean compared to UHV standards. Most impressively this has been demonstrated by the formation of self-assembled monolayers (SAM) of thiols on gold surfaces [75]. Here, the high chemical affinity of sulfur to gold is exploited. If thiols get close to a gold surface, the characteristic S-H bond is cleaved and the sulfur atom subsequently forms a strong covalent bond to a gold surface atom. Also other sulfur containing organic compounds, such as disulfides [76] or thioethers [77, 78], can be used for surface grafting.

In the case of SMMs *ex-situ* approaches have been proven to be partially effective. While successful attempts haven been reported especially in the beginning of such studies the influence of the surface-molecule interaction was largely underestimated. The interplay between ligand, functional unit and surface is very complex and can lead to molecular decomposition or to the loss of magnetic properties [15]. To make matters even more complicated also effects of the solvent on the deposition characteristics have been found [79]. Whether a certain combination of functional unit, ligand, surface and solvent leads to the desired properties depends on the particular case and can not be predicted.

3.4 {Ni₄} SMM

A new SMM with the formula $[\text{Ni}(\mu_3\text{-Cl})\text{Cl}(\text{HL}\cdot\text{S})]_4$ (abbreviated: {Ni₄}) with HL·S = C₁₁H₁₅NOS was synthesized in cooperation by our in-house chemists from the Kögerler group from RWTH Aachen and the Braunstein group from University of Strassbourg. Fig. 3.10 shows a persepective and top view of {Ni₄}. The HL·S ligand is shown on the right in Fig. 3.10. In the course of this PhD thesis the investigation of {Ni₄} was published in [80], on which this section is partially based upon.

The prospects of using such molecules for molecular spintronics have been motivated in the previous sections of this chapter. One of the major challenges which obstructs the widespread use of such molecules for spintronic devices is the controlled deposition and the understanding of the associated physisorption and chemisorption phenomena, which may be detrimental to the desired molecular properties.

This objective has led to the use of grafting groups to better control the molecule-surface interaction. With respect to stable and controlled anchoring, the formation of self-assembled monolayers (SAM) of sulfur-functionalized molecules on gold surfaces has proven a scalable method, in particular for molecules with thiol end-groups [81, 82, 83, 75]. However, it is a priori unknown if and how a specific grafting group and its binding to the substrate are going to affect the molecular properties after adsorption. For example, {Mn₁₂} molecules with thiol-based grafting groups deposited on gold lose the characteristic SMM features [15], whereas {Fe₄} SMMs on gold retain their magnetic properties owing to the decoupling of the magnetic core from the surface by suitable, bulky spacer groups [84, 85]. While thiols (-SH)

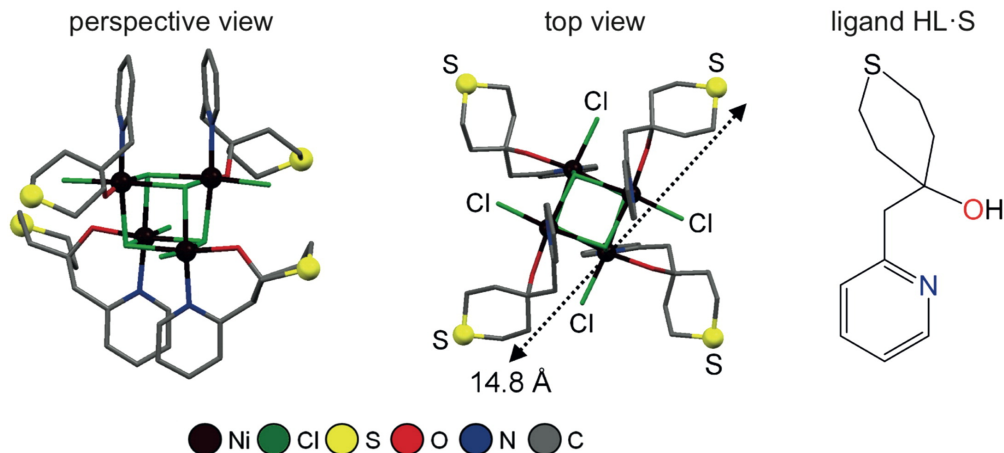


Figure 3.10: Perspective (left) and top (middle) views of the molecular structure of $[\text{Ni}(\mu_3\text{-Cl})\text{Cl}(\text{HL}\cdot\text{S})]_4$, where $\text{HL}\cdot\text{S}$ represents a pyridylalcohol-type ligand with an aliphatic cyclic thioether group (right). The nickel and sulfur atoms are represented as ball-and-stick models. Hydrogen atoms are omitted for clarity. Taken from [80].

[86], methylsulfides ($-\text{SMe}$) [87], and 1,2-dithiolanes ($-\text{S-S}-$) [88] have proven to be effective anchoring groups to gold electrodes in the chemistry and physics of magnetic coordination complexes [89], other thioether-like groups such as cyclic thioethers are still unexplored. The systematic investigation of the adsorption phenomena of metal organic molecules on various metallic surfaces and thus of the generated molecule-substrate hybrids is appealing and worthwhile because it should allow to derive necessary guidelines for the fine-tuning of the critical metal-ligand coordination bonds and the structure and composition of the molecular material.

$\{\text{Ni}_4\}$ was synthesized as an attempt to expand the strategy of using thiols as aurophilic deposition groups, for the first time, to aliphatic cyclic, *i.e.* semi-rigid, thioether functions. This strategy aims at taking advantage of the facts that thioether grafting groups are less prone to oxidation and are also suitable for the production of SAMs on coinage metal surfaces [76, 90, 78] by forming a weaker coordination-type bond.

The synthesis, structure, and magnetochemistry of the cubane-type nickel(II) complex $\{\text{Ni}_4\}$ containing four neutral pyridyl-alcohol-type ligands ($\text{HL}\cdot\text{S} = \text{C}_{11}\text{H}_{15}\text{NOS}$) with structurally exposed, peripheral thio-cyclohexane functionalities is reported in [1]. The four octahedrally coordinated nickel centers form a distorted $\{\text{Ni}^{\text{II}}(\mu_3\text{-Cl})_4\}$ cubane core, the remaining three coordination sites per nickel center are occupied by a terminal chloride ligand and the N and O donor sites of one chelating $\text{HL}\cdot\text{S}$ ligand. In contrast to the previously investigated cubane-type $[\text{Co}_4^{\text{II}}\text{Cl}_4(\text{HL})_4]$ SMMs (ratio $\text{Co}/\text{HL}/\text{Cl} = 1:1:1$) [91], the present system $\{\text{Ni}^{\text{II}}(\mu_3\text{-Cl})\text{Cl}\}_4 \leftarrow (\text{HLS})_4$ (ratio $\text{Ni}/\text{HLS}/\text{Cl} = 1:1:2$) does not involve charge transfer between the magnetic core metals and the HLS ligands. This allows us to address the effect of the ligands charge neutrality on the adsorption characteristics of our cubane-type tetranuclear Ni(II) complex.

As a polycrystalline material, $\{\text{Ni}_4\}$ is stable up to about 525 K under protective

atmosphere and soluble in dichloromethane (DCM). The stability in DCM solution was proven by fourier transform infrared (FT-IR) spectroscopy [1]. $\{\text{Ni}_4\}$ has a diameter of about 15 Å (S to S) and its magnetism is characterized by ferromagnetic coupling between the Ni ions ($J = +1.3\text{ meV}$) and a slow relaxation up to 3.8 K as determined by an ac susceptibility measurement at $f = 199.9\text{ Hz}$ [1].

3.5 Triphenyl-triazine

2,4,6-triphenyl-1,3,5-triazine (TPT) is a flat aromatic organic molecule composed of three phenyl rings which are attached to the carbon sites of a central 1,3,5-triazine ring. The 3-fold symmetric gas-phase geometry of TPT is shown in Fig. 3.11. TPT appears as an interesting choice for studying its interaction with surfaces since its two types of aromatic rings (*i.e.* phenyl and triazine) should lead to different hybridizations in one molecule.

In a previous study by Atodiresei *et al.* [59] the electronic properties of benzene (C_6H_6) and the benzene derivatives pyridine ($\text{C}_5\text{N}_1\text{H}_5$) and pyrazine ($\text{C}_4\text{N}_2\text{H}_4$) chemisorbed on Cu(110) were investigated by DFT. Although these molecules are only different by one or two atoms respectively (if the hydrogen is neglected), their adsorption positions and electronic properties differ significantly. One notable distinction is that the HOMO in benzene has π -character, while in pyridine and pyrazine the HOMO has σ -character which is reflected in the DOS of the molecule-surface hybrid.

In a similar theoretical study by Friedrich *et al.* [92] the electronic and magnetic properties of CH_2BH , C_2H_4 , CH_2NH and CH_2O chemisorbed on Fe/W(110) were investigated. While a magnetic hardening was observed for CH_2BH , C_2H_4 and CH_2NH , a softening was detected in the case of CH_2O . This study emphasizes the enormous tuneability of magnetic thin films affected by organic molecules.

Studying TPT deposited on magnetic thin films promises new insights about the properties of hybrid-molecular magnets. TPT is expected to exhibit delocalized electrons in p_z orbitals as is typical for flat aromatic molecules. Thus it appears as a good choice for studying the spin dependent hybridization. Depending on the coupling strength, effects ranging from inversion to enhancement are expected [51]. The existence of different aromatic rings in one molecule could lead to highly site dependent effects and offers new insights into designing the properties of organic-ferromagnetic interfaces.

Furthermore, when applying the ideas of Friedrich *et al.* and Brede *et al.* [68] to TPT deposited on a magnetic surface, one could conjecture the formation of several individual switchable units. Such systems could provide invaluable information on how to design switchable magnets on a sub-nanometer level at or close to room temperature. As demonstrated by Raman *et al.* [17] macroscopic devices based on these principles show impressive properties. The understanding of the involved fundamental principles can be improved by studying suitable microscopic systems and allows the derivation of new guidelines for optimised macroscopic devices.

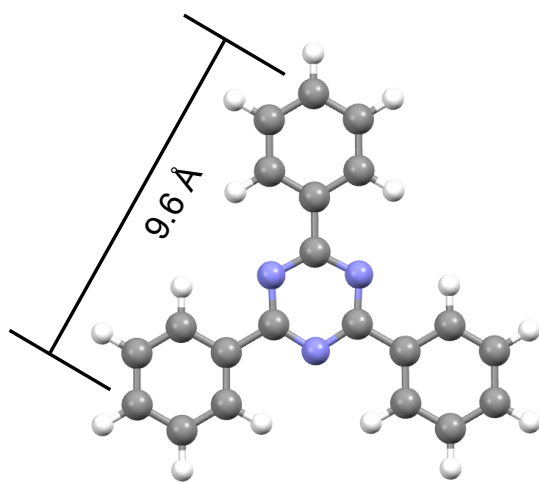


Figure 3.11: Geometry of TPT in gas-phase. Grey: Carbon, purple: Nitrogen, white: Hydrogen. TPT can be considered as an equilateral triangle with a side length of 9.6 Å (C to C).

Chapter 4

Experimental methods

The first section of this chapter introduces the Nano Spintronic Cluster Tool (NSCT) UHV system where the preparation of all samples and most of the measurements were conducted. The second section discusses the preparation of the two main sample systems investigated in this PhD thesis: $\{\text{Ni}_4\}/\text{Au}(111)$ and TPT/Fe/W(110). The third section is dedicated to a crucial point in STM experiments: The preparation of STM tips.

4.1 NSCT vacuum system

The NSCT allows the preparation and investigation of samples with various methods without the necessity of breaking the vacuum. A schematic drawing of the NSCT is shown in Fig. 4.1. In general the fabrication of spintronic devices is possible via two approaches: top-bottom (*e.g.* molecules on surfaces) or top-down (*e.g.* lithography). An extensive preparation chamber and the combination of two complementary analysis chambers, connected via a transfer chamber, allows to pursue both approaches in the NSCT.

Sample preparation is usually a two step process: A suitable substrate is prepared first and afterwards, an interesting material is deposited on it. For reproducible and comprehensible results, substrates should ideally exhibit homogeneous and highly defined surfaces. Both requests are met by single crystals and make them common choices as substrates. In almost all cases proper cleaning procedures are already established and guarantee reproducible substrate conditions. Depending on the particular single crystal, different techniques are required for cleaning. For this task the preparation chamber of the NSCT is equipped with a sputter gun (*e.g.* Au(111) in section 4.2.1) and a high temperature e-beam heater for flashing¹ (*e.g.* W(110) in section 4.3.1) and annealing.

For the deposition of materials, the preparation chamber is equipped with three different evaporators:

- A homebuilt Knudsen-cell type evaporator for organic material (*e.g.* TPT).

¹Flashing, when referring to tungsten substrates, denotes a process where samples are heated to temperatures of 2500 K and higher for a short amount of time, typically 10-30 s.

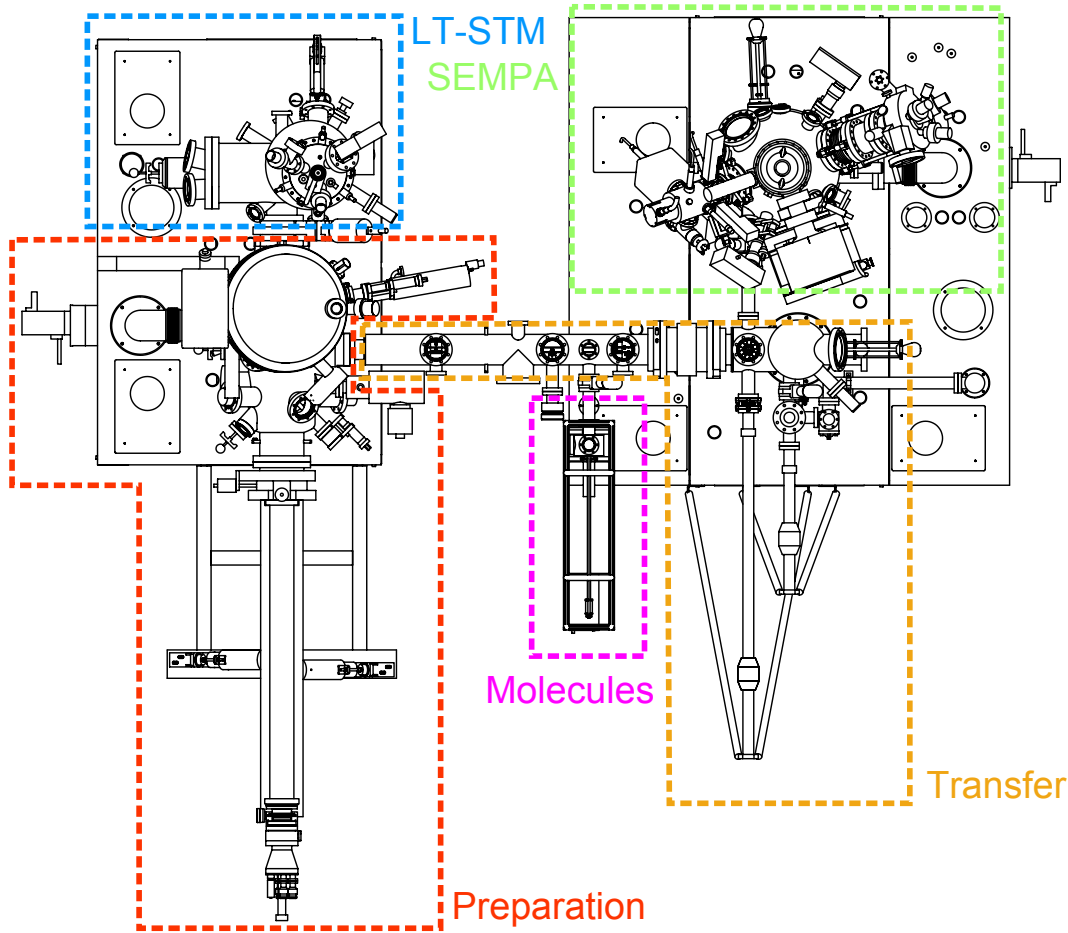


Figure 4.1: Scheme of the Nano Spintronic Cluster Tool. The individual UHV chambers are color coded: LT-STM in blue, preparation chamber in red, SEMPA in green, load lock and transfer in orange, molecule evaporation chamber in magenta. Courtesy of Frank Matthes.

- A triple e-beam evaporator from FOCUS. Due to its particular construction this evaporator achieves very low pressures during operation and is ideally suited for highly contamination sensitive samples. This evaporator was used for *e.g.* depositing iron thin films on W(110).
- A five-pocket e-beam evaporator from Thermionics. This evaporator achieves significantly higher deposition rates at the cost of slightly higher pressures during evaporation. It was used for *e.g.* coating STM tips with chromium.

During evaporation, samples can be either cooled down to 30 K with liquid helium or resistively heated to 500 K. To analyze film growth and sample cleanness the preparation chamber is additionally equipped with a low-energy electron diffraction (LEED) setup and an Auger electron (AES) and X-ray photoelectron spectroscopy (XPS) system. The base pressure of the preparation chamber reached under standard conditions $3 \cdot 10^{-11}$ mbar.

After preparation, samples can be transferred in one of the NSCTs analysis chambers. All STM measurements were conducted with the low-temperature STM from Omicron. The LT-STM can be cooled down to 5 K with liquid helium. The reduced drift and high thermal stability at this temperature make the LT-STM ideally suited for microscopy and spectroscopy studies of single molecules. As explained in chapter 2, STMs are powerful tools to investigate the topography and spectroscopy of samples on a nanometer scale and are thus very valuable when examining bottom-up approaches.

The second analysis chamber is equipped with a scanning electron microscope with polarization analysis (SEMPA) and a focussed ion beam (FIB). The FIB allows to fabricate well defined nanostructures and is central for top-down approaches in the NSCT. Unfortunately, SEM can hardly contribute any valuable information when investigating the interaction of single molecules with surfaces. However, the SEM was used as a supplementary tool to characterize the shape of STM tips in order to estimate their suitability for STM operation.

Preparation and SEMPA chamber are connected via the transfer chamber (other in Fig. 4.1). The transfer includes a load lock for the introduction of new samples into the system. A separate chamber is exclusively used for the evaporation of molecules (magenta in Fig. 4.1). This chamber is equipped with another homebuilt Knudsen-cell type evaporator and a micro balance for finding suitable evaporation parameters for molecules. Additionally, it can be baked separately and thus allows to exchange evaporation materials quickly.

4.2 $\{\text{Ni}_4\}/\text{Au}(111)$ sample preparation

A Au(111) single crystal served as a substrate for the $\{\text{Ni}_4\}$ experiments. Gold substrates are frequently used for the deposition of molecules due to two reasons:

1. The high inertness of gold allows *ex-situ* deposition of molecules, *e.g.* by drop-casting, with negligible contamination of the surface due to exposure to atmospheric conditions.
2. The chemical affinity of gold to sulfur allows an easy fabrication of self assembled monolayers with S-functionalized molecules.

Since $\{\text{Ni}_4\}$ exhibits S-functionalized ligands, an Au(111) single crystal was a natural choice. Both steps of the sample preparation, *i.e.* cleaning the Au(111) crystal (section 4.2.1) and depositing the $\{\text{Ni}_4\}$ on it (section 4.2.2) are discussed in the following.

4.2.1 Preparation of Au(111)

Gold crystals are cleaned by sputtering. During this process the sample surface is bombarded with high energy noble gas ions (typically argon). The impact of the high energy ions leads to the removal of surface atoms of the sputter target, *i.e.* both adsorbates and sample material and results in a clean, but rough surface². By heating the sample surface atoms can rearrange themselves and form a smooth surface again. Like many other metals, Au(111) has an intrinsic surface reconstruction: $23 \times \sqrt{3}$ or "herringbone reconstruction" [93]. In this

²Sputtering might be compared to sandblasting in the macroscopic world.

reconstruction the surface layer is contracted, thus forming regions of alternating hexagonal close-packed (hcp) and face-centered cubic (fcc) stacking.

The following procedure was found to lead to high quality Au(111) surfaces:

- Sputtering: 20 minutes with the following parameters: $p_{\text{Ar}} = 5 \cdot 10^{-6}$ mbar, 800 eV ion energy, sample current $\approx 5 \mu\text{A cm}^{-2}$.
- Annealing for 20 minutes at 900 K in UHV, afterwards cooldown to room temperature in 30 minutes.

Figure 5.5a of the next chapter shows an STM image of the reconstructed Au(111) surface obtained by this procedure. The elbows of the herringbone are the most reactive sites and are often occupied by adsorbates like CO molecules.

4.2.2 Deposition of $\{\text{Ni}_4\}$

$\{\text{Ni}_4\}$ is deposited from solution on a Au(111) single crystal. This method allows to utilize the S-functionalized ligands as described in section 3.4. Additionally, *in-situ* sublimation appears as an unlikely deposition route due to the low thermal stability of $\{\text{Ni}_4\}$.

$\{\text{Ni}_4\}$ thin films in the monolayer (ML) regime were deposited *ex-situ* by immersing the previously cleaned Au(111) crystal into an oxygen-free 0.5 mM $\{\text{Ni}_4\}$ -DCM solution for one hour. Afterwards the crystal was immersed into pure DCM for one hour to remove unbound species and contaminations. The deposition was conducted under argon atmosphere at room temperature [80].

The $\{\text{Ni}_4\}$ bulk sample for XPS reference measurements was prepared by drop casting about 20 μl oxygen-free 0.5 mM $\{\text{Ni}_4\}$ -DCM solution on a clean Au(111) crystal without applying subsequent rinsing in pure DCM. After preparation samples were directly transferred in UHV for post-annealing and investigation [80].

4.3 TPT/Fe/W(110) sample preparation

The preparation of TPT/Fe/W(110) samples follows a three step procedure. First, a clean W(110) surface needs to be established by cycles of flashing in UHV and annealing in oxygen atmosphere. Subsequently iron is deposited and transformed into the desired morphology. In a final step TPT is deposited by sublimation.

4.3.1 Preparation of W(110)

Tungsten substrates are a very common choice for depositing thin films, mainly due to strongly reduced intermixing of film and substrate and well documented cleaning procedures [94, 95, 96]. Elemental tungsten has an exceptional high melting point (3695 K). Thus, heating a W(110) crystal to very high temperatures should theoretically lead to the desorption of all adsorbates and result in a very clean surface.

Unfortunately, reality is not as simple. The main impurity of tungsten crystals is carbon, which occupies interstitial lattice sites. Heating the tungsten crystal to high temperatures

increases the mobility of carbon and leads to the segregation at the surface. As a result, tungsten carbide is formed which has a comparable melting point to elemental tungsten and thus cannot be removed by the aforementioned method.

The carbide is removed by annealing the tungsten crystal in an oxygen atmosphere. Oxygen reacts with the carbide and forms CO and CO₂, while oxydizing the remaining tungsten surface at the same time. Fortunately, tungsten oxides have a lower melting point and can be removed by heating to temperatures above 2500 K. In order to keep the segregation of carbon to a minimum, high temperatures are only applied for some ten seconds. This process is named "flashing". As a result, the tungsten cleaning procedure is a two-step process:

1. Annealing in oxygen atmosphere (to remove carbides)
2. Flashing in UHV (to remove oxides)

This procedure is repeated multiple times, until a sufficiently clean tungsten surface is achieved. The result of this procedure with varying parameters, *i.e.* duration, oxygen partial pressure and annealing temperature, has been investigated by STM [94, 95], LEED [95], EELS [96] and other techniques. The two-step process reported in [94] with the following parameters was employed during this PhD thesis:

1. Heated by electron bombardement (1500 V, 70 mA emission current) to 1800 K in an oxygen atmosphere for 30 minutes,
2. followed by flashing (1500 V, 340 mA emission current) to 2800 K for 30 seconds in UHV.

The first oxygen annealing cycle starts at $p_{\text{O}_2} = 5 \cdot 10^{-6}$ mbar. In the following cycles the oxygen partial pressure is halved until $p_{\text{O}_2} = 2 \cdot 10^{-8}$ mbar for the final step is reached. Once a sufficiently clean surface was established, the W(110) crystal could be flashed in UHV without the oxygen annealing procedure several times. As soon as a significant degradation of surface cleanness was observed, only the final step of the oxygen annealing procedure was repeated, resulting again in a very clean surface. The pressure during the high temperature flash is very important for the cleanness of the W(110) crystal. It was usually $2 \cdot 10^{-8}$ mbar during the flash, but decreased fast back into the low 10^{-10} mbar regime afterwards. The cleanness of the W(110) substrate was confirmed with STM and XPS.

4.3.2 Fe thin film deposition

Iron was sublimed from a rod of high purity (99.995 %) with a triple evaporator from Focus. The iron rod is heated directly by electron bombardement. Since iron is sublimable this method does not require a crucible. Additionally, the whole setup is enclosed with a water cooled heat shield in order to keep the degassing of non-evaporant materials to a minimum.

Iron was deposited on the previously cleaned W(110) substrate in the low 10^{-10} mbar regime at a rate of ≈ 0.6 ML per minute for usually 1.5 ML total coverage. For high quality

films both evaporator and evaporant need to be thoroughly degassed. The best results were achieved by leaving filament and evaporant always hot, but below evaporation conditions.

The growth mode of Fe/W(110) is discussed in section 6.1 in detail. A smooth morphology was induced by annealing. Films with large areas of first and second monolayer were achieved by annealing samples at 500 K for 8 minutes. Higher temperatures lead to the formation of islands with a thickness of four or more layers.

4.3.3 TPT deposition

TPT is a commercially available product which can be bought as a 99.5 % pure powder from Sigma-Aldrich. The powder was filled into a glass crucible and sublimated using a Knudsen-cell evaporator at 450 K at a rate of approximately 0.5 ML per minute. The pressure during sublimation was as low as $5 \cdot 10^{-11}$ mbar. Despite the low pureness of the TPT powder in comparison to other materials, samples showed a surprisingly low amount of contamination.

During TPT deposition it was necessary to cool down the Fe/W(110) substrate with liquid nitrogen to 170 K to reduce the mobility of adsorbed molecules. When deposited on a substrate at room temperature, TPT is mobile and sticks preferably to step edges and dislocation lines. A similar observation was made for TPT deposited on Co/Cu(111) [97].

It was found that already the transfer from the cold manipulator into the cold STM stage with a wobblestick at room temperature lead to a partial warm-up of the sample resulting in increased TPT mobility. To reduce the warm-up during transfers, the wobblestick was pre-cooled by touching the cold outer STM cryostat for at least 30 minutes prior to the transfer.

4.4 STM tip preparation

The properties of tips influence significantly the outcome of STM experiments. Therefore tip fabrication and preparation are crucial parts of every STM experiment and have been subject of extensive studies [98, 99]. During this work tips were etched *ex-situ* and subsequently processed with various *in-situ* treatments.

4.4.1 Tungsten tips

Etched tungsten are the most common choice for standard STM due to two reasons:

1. The etching can be done with rather low experimental effort.
2. The starting material, a polycrystalline wire, is easily available.

The etching setup used during this PhD is shown in Fig. 4.2. The tungsten wire (red) is immersed into the 5 M NaOH etching solution (light blue). Parts of the wire are protected by a Teflon coating (green and ocher), so the wire is only etched at the desired position

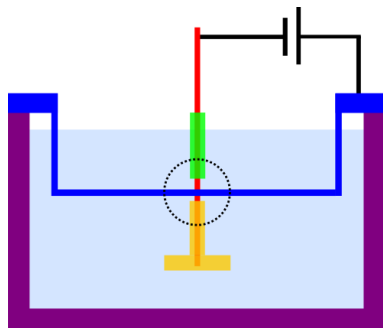
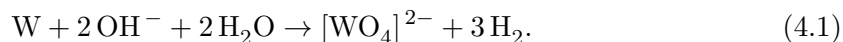


Figure 4.2: Schematic tip etching setup: A tungsten wire (red) is immersed into an etching solution (light blue). Parts of the wire are protected by a Teflon coating (green and ocher), so the wire is only etched at the desired position (marked by dotted circle). A current is applied between the cathode (dark blue) and the tungsten wire to start the etching reaction. The lower "T"-shaped Teflon coating (ocher) ensures a safe landing of the broken-off wire.

(marked by dotted circle). A current is applied between the cathode (dark blue) and the tungsten wire to start the etching reaction:



The wire is thinned by the etching reaction and the lower part eventually breaks off. In principle both the upper and the lower part can be used as STM tips. Using the lower part has the advantage that the etching process is terminated immediately after the wire breaks. If the etching process continues after breaking the aspect ratio of the tip will decrease again. The etching for the upper part continues until the is turned off. Electronic circuits have been developed in order to reduce the time between wire breaking and current shut off to a minimum [98]. By using the lower part as STM tip no additional electronic regulation is necessary. However, it must be guaranteed that the tip is not damaged by uncontrollably touching a surface. In the used setup the "T"-shaped Teflon coating (ocher in Fig. 4.2) of the lower part ensures a safe and upright landing. With this method tip radii down to 20 nm have been achieved [98]. After etching is finished, the tip is washed repeatedly in isopropanol and demineralized water and subsequently transferred into the UHV system for *in-situ* treatment.

While tips made by etching can be used without any further treatment, additional *in-situ* treatments offers various advantages. Typically tips are carefully heated to remove contaminations, residues from the etching process and oxides formed by the etching process and from the exposure to atmospheric conditions. At higher temperatures the tip apex eventually melts, which can induce a partial recrystallization. Such processes depend strongly on individual tip shapes and since the tip heating tool of the NSCT has no means of temperature control, it is difficult to predict the exact outcome.

However, tips and changes induced by heating can be imaged by SEM. The resolution in SEM in the NSCT is limited to approximately 10 nm and thus allows to get an impression of the general tip shape. The atomic structure of the tip apex which is responsible for tunneling can not be imaged. Other methods, like field emission microscopy have been proposed in literature for evaluating STM tips before actual STM experiments [99]. Since tips are prone to changes during experiment, the usefulness of these methods is questionable.

4.4.2 Tips for SP-STM

Tungsten is a non-magnetic material. Non-magnetic tips allow STM to probe the spin-integrated sample DOS. By using a magnetic tip, STM becomes sensitive to the spin-polarized sample DOS via the TMR as explained in chapter in 2.5. Therefore, the fabrication of magnetic tips has attracted considerable scientific interest and a multitude of techniques have been proposed. The most common ways to fabricate magnetic tips are:

1. use a magnetic material for the tip
2. coat the tip with magnetic material
3. pick-up magnetic material during experiment

Preparing STM tips from a magnetic material appears as an easy option and in fact tips from ferromagnetic materials, such as Ni [100] or Fe [101], have been successfully prepared and used for SP-STM. Unfortunately such ferromagnetic tips exhibit strong magnetic stray fields, making them unsuitable for the investigation of small or sensitive magnetic structures (*e.g.* magnetic thin films like Fe/W(110) [102]). In contrast, antiferromagnetic materials appear more favorable, because they exhibit negligible stray fields. Since transport in STM is dominated by a single atom, tips from an antiferromagnetic material can be sensitive to magnetic structures too. In fact, bulk Cr tips are a popular choice for SP-STM experiments [103, 104]. Similar to tungsten tips, bulk Cr tips are prepared by etching a polycrystalline wire. Since chromium wire is rather brittle it is not easy to process. Last but not least, bulk Cr tips are also not guaranteed to be spin sensitive. The reasons for this behaviour are not completely understood, but the formation of non-magnetic oxides or residues from the etching process seem plausible.

Therefore preparing a standard tungsten tip, cleaning it by flashing and subsequently covering it with a magnetic material can be viable alternative. Iron and chromium coated tips have proven to be very reliable tools for SP-STM [36, 37]. In order for the coating to stick properly to the tip, a very clean tip surface, ideally even recrystallized, is necessary. The magnetization direction is defined by the shape and interface anisotropy of the coating material. As a result, Fe-coated tips generally exhibit a strong in-plane (IP) magnetization [37]. While the stray field of tips coated with a ferromagnetic material is smaller than the field of bulk ferromagnetic tips, it has been shown to still affect samples [102]. Cr-coated (up to ≈ 45 ML [36]) tips generally have a strong out-of-plane (OOP) magnetization and negligible stray fields, making them ideal for many SP-STM applications [102].

Picking-up magnetic material with the STM tip during an experiment seems like an easy option, but is usually quite unreliable. The successful pick-up of magnetic material from a sample has been achieved by pulsing [105] or by dipping the tip into the sample [106]. With this method one has only small control over the magnetization direction and stability of the tip. Therefore, this approach is usually regarded only as a complementary method to the first two methods.

All methods were used during this PhD. Two bulk Cr tips using the same method described for tungsten tips in section 4.4.1 were prepared. Both tips did not show spin sensitivity, although successful attempts with this method have been previously achieved in

the NSCT [107]. Since the availability of Cr wire was very limited, coating easily available tungsten tips with magnetic material was a good alternative. Since iron evaporation was already established for the preparation of Fe/W(110), iron was used for the first coating experiments. Approximately 15 ML Fe were deposited at a rate of 1 ML per minute on a flashed tungsten tip. Out of two attempts, one tip exhibited strong IP sensitivity and one was non-magnetic.

The strong IP sensitivity of Fe-coated tips results in a low OOP sensitivity. Since one of the main scientific aims was to investigate the spin dependent hybridization of TPT on the OOP magnetized domains of DL Fe/W(110), Fe-coated tips proved to be not ideal. Therefore, as a next step flashed tungsten tips were coated with roughly 10 ML chromium at a rate of 0.3 ML per minute. Both attempts were successful, with the first tip (Fig. 4.3) being exceptionally good with high polarisation, high stability, strong OOP sensitivity and high spatial resolution. The second tip, although using the same preparation procedure, achieved spin contrast too, but was by far not as stable. The SP-STM results obtained on Fe/W(110) using Fe- and Cr-coated tips are shown in chapter 6. The SP-STM experiments on TPT/Fe/W(110) in chapter 7 were performed mostly with Cr-coated tips.

Picking-up material by pulses was observed once with an already iron coated tip, but could not be done in a reproducible way. Especially for the 1.5 ML Fe/W(110) system, dipping the tip into sample is not really a viable alternative since the magnetic film is only very thin.

Preparing and evaluating tips for SP-STM experiments is a time consuming process. In the NSCT tips are only exchangeable at 77 K or higher, whereas the experiments are ideally performed at 5 K. In case a tip does not show spin sensitivity, one can try to either get rid of oxides and contaminations by pulsing or to pick-up magnetic material. However, such attempts have been proven to be very unreliable and of low success rate. In contrast, the spin sensitive tips were spin sensitive directly at the beginning of the experiment and could be used for up to several weeks.

The first fabricated Cr-coated W-tip was investigated by SEM and is shown in Fig. 4.3. In Fig. 4.3a the tip is imaged with a magnification of 5000. The apex area appears very blunt with a radius more than 10 μm . The base of the tip seems to be full of etching residues. Fig. 4.3b shows the tip apex with a magnification of 10000. Areas with different brightness are visible, however it is not possible to distinguish the Cr-coating from the remaining material. Additionally it is difficult to determine the "front most" area where the tunneling actually happens. Although the overall impression from SEM of this tip suggests a bad STM suitability, this tip produced many high quality images. Experimentally it yielded a high effective spin polarization of up to 12.5 % (Eq. 2.23) and topography images with extremely high spatial resolution. This situation showcases even more the importance of the "last tip atom" in STM experiments.

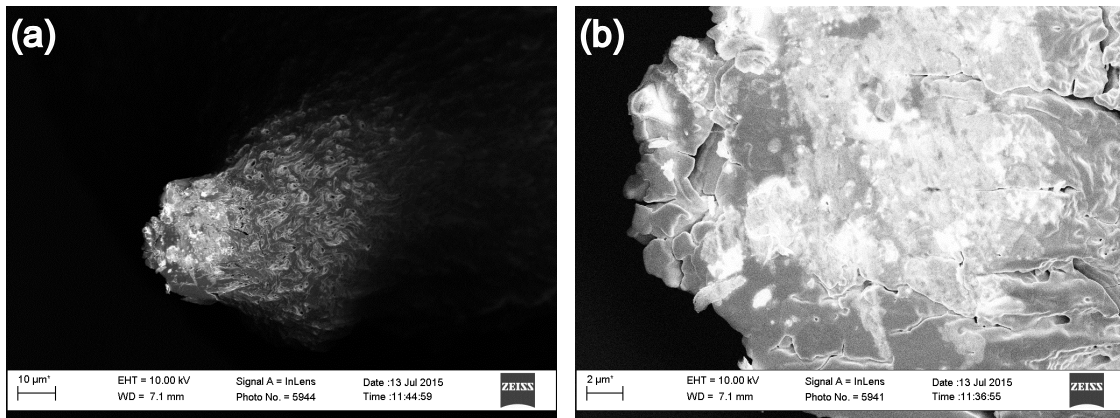


Figure 4.3: SEM images of a Cr-coated W-tip. (a) Tip apex with a magnification of 5000 (sample tilt 15°). (b) Tip apex with a magnification of 10000 (sample tilt 15°).

Chapter 5

{Ni₄} on Au(111)

The use of SMMs for spintronic devices has been motivated in the third chapter. Their actual use in devices is inhibited by two challenges:

1. low blocking temperatures
2. controlled deposition and understanding of adsorption phenomena

SMMs are small molecules where only a couple atoms are responsible for the magnetic properties. Thus, from today's perspective it seems unlikely that SMMs will eventually reach blocking temperatures close to room temperature. In certain cases where already the general realisation is most important, such as *e.g.* quantum computing, the need for very low temperatures does not really appear as limitation. Nevertheless, small incremental increases in blocking temperature might in the long term make a considerable difference regarding the widespread use of SMMs.

The second challenge, a controlled deposition and understanding the adsorption phenomena, is much more accessible. Novel surface functionalizations are easily synthesized and the obtained results can be used as input for new experiments. Such studies can potentially lead to new guide lines which might help to confine the vast amount of possible combinations to the most promising ones.

Due to the aforementioned challenges chemists constantly try to synthesize new compounds with new or improved properties. The {Ni₄} SMM is the result of such an attempt. In the {Ni₄} compound a novel Ni₄Cl₈ cubane-type core is responsible for the magnetic properties. In bulk ac susceptibility measurements at 199 Hz {Ni₄} showed a slow magnetization relaxation at 3.8 K [1]. In order to bind reliably to a surface {Ni₄} exhibits cyclic thioether functionalized ligands. Thioether-functionalized ligands have been successfully used for depositing molecules on gold surfaces [108, 90], but have not been used for grafting SMMs onto surfaces.

Thus, the deposition of {Ni₄} on Au(111) promises new insights into the surface binding capabilities and adsorption properties of thioether functionalized compounds, especially for SMMs. A combination of X-ray photoelectron spectroscopy (XPS) and STM was used to provide an in-depth analysis of the adsorption characteristics of {Ni₄} on Au(111). XPS and STM complement each other very nicely: XPS probes the binding

energy of photoemitted core electrons and thus is element sensitive to the element’s chemical environment. STM probes the DOS of a sample surface near the Fermi level and usually can not distinguish between different elements. However, it allows to investigate the real-space surface topography with sub-nanometer resolution and gives insight into binding geometries. Studying the adsorption properties is a prerequisite of investigating the magnetic properties of SMMs deposited on surfaces and potentially allows to derive new guidelines for the preparation of spintronic devices. The results of this study were published in [80]. This chapter is largely based on this publication including the supplemental material.

5.1 XPS results

XPS is a highly surface sensitive method for analyzing the elemental composition and chemical states of sample surfaces. Studying the peak fine structure of the S $2p$ signal gives insight on to binding mechanisms of the thioether functionalized ligand to the Au(111) surface. The investigation of the Ni $2p$ doublet revealed information of the state of the magnetic core.

5.1.1 As-deposited state

Since the binding of the $\{\text{Ni}_4\}$ to the surface is expected to be solely accomplished via the S-containing ligands, the surface binding capabilities of the bare HL-S ligand without the central $\{\text{Ni}_4(\mu_3\text{-Cl})_4\text{Cl}_4\}$ cube were first investigated as a reference. The results are shown in Fig. 5.1a and reveal that the S $2p$ signal consists of four components resulting from the superposition of three doublets with the $2p_{3/2}$ peak located at 161.1, 162.1, and 163.1 eV, respectively. The relative weights of the doublets are listed in Table 1 and agree well with previous literature reports on thioether-functionalized molecules [109]. The doublet at 163.1 eV, which is responsible for 52.9 % of the total signal, is attributed to a weak coordination-type bond [109], which is the expected binding for a thioether group. The doublets at 162.1 and 161.1 eV have basically the same intensity and are responsible for the remaining 47.1 % of the signal. The doublet at 162.1 eV is usually attributed [109, 110] to a thiol group bound to gold. The 161.1 eV peak is either due to atomic sulfur or due to a thiol group with different binding chemistry [109, 111], *e.g.* different binding site on the reconstructed Au(111) surface. For thioethers, both destructive [112] and non-destructive [113] adsorption on gold have been reported. Nevertheless, the appearance of ca. 50 % in this case thiols is surprising and inscrutable, but in agreement with Ref. [109]. The XPS reference measurement of a bulk $\{\text{Ni}_4\}$ sample (Fig. 5.1e) reveals a strongly broadened S $2p$ peak with maximum intensity at 163.9 eV that can be considered as a fingerprint of the HL-S ligands when not bound to the Au substrate. The absence of this component in Fig. 5.1a allows the conclusion that all unbound species are removed from the ligand reference sample by the deposition procedure, as expected.

As next step $\{\text{Ni}_4\}$ was deposited on Au(111) and the presence of all elements (except H) on the surface that constitute $\{\text{Ni}_4\}$ was confirmed by an XPS overview spectrum (Fig. 5.2) using a lab-based Mg $K\alpha$ radiation source. The Au peaks dominate the spectrum and the signal-to-noise ratios for the $\{\text{Ni}_4\}$ species are low as expected for a coverage in

the monolayer regime. Nevertheless, the elements' relative peak areas are in agreement with the expected values. The spectral weights for O, Cl, and C are slightly higher than expected, which most likely results from the solvent and the exposure to atmosphere. All these conclusions derived from XPS results could be qualitatively confirmed by Auger electron spectroscopy (AES).

The S $2p$ spectrum of $\{\text{Ni}_4\}$ (Fig. 5.1b) is quite similar to that of the adsorbed bare ligands (Fig. 5.1a). The S $2p$ signal consists of the same three doublets with slightly different weights (Table 5.1). For the intact $\{\text{Ni}_4\}$ it is geometrically impossible that all four ligands are bound to the gold substrate at the same time. Assuming that all ligands remain attached to $\{\text{Ni}_4\}$ one would expect that only one or two ligands per complex bind to Au, resulting in the XPS spectra in a component of the unbound species (Fig. 5.1e) with a weight of 50-75 %. The fact that such a component is not observed at all indicates that $\{\text{Ni}_4\}$ loses at least some of its ligands during deposition. The question whether all ligands are detached cannot be answered by XPS, but will be addressed later by STM. In both cases of bare ligand and complete $\{\text{Ni}_4\}$ deposition, a broadened C $1s$ peak was detected at 284.5 eV, which is a typical value for C in organic ligands [109].

S $2p_{3/2}$ peak energy (eV)	163.1	162.1	161.6	161.1
Species	Thioether	Thiol 1	Atomic S	Thiol 2
HL-S ligand	52.9	23.9	0	23.4
$\{\text{Ni}_4\}$	41	31.8	0	27.2
$\{\text{Ni}_4\}$ @ 400 K	16	44.7	0	39.3
$\{\text{Ni}_4\}$ @ 500 K	0	0	100	0

Table 5.1: Relative intensities of the S $2p$ doublets in the XPS spectra in percent. Doublets are named by the energy position of the $2p_{3/2}$ peak.

5.1.2 Post-annealed states

To gain more insight into the thermal stability and surface binding conditions, samples were post-annealed under UHV conditions. After 30 min at 400 K, a change of the S $2p$ weights was detected (Fig. 5.1c and Table 5.1). The amount of intact thioethers was reduced, while the contributions from the thiols were increased. By increasing the thermal energy, more ligands seem to transform into an energetic more favorable thiol form. After 30 minutes post-annealing at 500 K, only one doublet at 161.6 eV (Fig. 5.1d and Table 5.1) was observed, and heating to higher temperatures did not change the S spectrum anymore. The evolution of all three former doublets into a new one indicates significant changes of the S-containing ligand, most likely decomposition by releasing atomic S that binds to the gold surface.

Additional evidence for a ligand decooordination upon interaction with the surface stems from the electrochemical analysis of a gold electrode that is functionalized by the same treatment applied to the Au crystal for the *in-situ* measurements: It shows the same correlated oxidation and reduction waves as those appearing after a first nonreversible

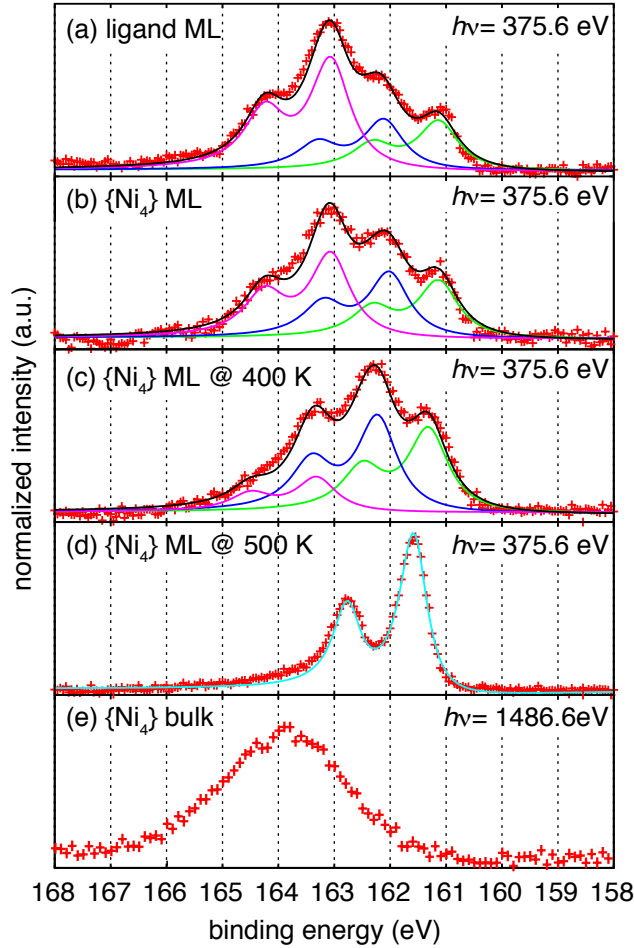


Figure 5.1: Normalized XPS S 2p spectra after deposition of (a) bare HL-S ligands on Au(111), (b-d) $\{\text{Ni}_4\}$ complexes on Au(111), and (e) the $\{\text{Ni}_4\}$ bulk reference sample. Post-annealing temperatures for (c) and (d) are indicated. Red crosses represent experimental data and solid lines in (a-d) the decomposition of the spectra into individual doublets at 161.1 eV (green), 161.6 eV (cyan), 162.1 eV (blue), and 163.1 eV (pink) according to Table 5.1. Black lines are the fitted total spectra. The background was subtracted with a Shirley algorithm. All S 2p doublets were fitted with a fixed $2p_{3/2} : 2p_{1/2}$ intensity ratio of 2 and a fixed energy splitting of 1.19 eV by Doniach-Sunjic functions with an asymmetry of 0.1 and a peak width of 0.32 eV. Experiments are carried out for (a-d) at BL 5 at DELTA with a photon energy of 375.6 eV and for (e) with a standalone spectrometer using monochromatized Al $K\alpha$ radiation.

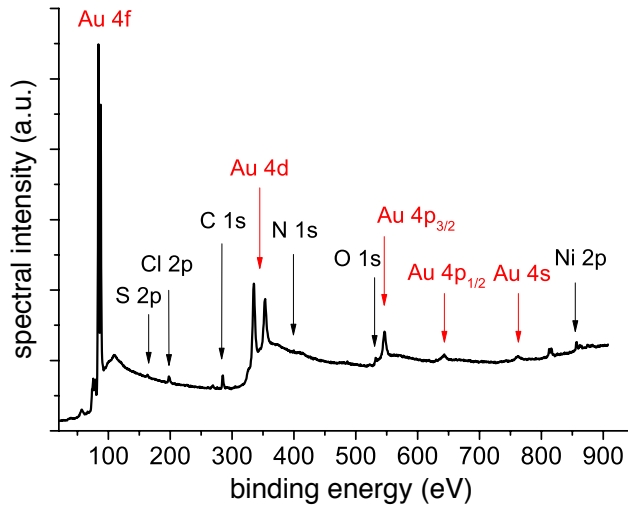


Figure 5.2: XPS overview spectrum after $\{\text{Ni}_4\}$ deposition on Au(111). The overview spectrum is dominated by the Au peaks (red), but all constitutive elements of the $\{\text{Ni}_4\}$ complex can also be detected and quantified. Obtained with a lab-based Mg $K\alpha$ radiation source.

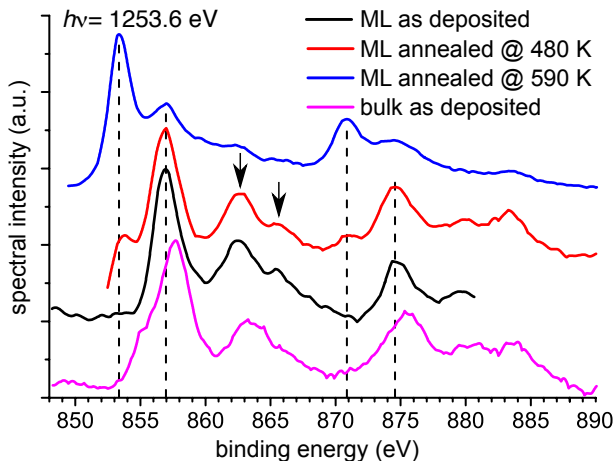


Figure 5.3: Shift of the Ni 2p doublet upon post-annealing. Before annealing (black) the Ni $2p_{3/2}$ peak is at 857 eV in good agreement with Ni(II) in a Cl environment. After subsequent annealing steps at 590 K, the Ni $2p_{3/2}$ peak shifts to 853.5 eV (blue) indicating the decomposition of the central cubane-like $\{\text{Ni}_4\text{Cl}_{4n}\}$ core. The pink spectrum of a $\{\text{Ni}_4\}$ bulk sample is slightly shifted with respect to the as deposited monolayer sample, but shows a very similar overall spectral shape. Black arrows mark the shake-up satellites.

oxidation in $\{\text{Ni}_4\}$ using a glassy carbon electrode (Fig. A.1 in the appendix). This indicates that the species deposited on gold is distinct from the intact $\{\text{Ni}_4\}$ complex and that the ligand decoordination process observed upon absorption is most likely initiated by electron transfer from the molecule to the metallic substrate.

Another interesting question concerns the state of the remaining $\{\text{Ni}_4\text{Cl}_{4n}\}$ ($n = 1$ or 2) core. For $n = 2$ the $\{\text{Ni}_4\text{Cl}_4\}$ core is decorated by four terminal Cl atoms (compare with Fig. 3.10), and $n = 1$ corresponds to the naked core. In a $\{\text{Ni}_4\}$ bulk reference sample, the Ni $2p_{3/2}$ peak is detected at 857.7 eV (pink line in Fig. 5.3). The presence of O and N donors in $\{\text{Ni}_4\}$ possibly explains the shift in binding energy of 0.7 eV with respect to NiCl_2 [114]. In addition, the two typical shake-up satellites (black arrows in Fig. 5.3) for a NiCl_2 film [115] are observed, in which the Ni is also octahedrally coordinated. The Ni $2p$ XPS spectrum of a $\{\text{Ni}_4\}$ monolayer sample in the as-deposited state (black line in Fig. 5.3) shows a very similar overall spectral shape, including the shake-up satellites, to the bulk sample, but the spectrum is shifted by 0.7 eV to lower binding energy. The similarity indicates that the cubane-like $\{\text{Ni}_4\text{Cl}_{4n}\}$ core is still intact after deposition although the ligands are decoordinated, which most likely gives rise to the slight shift in binding energy. In this context, it is also worthwhile to note that the detachment of the neutral ligands does not alter the charge on the remaining fragment, making it likely to be the cubane-like $\{\text{Ni}_4\text{Cl}_{4n}\}$ core of the parent molecule. The appearance of the shake-up satellites in the black and red spectra in Fig. 5.3 suggests paramagnetic behavior [115] of the core at room temperature, *i.e.* the measurement temperature. The Cl $2p_{3/2}$ peak is detected at 199 eV (Fig. 5.2), which is in good agreement with the expected Ni environment [114] and again confirms the integrity of the cubane-like $\{\text{Ni}_4\text{Cl}_{4n}\}$ core after deposition. However, from the XPS data one cannot state whether the terminal Cl atoms are still attached. If they were decoordinated but bound to the surface, they would still contribute to the spectra.

Upon post-annealing to 590 K, a significant shift of the Ni $2p_{3/2}$ peak by 3.5 eV (blue spectrum in Fig. 5.3) is observed. The significant reduction of Cl in the XPS spectra at this temperature (Fig. 5.4) provides strong evidence for the breaking of the central cubane-like

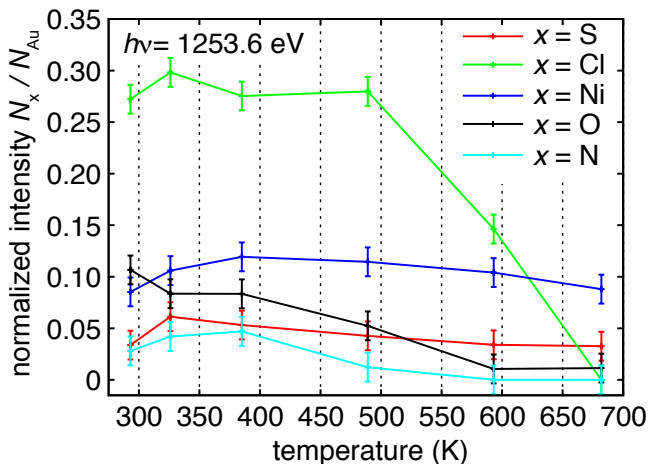


Figure 5.4: Elemental composition as a function of the post-annealing temperature reached in subsequent annealing steps. At higher annealing temperatures, the signals for O, N, and Cl completely vanish due to the decomposition of the $\{\text{Ni}_4\}$ complex. The S and Ni signals, however, are within the error bar constant during the whole annealing procedure.

$\{\text{Ni}_4\text{Cl}_{4n}\}$ core during annealing. After annealing, the Ni 2p binding energy is closer to that of bulk Ni^0 , implying at least a change in chemical environment but more likely a change in oxidation state from initially +II to 0.

Up to now, no studies concerning the magnetic properties of the intact cubane-like $\{\text{Ni}_4\text{Cl}_{4n}\}$ core remaining on the surface after the detachment of the charge-neutral HL·S organic ligands have been performed. However, the investigation of the magnetic properties of the cubane-like $\{\text{Ni}_4\text{Cl}_{4n}\}$ core on the surface by X-ray magnetic circular dichroism (XMCD) is in preparation.

5.1.3 Decomposition upon in-situ post-annealing

All changes of the elemental composition induced by stepwise post-annealing were monitored by lab-based XPS (Fig. 5.4). For low temperatures no significant change in the elemental composition were observed. Starting at 480 K, the O and N signal intensities strongly decrease indicating that the thermal stability of $\{\text{Ni}_4\}$ is reduced when deposited on a surface as compared to the stability in bulk (525 K) evidenced by thermogravimetric analysis (TGA) [1]. At 590 K the intensity of Cl drops significantly, and at 680 K neither O, N, nor Cl can be detected anymore, which clearly establishes the decomposition of the molecule in agreement with all previous statements. The amount of S is constant within the error bars of the XPS analysis, indicating that all S atoms are indeed bound to the Au substrate. This observation further supports the conjecture of ligand detachment during adsorption.

When discussing mechanisms for the observed molecular decomposition it is useful to consider relevant energy scales. The thermal energy involved in the post-annealing process ($kT \approx 25\text{--}70\text{ meV}$) is small in comparison to the adsorption energies of S on Au, which have been calculated using DFT to be as high as 4 eV for single S atoms, depending on adsorption geometry [116]. For thiols, DFT calculations lead to adsorption energies of 1-2 eV, depending on adsorption geometry [116]. For the related thiophene molecule, adsorption energies on Cu(100) of 630 meV have been reported [117]. Thus, it seems safe to assume that the adsorption energy of the thioether-functionalized $\{\text{Ni}_4\}$ is at least one order of magnitude

larger than the thermal energies involved in the post-annealing process. Therefore, it is very likely that the adsorption energy is the driving force behind the decomposition of the $\{\text{Ni}_4\}$ complex. However, higher adsorption energies do not necessarily cause more frequent molecular decomposition, but may result in increased molecular stability after adsorption, as recently reported [118]. Since there are only a few reports on the deposition of bulky thioether-functionalized molecules on gold [119], it is difficult to answer this question at the current stage. Nevertheless, the data suggest a separation of the ligands from the core directly when the cubane cluster is deposited on the surface. The post-annealing treatment then leads first to the decomposition of the ligands and, at higher temperatures, to the disintegration of the central cubane-like $\{\text{Ni}_4\text{Cl}_{4n}\}$ core.

5.2 STM results

In addition to XPS all sample states were investigated with STM. The main focus of the STM study was to potentially image intact $\{\text{Ni}_4\}$ complexes or fragments, such as the ligand or the $\{\text{Ni}_4\text{Cl}_{4n}\}$ core and their arrangement on the surface.

5.2.1 As-deposited state

Fig. 5.5a shows a typical STM image of the herringbone reconstruction of the clean Au(111) surface, and Fig. 5.5b the surface morphology after the $\{\text{Ni}_4\}$ deposition process, where no herringbone reconstruction is visible anymore. Instead the terraces appear to be covered by a diffuse blanket and irregularly shaped particles. In literature the formation of highly ordered SAMs with thioether-functionalized molecules has been reported [108, 90], but in the $\{\text{Ni}_4\}$ case no signs of any ordered structures or monoatomic depressions typically for highly ordered SAMs [120] could be observed. Larger molecules, such as most SMMs with multiple potential adsorption positions, usually show disordered adsorption patterns [85, 84]. These molecules can then be identified by statistically analyzing the particle size. Although irregularly shaped particles are observed, they show a random lateral size distribution and are typically much larger than a single $\{\text{Ni}_4\}$ cubane or its fragments. Zooming in these particles did not reveal any additional details. Thus, it seems very unlikely that these represent single $\{\text{Ni}_4\}$ or well-defined clusters of $\{\text{Ni}_4\}$.

Also LEED of the as-deposited state only shows weak Au(111)-(1×1) spots indicating no additional order. Therefore, it appears likely that the fragments resulting from the decomposition of $\{\text{Ni}_4\}$ are lying in a disordered fashion on the surface and give rise to the diffuse STM morphology.

5.2.2 Post-annealing at 590 K

Fig. 5.6a shows a STM picture after annealing at 590 K for 1 h, resulting in a completely different morphology with ordered, disordered, and also uncovered areas. In a few spots, some larger features are observed, which might be identical to those in the images taken prior to the post-annealing (Fig. 5.5b). The uncovered areas reveal a distorted herringbone reconstruction of the bare Au(111) surface (inset of Fig. 5.6a). Changes in the electronic

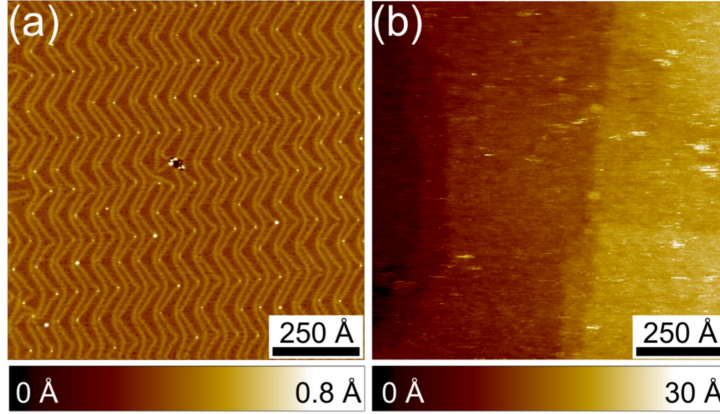


Figure 5.5: Surface morphology before and after $\{\text{Ni}_4\}$ deposition. (a) STM image of the cleaned Au(111) substrate showing up to 1000 Å wide terraces with a regular herringbone reconstruction. Image parameters: 1000 Å \times 1000 Å, $V_{\text{Bias}} = -1$ V, $I_{\text{T}} = 1$ nA, 78 K. (b) STM image after $\{\text{Ni}_4\}$ deposition on the surface shown in (a) without post-annealing. Image parameters: 1000 Å \times 1000 Å, $V_{\text{Bias}} = -1$ V, $I_{\text{T}} = 50$ pA, 5 K

structure due to the adsorption of particles can lead to a distortion of the herringbone reconstruction [121, 122] and very likely explain the particular case observed here. Most importantly, the observation of the herringbone reconstruction allows one to determine the particle coverage to be in the submonolayer regime and to measure the apparent height of the adsorbate layers.

The histogram of the height distribution calculated for the terrace in the right half of Fig. 5.6a, where no substrate step edges occur, is shown in Fig. 5.6b. The first peak in the histogram (black) represents the bare substrate, which takes 15 % of the surface area. The average height of the substrate is set to 0 Å. The second peak (red) is attributed to the disordered areas in Fig. 5.6a. The disordered nature is also confirmed by the larger width and the asymmetric shape of this peak, indicating that there is no strongly preferred height. About 65 % of the surface is covered with disordered areas, and the most probable height is 1.5 Å above the Au surface. The remaining 20 % of the surface exhibit ordered areas with an average relative height above the substrate of 2.2 Å. These height differences are much smaller than what is expected for intact $\{\text{Ni}_4\}$ and are rather of the order of the corrugation of single atoms. Therefore, the STM data in Fig. 5.6 confirm the decomposition of the molecule.

High-resolution STM images of ordered areas (Fig. 5.7) reveal two different characteristic features: A hexagonal (red hexagon in Fig. 5.7) and a rhombohedral (blue and green frames in Fig. 5.7) structure. Antiphase domain boundaries (*e.g.* trench between blue and green frames in Fig. 5.7) with a width of 3 Å separate growth domains. Both structures have corrugations of about 0.5 Å. The topography observed in Fig. 5.7 changes only slightly with the applied bias voltage in the investigated range of $-2 \text{ V} < V_{\text{Bias}} < 2 \text{ V}$. Therefore, the measured corrugation is mostly of topographic rather than electronic origin. The bright spots in both structures have similar apparent heights above the substrate and

similar corrugations. In spite of the locally ordered areas LEED patterns of the sample images in Fig. 5.7 only show spots belonging to the Au(111)-(1x1) substrate. Thus, after post-annealing to 590 K there is no long-range order for the observed structures.

The morphology in Fig. 5.6 and the observation of two different local structures with different packing density in Fig. 5.7 lead to the conjecture that the state after post-annealing at 590 K is an intermediate state similar to that resulting from the condensation of a 2D lattice gas. Such behavior has previously been reported for alkanethiols on Au(111) [81] and corannulenes on Cu(111) [123]. In order to confirm this conjecture, samples were post-annealed at a slightly higher temperature of 680 K.

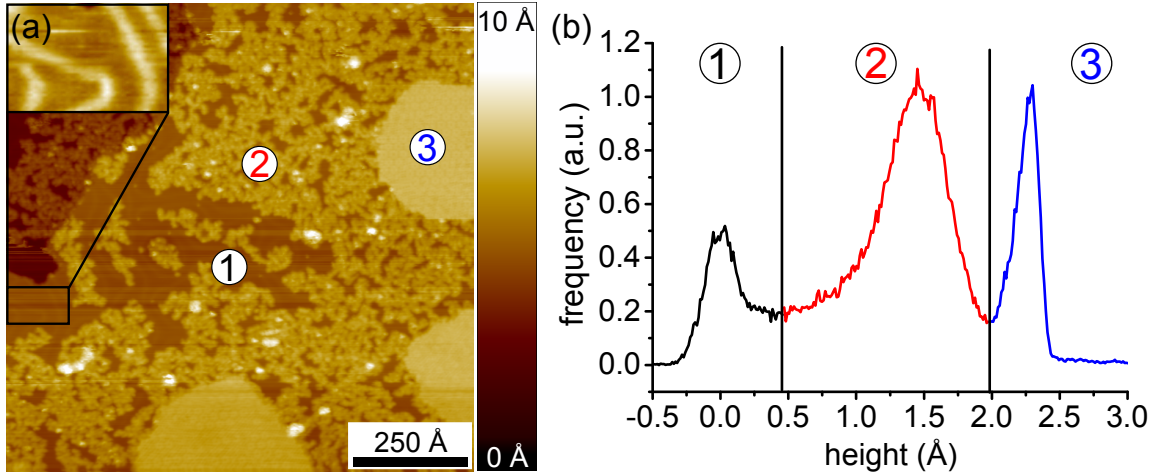


Figure 5.6: Surface morphology after $\{\text{Ni}_4\}$ deposition and post-annealing at 590 K. (a) STM image showing uncovered (1), disordered (2), and ordered (3) areas. The numbers are placed exemplarily on corresponding areas. Inset: A distorted herringbone reconstruction appears in uncovered areas. Image parameters: $100 \text{ Å} \times 1000 \text{ Å}$, $V_{\text{Bias}} = -2 \text{ V}$, $I_{\text{T}} = 1 \text{ nA}$, 5 K. (b) Histogram of the height distribution on the terrace in the right half of the STM image shown in (a).

5.2.3 Post-annealing at 680 K

After post-annealing at 680 K, the samples show only one hexagonal morphology (Fig. 5.8a). The repeating feature of this morphology is a dark central hole surrounded by six bright spots in hexagonal symmetry. The lateral distance between central holes is 9.5 Å , and the corrugation is about 0.5 Å . Similar to the observations after the first annealing step, the STM images are only very weakly dependent on the bias voltage. Even for reversed bias voltage, the center hole remains a hole, indicating that the STM corrugation is mostly of topographic rather than electronic origin. Both properties also agree with those measured after post-annealing at 590 K pointing towards similar origins of the protrusions in all three structures.

LEED patterns still reveal the spots belonging to the Au(111)-(1x1) substrate, but in addition spots forming a $2\sqrt{3} \times 2\sqrt{3}$ superstructure (Fig. 5.8b) are observed. The size and

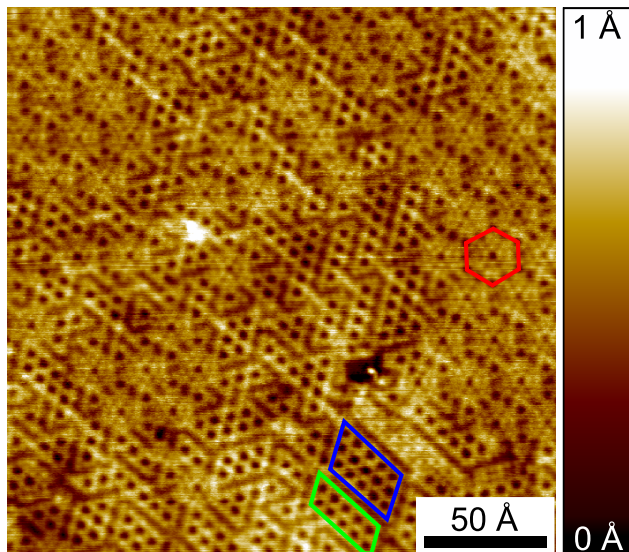


Figure 5.7: High-resolution STM image of an ordered area after annealing at 590 K for 1 h showing a hexagonal (red frame) and a rhombohedral structure (blue and green frames). The rhombohedral patterns are separated by anti-phase domain boundaries. Image parameters: $220 \text{ Å} \times 220 \text{ Å}$, $V_{\text{Bias}} = -1 \text{ V}$, $I_{\text{T}} = 1 \text{ nA}$, 5 K.

symmetry of this superstructure are in good agreement with the STM data. Therefore, the local structure observed in Fig. 5.8a is long-range ordered and covers large areas of the sample surface. STM data do not allow an unambiguous chemical identification of the six alike looking building blocks within the surface unit cell, but by comparison with literature [124] and XPS data, it is safe to conclude that these reconstructions stem from atomic sulfur on Au.

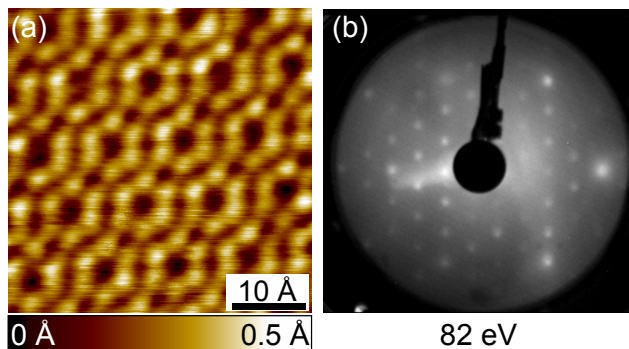


Figure 5.8: High-resolution STM image and LEED pattern after $\{\text{Ni}_4\}$ deposition on Au(111) and post-annealing at 680 K for 1 h. The LEED pattern taken at 82 eV confirms that the local structure observed in the STM image (a) coherently covers large areas on the sample surface. STM image parameters: $40 \text{ Å} \times 40 \text{ Å}$, $V_{\text{Bias}} = -1 \text{ V}$, $I_{\text{T}} = 1 \text{ nA}$, 5 K.

5.2.4 Structure models of the sulfur overlays

Figure 5.9 shows high-resolution STM images and corresponding structure models for the observed regular structures. Figures 5.9a and 5.9c correspond to the rhombohedral and hexagonal structures, respectively, observed in Fig. 5.7 after post-annealing at 590 K for one hour, whereas Fig. 5.9b shows the state after post-annealing at 680 K (Fig. 5.8). The structure in Fig. 5.9a reveals two growth domains. The local structure within one domain can be described as a (2×2) superstructure. The 3-fold hollow site was chosen

as the preferred adsorption site [125]. The following discussion would also hold true, if the adsorbates were sitting on top or bridge sites. The non-occupied sites appear in the STM images as "holes", and the hole-hole distance is in reasonable agreement with twice the Au nearest-neighbor distance on Au(111) of 5.8 Å. The structure model also naturally explains the formation of anti-phase domain boundaries (*e.g.* between the blue and green domains). The structure in Fig. 5.9b is observed after post-annealing at 680 K for one hour and reveals long-range order as discussed in the context of Fig. 5.8. Hence, it is thermodynamically more stable than the other two structures. The $2\sqrt{3} \times 2\sqrt{3}$ R30° reconstruction yields a periodicity of 9.9 Å and consists of interpenetrating rosette-shaped elements, each formed by a central hole surrounded by six triangles spanned by three adsorbates. The triangular arrangement (red triangles) corresponds to the local order of the frequently observed $\sqrt{3} \times \sqrt{3}$ R30° reconstruction of S-functionalized species adsorbed on Au [126]. The hexagonal structure in Fig. 5.9c, finally, is observed in coexistence with the rhombohedral structure (Fig. 5.7) and can be constructed by combining elements from the structures shown in Figs. 5.9a and 5.9b: Rosettes from Fig. 5.9b are here arranged without overlap. The boundaries (solid lines in Fig. 5.9c) consist of a linear arrangement of holes with hole-hole distance of 5.8 Å similar to that of the rhombohedral structure in Fig. 5.9a. The distance between nearest neighbor rosettes (*e.g.* along the dashed line in Fig. 5.9c) measures 9.8 Å similar to the periodicity of the $2\sqrt{3} \times 2\sqrt{3}$ R30° reconstruction in Fig. 5.9b.

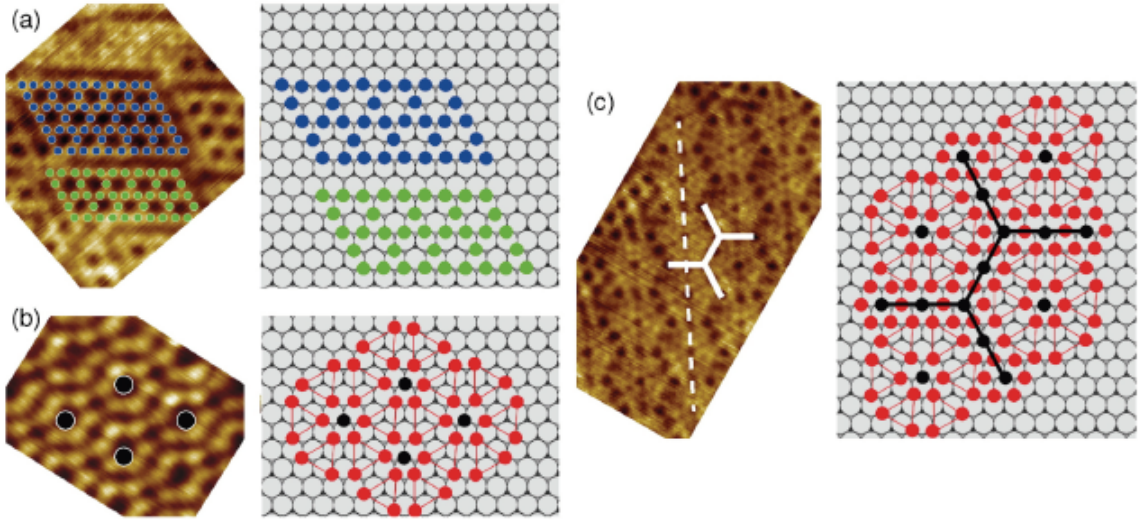


Figure 5.9: Structure models for different sulfur overlayer observed by high-resolution STM. (a) Rhombohedral structure after post-annealing at 590 K marked in Fig. 5.7 by blue and green frames. (b) Long-range ordered hexagonal morphology after post-annealing at 680 K shown in Fig. 5.8. (c) Hexagonal structure after post-annealing at 590 K marked in Fig. 5.7 by a red frame. Red, blue, and green dots correspond to protrusions in the STM images and black dots to "holes". The grey mesh in the models represents the Au(111) surface.

5.3 Conclusion

The adsorption of the cubane-type $\{\text{Ni}_4\}$ SMM with structurally exposed thio-cyclohexane groups on the Au(111) surface has been investigated with STM, XPS and LEED techniques. The organic HL-S ligands decoordinate from the $\{\text{Ni}_4\text{Cl}_{4n}\}$ core during the adsorption of the $\{\text{Ni}_4\}$ molecule, which can be attributed to the released adsorption energy of S on Au. The remaining fragments very likely contribute to the disordered morphology observed by STM in the as-deposited state. Post-annealing above 480 K leads to a decomposition of the initially intact $\{\text{Ni}_4\text{Cl}_{4n}\}$ core and desorption of some fragments, while the remaining Ni- and S-containing parts form a long-range ordered superstructure at 680 K. The stability of the $\{\text{Ni}_4\text{Cl}_{4n}\}$ core up to 480 K indicates that such types of coordination complexes can be tuned to retain their SMM properties exhibited in the bulk as long as the local molecular electrostatic environment does not significantly influence the molecular magnetic anisotropy [127]. Future XMCD studies will show if charge-neutral, thioether-functionalized organic ligands can be used as transporters of highly unstable inorganic structures with appealing electronic and magnetic properties onto metallic substrates, whose interfaces are capable of providing a certain chemical stability to such elusive species (*e.g.* in this case the $\{\text{Ni}_4\text{Cl}_{4n}\}$ building block), not achievable in the bulk.

The results described in this chapter highlight the fragility of the intramolecular, magnetic core-organic ligand interfaces, which are strongly influenced by the substrate surface upon deposition of $\{\text{Ni}_4\}$ from solution. Strategies to stabilize metal-organic complexes on various metallic substrates are

1. strengthening of the metal-ligand bonds by introducing strong π -backbonding organic ligands and/or strongly negatively charged chelating (redox) ligands and
2. reduction of the number of ligands/anchoring groups per complex so that all of them can bind to the substrate surface with no significant molecular deformation or ligand decoordination.

While due the ligand decoordination during adsorption it was not possible to investigate the intact $\{\text{Ni}_4\}$ SMM, it has been shown that this behaviour can be also used to deposit bimetallic clusters [128].

Chapter 6

Fe/W(110) imaged with SP-STM

The low coverage Fe/W(110) system exhibits interesting topographic, electronic and magnetic effects and thus is one of the most studied magnetic thin film systems. Many different methods have been used to investigate Fe/W(110). LEED [129, 130] and STM [131, 132] helped to understand the growth mode, whereas MOKE [133, 134] and SP-STM [132, 103] gave insight into the magnetic properties.

During this PhD thesis 1.5 ML Fe on W(110) were used as magnetic substrate for the deposition of TPT molecules. Before the results from the TPT/Fe/W(110) samples are presented in the next chapter, this chapter discusses the properties of the Fe/W(110) system.

A decisive factor in the Fe/W(110) system is the large lattice mismatch between tungsten ($a_W = 3.165 \text{ \AA}$) and iron ($a_{Fe} = 2.866 \text{ \AA}$) [135] of $(a_W - a_{Fe})/a_W = 9.4 \%$. This enormous strain directly affects the topography and thereby also electronic and magnetic properties. The first four layers of iron on W(110) have considerably different properties. Starting with the fourth layer Fe grows with its bulk lattice constant and its properties are subject to rather small changes. Section 6.1 discusses briefly the growth and the topographical features of Fe/W(110).

Especially the second layer (or double layer, abbreviated: DL) iron on W(110) is well suited for investigating the spin dependent hybridization of molecules on magnetic surfaces by SP-STM. The DL exhibits alternating out-of-plane (OOP) magnetic domains and in-plane (IP) domain walls and thus can be used for characterizing the magnetization direction of SP-STM tips *in-situ*. Furthermore the spacing between domains is small and very regular. Due to this magnetic structure molecules on opposite domains are found routinely and can be easily imaged by STM. Section 6.2 discusses the electronic and magnetic properties of one and two layer thick films of iron on W(110).

Section 6.3 compares STM and SP-STM images of Fe/W(110) obtained with different tips and discusses the resulting differences. The comparison of Fe- and Cr-coated tips with different magnetization directions highlights the variety of magnetic features in the Fe/W(110) system. The characterization of magnetic tips is important for chapter 7.

6.1 Topography and growth of Fe/W(110)

In general, the topographical properties of thin films strongly depend on the lattice mismatch between substrate and heteroepitaxial layer. The degree of mismatch determines if and what type of structural defects occur [131]. Fe/W(110) is a system with a large mismatch of 9.4%. Thus effects resulting from the strain on topography and growth mode have to be expected.

Another important parameter for film growth is temperature. Films grown at room temperature usually have a considerably different morphology than films grown at elevated temperatures. Fortunately, the morphology of films can be changed subsequently by post-annealing. The Fe films grown in this PhD were always post-annealed to achieve a flat and homogenous morphology. Therefore, this section will focus on films grown under such conditions. Fig. 6.1 shows an overview STM image of roughly 2 ML Fe/W(110), which exhibits the first four atomic layers of Fe/W(110).

When iron is deposited on W(110) and post-annealed at temperatures > 570 K it covers the complete surface before the second atomic starts growing [131]. This effects results from different surface free energies ($\gamma_{Fe} = 2.9$ J/m² and $\gamma_W = 3.5$ J/m² [136]), which makes covering the surface first energetically more favorable. The first layer grows pseudomorphic lattice and isotropic [137, 129].

After the first layer is completed the second layer starts growing preferably along the [001] direction, which can lead to the formation of "nanowires" as seen in Fig. 6.1. The growth conditions described in section 4.3.2 (1.5 ML, post-annealed at 500 K) avoided this regime of anisotropic growth and lead to larger and homogeneous regions of the second atomic layer. Stress resulting from the lattice mismatch is released by including additional rows of atoms, which can be seen as dislocation lines along the [001] direction. The separation of these dislocation lines is affected by the shape of the DL area. In big and unobstructed DL areas the dislocation separation is approximately 4.6 nm [131] as seen in Fig. 6.3a and Fig. 6.4a. In DL nanowires grown along tungsten step edges (*e.g.* Fig. 6.6a) the separation can strongly vary and reaches values of up to 20 nm. Such morphologies are ideal for the investigation of molecules, since less molecules are close to dislocation lines and more can be found on defect-free regions, allowing reproducible measurements and comparison with DFT calculations. Dislocation lines allow an easy identification of the DL Fe/W(110) itself and the the crystallographic directions by STM.

All layers above the second layer start growing before the previous layer is completed. In the third layer additional dislocation lines along [001] are introduced with a rather regular separation of 2.7 nm [131]. The growth is still anisotropic in [001] direction. Starting from the fourth layer, a 2D dimensional dislocation network is formed and the Fe grows fully relaxed. The formation of a 2D network is explained by the insertion of an iron atom roughly every ninth row to compensate for strain, which leads to a Moirée pattern [131]. In contrast to the second and third layer, the fourth layer grows again isotropic.

As can be seen in Fig. 6.1, by depositing roughly 2 ML iron on W(110), already the third and fourth atomic layer started to form. However, for the investigation of TPT large an homogenous areas of DL Fe were desired. Such morphologies (as shown in Fig. 6.3a, 6.4a and 6.6a) were best found when depositing only 1.5 ML Fe according to the procedure

described in section 4.3.2.

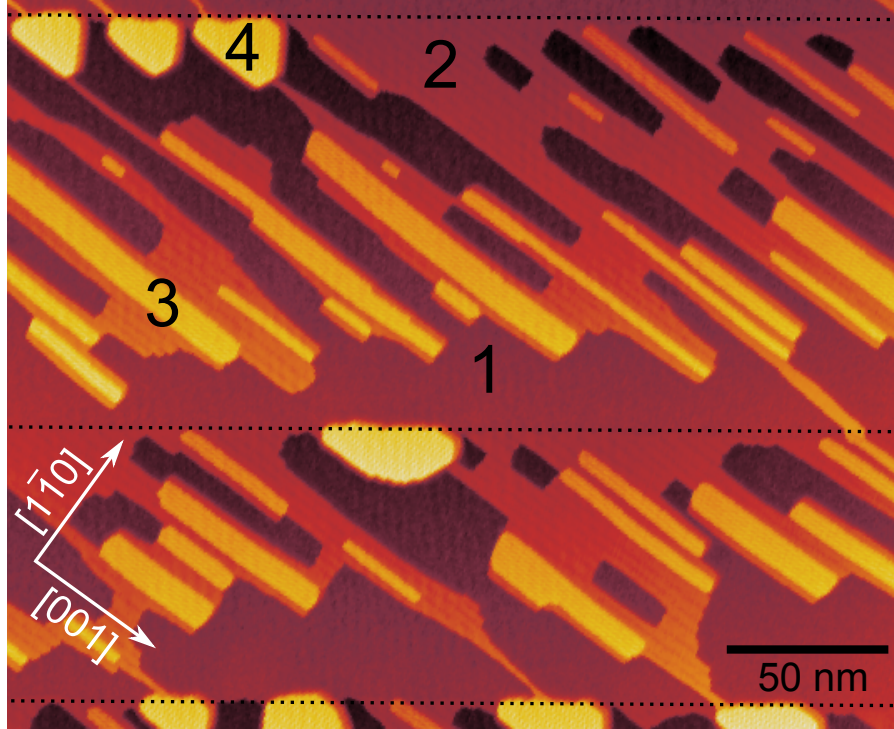


Figure 6.1: Typical morphology of an Fe thin film on W(110). Numbers indicate respective atomic layer of Fe. Dotted lines indicate steps of the W(110) substrate. STM image parameters: $262 \text{ nm} \times 214 \text{ nm}$, $V_{\text{Bias}} = -1 \text{ V}$, $I_{\text{T}} = 1 \text{ nA}$, 78 K .

6.2 Electronic and magnetic properties

Samples with the first and second atomic layer iron on W(110) were used as a magnetic substrate for the deposition of TPT molecules. Previous studies on similar systems [16, 65] indicate that the electronic properties of adsorbed molecules are largely affected by the substrate surface. Thus the fundamental electronic and magnetic properties of the first and second layer iron on W(110) will be discussed in this section.

The DOS of the first layer Fe/W(110) around the Fermi level is characterized by broad bands with an empty-state peak at 400 meV [103]. Spin polarized tunnel spectra show only small asymmetries for opposite magnetic domains (red and green curves in Fig. 6.2c).

The magnetization of the magnetic domains of first atomic layer Fe/W(110) are IP along the $[1\bar{1}0]$ direction [133]. Fig. 6.2a and b show a SP-STM topography image and a dI/dV -map respectively of the monolayer (ML) Fe/W(110) system. Two opposite domains are marked by the white arrows in Fig. 6.2b. The domain walls do not follow any preferred crystallographic direction as can be seen later in Fig. 6.4b and 6.6b. The Curie temperature for one layer iron on W(110) is 230 K [61].

The DOS of the second layer Fe/W(110) around the Fermi level is dominated by two d_{z^2} -like states at -80 meV and 700 meV [103]. Both peaks show significant asymmetries in spin polarized tunnel spectra (ocher and purple curves in Fig. 6.2c). The DOS at other energies varies slightly in literature [103, 107, 138, 139]. This variation can be attributed to electronic states of the tip. STS spectra with different tips will almost always be slightly different, since it is basically impossible to achieve completely identical tip conditions in experiments. Compared to the main peaks at -80 meV and 700 meV these variations are less pronounced and once identified tip states can be excluded from further analysis.

The magnetic structure of the second layer Fe on W(110) is very complex and includes both IP and OOP elements. Many different techniques, both experimental and theoretical, were necessary to completely understand the magnetism of the DL Fe/W(110). The first studies concerning the magnetic properties of the Fe/W(110) system were performed with MOKE. The first and third layer showed an IP magnetization, whereas for the second layer an OOP magnetization was observed [134].

The next steps in understanding the magnetic properties of DL Fe/W(110) were performed with SP-STM [138, 102]. Using tips with different magnetization directions revealed OOP oriented domains and IP oriented domain walls [102]. Depending on the particular Fe morphology different phenomena were observed. On W(110) substrates with high miscuts, the DL grows preferably along the step edges and thus forms nanowires. Such nanowires are either single domain or have magnetic domains with an average length of some 100 nm. In order to reduce the magnetic stray field energy such nanowires are usually oriented antiparallel to their neighbors and thus lead to a "terrace wise antiferromagnetism" [138].

In large and unobstructed areas of DL Fe the domains are typically 50 ± 5 nm wide [102]. The domain walls propagate fairly strictly along the $[1\bar{1}0]$ direction and are on average 7 nm wide [140]. Such a morphology is shown in Fig. 6.2a. The corresponding dI/dV-map in Fig. 6.2b shows domains and domain walls of the DL Fe/W(110) system. Due to the lack of magnetic fields in the early microscopes it was not possible to determine the actual domain wall type, *i.e.* Bloch- or Néel-type¹.

Eventually a combination of SP-STM with a triple axis vector magnet and micromagnetic simulations [141, 142] were able to reveal the exact magnetic behaviour of the DL Fe/W(110) system. SP-STM unveiled that the magnetization direction rotates like an inhomogenous right rotating cycloidal spiral. The domain walls are thus of Néel-type. Micromagnetic simulations confirmed that this certain type of rotation direction is induced by the Dzyaloshinskii-Moriya-Interaction (DMI) [141].

The DMI [143, 144] is an antisymmetric exchange interaction, which contributes to the total magnetic exchange interaction in systems with broken inversion symmetry. The DMI contribution can be expressed as:

$$H_{\text{DM}} = \mathbf{D}_{ij} \cdot (\mathbf{S}_i \times \mathbf{S}_j) \quad (6.1)$$

with the DMI vector \mathbf{D}_{ij} only being unequal to zero in systems with broken inversion symmetry. The microscopic origin of the DMI is the spin-orbit coupling. Consequently,

¹In Bloch-type domain wall the magnetic moments rotate about the axis perpendicular to the wall. In Néel-type domain walls the magnetic moments rotate along the axis of the wall.

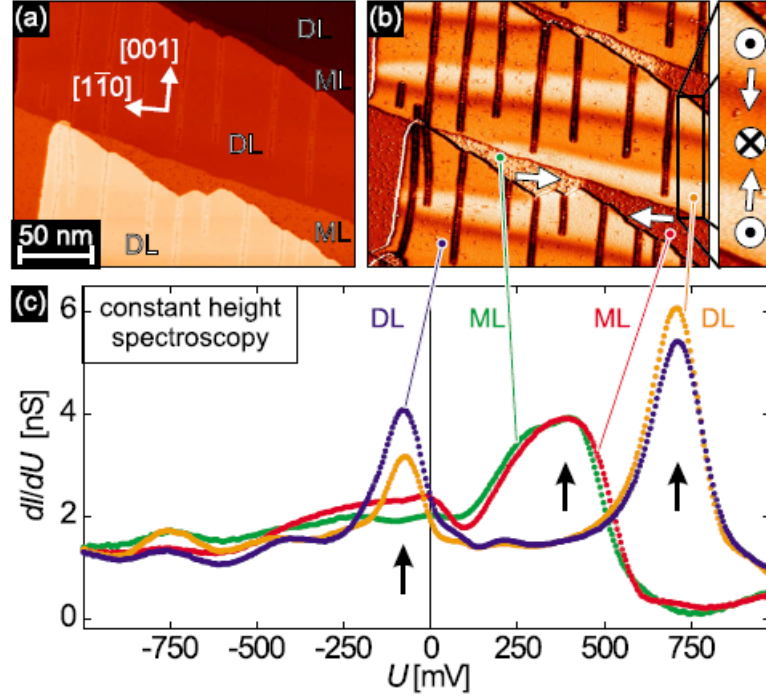


Figure 6.2: (a) Topography image of 1.5 ML Fe/W(110), taken with a bulk Cr tip at $V_{\text{Bias}} = 100$ mV. ML and DL areas are visible. (b) Simultaneously recorded dI/dV map, revealing magnetic contrast on the ML domains, the DL domains, and the DL domain walls. The magnetization structure on the ML and the DL is sketched within the map and the zoom inset, respectively. (c) Constant height spectroscopy above two different ML and two different DL domains (stabilization parameters: $V_{\text{Bias}} = -1000$ mV, $I_T = 2$ nA). A typical empty-state peak at $V_{\text{Bias}} = 400$ mV is visible for the ML, whereas two peaks caused by d_{z^2} -like states are resolved on the DL at $V_{\text{Bias}} = -80$ mV and $V_{\text{Bias}} = 700$ mV (positions marked by arrows). Taken from [103].

the DMI manifests itself only in systems with strong spin-orbit coupling. From Eq. 6.1 it becomes clear that the DMI favors a perpendicular orientation of spins.

As a result DMI drives the formation of spin spirals at surfaces if it is strong enough to compete with magnetic exchange and anisotropy:

$$|\mathbf{D}_{ij}| > D_c := \frac{4}{\pi} \sqrt{AK} \quad (6.2)$$

with A and K being the exchange stiffness and the anisotropy constant, respectively [142, 141]. For $|\mathbf{D}_{ij}| < D_c$ the magnetic ground state is collinear [145].

Exemplarily, one atomic layer manganese on W(001) is a system with $|\mathbf{D}_{ij}| > D_c$. Here, an homogenous spin spiral is formed, which means that the angle between any two neighboring magnetic moments is constant along the propagation direction of the spin spiral [146]. In contrast, micromagnetic simulations yielded only $|\mathbf{D}_{ij}| \approx 0.65 D_c$

in the DL Fe/W(110) system [141]. Therefore the DMI is not large enough to induce a homogenous spin spiral. However, the single domain state is destabilized by dipolar interaction giving rise to domains and domain walls. DMI then defines the rotational sense of the magnetization direction in these domain walls [141]. The rotation of the magnetization in the DL Fe/W(110) system is shown in Fig. A.4a in the appendix.

6.3 Fe/W(110) imaged with different STM tips

The appearance of Fe/W(110) in STM depends significantly on which type of tip is used and whether it is sensitive to magnetic components. The following sections compare the ML and DL Fe/W(110) imaged with tips without magnetic sensitivity, in-plane (IP) and out-of-plane (OOP) magnetic sensitivity.

6.3.1 Tips without magnetic sensitivity

Experiments are conducted in a step-by-step fashion. After one step can be reliably controlled, one can move to the next step. The difficulties in the fabrication process of magnetic STM tips have been discussed in section 4.4.2. If a tip is magnetic and in which particular direction, is never completely unambiguous after fabrication and can be only determined by experiment. Since also sample fabrication is nontrivial it is necessary to establish a preparation procedure for high quality samples first. Thus the first sample characterizations are performed with non-magnetic tungsten tips, which are known to be reliable tools for achieving high quality STM images.

The magnetic properties of thin films are very sensitive to contamination. Standard STM allows to estimate the cleanness of samples but is not sensitive to magnetic structures. However, the DL Fe/W(110) system offers a possibility to determine the magnetic state (*i.e.* magnetic or non-magnetic) of the sample with standard STM. The spin-orbit-interaction (SOI) leads to a mixing of states with d_{xy+xz} and d_{z^2} in domain walls [147]. This mixing locally changes the DOS and can be imaged with dI/dV-maps at $V_{\text{Bias}} = 50 \text{ meV}$. Other magnetic features in the Fe/W(110) system, however, can only be observed with magnetic tips.

Fig. 6.3a shows a typical example of an high quality 1.5 ML Fe/W(110) film. Both ML and DL patches are observed. The prominent dislocation lines (marked by black arrows) allow an easy identification of the DL and crystallographic directions. The remaining DL area appears flat and without additional features, as expected for a non-magnetic tip. Fig. 6.3b shows the corresponding dI/dV-map which reproduces all features described in the topography image, but additionally shows lines propagating along the $[1\bar{1}0]$ direction. These lines are identified as domain walls according to [147] and confirm the samples to be suitable for magnetic investigations.

The images in Fig. 6.3 were in fact obtained with a bulk Cr tip. However, a clear absence of tip magnetization was confirmed by neither observing domains nor domain walls with alternating contrast. This observation highlights the challenges involved in preparing magnetic STM tips. The images obtained with this bulk chromium tip without magnetic sensitivity are qualitatively similar to images obtained with standard tungsten tips.

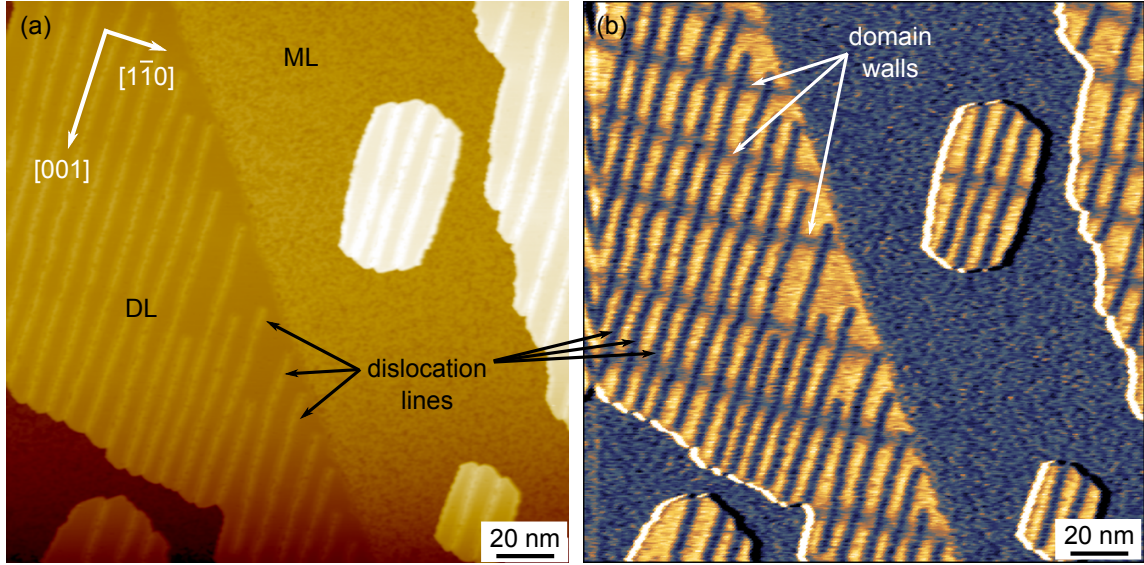


Figure 6.3: Overview STM images showing 1.5 ML Fe/W(110) imaged with a non-magnetic tip. (a) topography and (b) corresponding dI/dV map recorded with a non-magnetic tip. $200 \text{ nm} \times 200 \text{ nm}$, $V_{\text{Bias}} = 50 \text{ mV}$, $I_{\text{T}} = 1 \text{ nA}$, 5 K .

6.3.2 Fe-coated tips

As described in section 4.4.2 different methods were used to fabricate magnetic tips. Fig. 6.4a shows the topography image of a 1.5 ML Fe/W(110) sample which was obtained by using an Fe-coated (approximately 15 ML) tungsten tip. In this particular area mostly ML and DL areas with several small nanowires of the third layer have formed. Fig. 6.4b shows the simultaneously recorded dI/dV-map on which all magnetic features of the 1.5 ML Fe/W(110) system are observed: IP domains in the ML (marked by black arrows), OOP domains (marked by circles) and IP domain walls (marked by white arrows) in the DL. The fact that both IP and OOP magnetic features are observed results from a tilted tip magnetization direction and confirms the capability of Fe-coated tips to achieve full magnetic sensitivity² (*i.e.* being sensitive to both IP and OOP magnetic features). It is interesting to note how the nanowires of the third layer affect the magnetization direction in the neighbouring Fe DL film. Apparently they pose obstacles for the magnetic domains and lead to a discontinuous domain propagation.

After careful analysing Fig. 6.4a it becomes clear that the magnetic structure is partially visible in the topography image too. The line profiles, taken at the area indicated by the black rectangle in Fig. 6.4a and the corresponding area in Fig. 6.4b, are shown in Fig. 6.5. The line profile belonging to Fig. 6.5a (black line in Fig. 6.5) shows a periodic height variation of roughly 20 pm. The dI/dV line profile shows two plateau-like levels separated by dips of varying intensity. The plateaus result from the OOP domains and the dips from

²All visual indicators are meant to illustrate OOP and IP magnetization directions. The determination of the real magnetization direction requires applying external magnetic fields.

the alternating domain walls.

Comparing both line profiles (Fig. 6.5b) (blue line in Fig. 6.5), reveals that the domain walls are responsible for the height variations in the topography image. Thus, this observation demonstrates a dominating in-plane magnetization direction typical for Fe-coated tips [37, 148]. A determination of the exact tip magnetization direction using the formula derived in [103] was prevented by a non ideal sample morphology (*i.e.* very small dislocation line separation) and using bias voltages were both SOI and magnetic contributions from the domain walls are present as illustrated in Fig. A.4 in the appendix. Both STM images and lineprofiles are in good agreement with previous reports of using Fe-coated tips on Fe/W(110) [102].

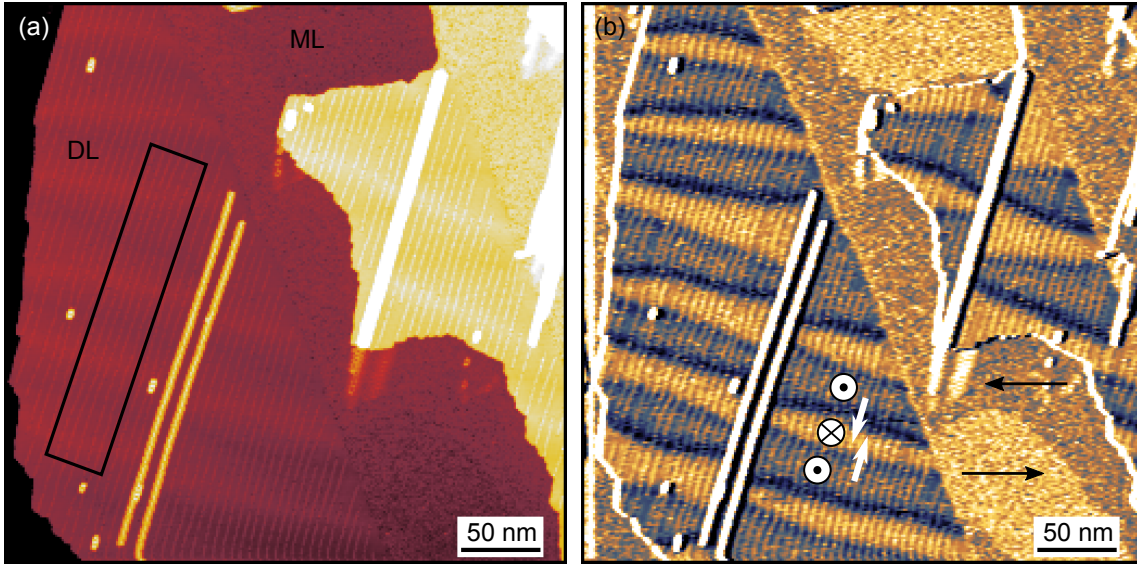


Figure 6.4: Overview SP-STM images with full spin sensitivity showing 1.5 ML Fe/W(110) obtained with an Fe-coated tungsten tip. (a) topography and (b) corresponding dI/dV map. STM image parameters: 350 nm \times 350 nm, $V_{\text{Bias}} = -100$ mV, $I_T = 1$ nA, 5 K.

6.3.3 Cr-coated tips

Although Fe-coated tips demonstrated full spin sensitivity, their strong IP magnetization direction is not ideal for the investigation of TPT on the OOP magnetized domains of the Fe DL. It is known from literature that Cr-coated tips usually exhibit an OOP magnetization direction [16, 37, 106]. A topography image of a 1.5 ML Fe/W(110) sample obtained by using a Cr-coated (10 ML) tip is shown in Fig. 6.6a. This particular area exhibits long DL nanowires along the W(110) substrate step edges with strongly varying dislocation line separation. The dI/dV-map (Fig. 6.6b) reveals full spin sensitivity: IP domains in the ML (red arrows), OOP domains (white circles) and IP domain walls (white arrows) in the DL. In contrast to Fig. 6.4a, where the IP magnetized domain walls are visible in the topography image, Fig. 6.6a shows significant height variations for the OOP magnetized domains due

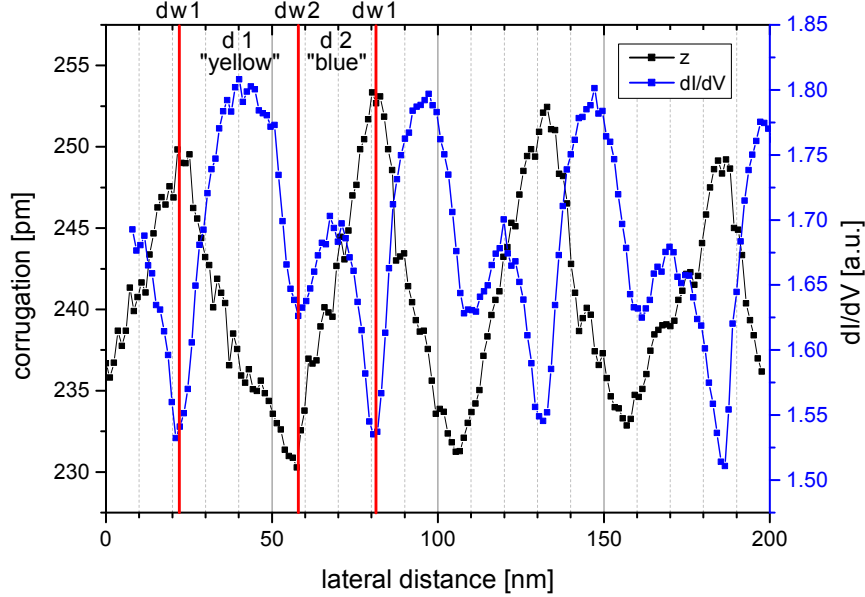


Figure 6.5: Line profiles showing the magnetic structure of the Fe DL imaged with a mostly IP sensitive Fe-coated tip. The line profiles were taken at the area indicated by the black rectangle in Fig. 6.4a (black line) and corresponding area in Fig. 6.4b (blue line) and are averaged over 26 parallel lines. The red lines indicate the position of domain walls (dw 1 and dw2) and separate opposite magnetic domains (d1 and d2). Domains with the same magnetization direction as d1 (d2) are colored yellow (blue) in Fig. 6.4b.

to the TMR. Thus, the expected strong OOP magnetization direction of Cr-coated tips was confirmed, which made them ideal for investigating TPT on DL Fe/W(110).

In order to understand the imaging properties of Cr-coated tips better, the area marked by the black square in Fig. 6.6a was subsequently imaged with different bias voltages. The results are presented in Fig. 6.7. The topography images at different bias voltages in Fig. 6.7a-c show considerable contrast changes. The apparent height difference between neighboring domains is explained by the TMR (refer to section 2.5):

- "Bright" domains stem from a parallel alignment of tip and sample magnetization. A parallel alignment results in high currents. Thus the tip retracts from the sample in constant current mode.
- "Dark" domains stem from an anti-parallel alignment of tip and sample magnetization. An antiparallel alignment results in small currents. Thus the tip approaches the sample in constant current mode.

With changing bias voltages contrast in the domains itself changes, but the alignment of tip and sample magnetization does not change (*i.e.* the dark domain is always darker) for the investigated bias voltages. In contrast to the images obtained with Fe-coated tips, the domain walls were not visible in the topography images. The dI/dV-maps (Fig. 6.7d-f)

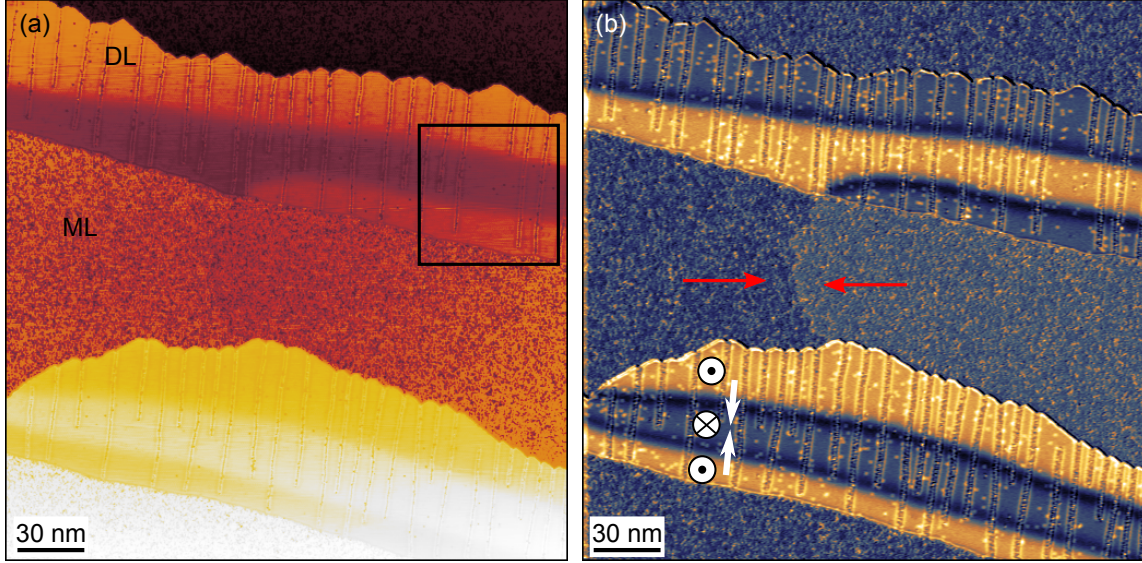


Figure 6.6: Overview SP-STM images with full magnetic sensitivity showing 1.5 ML Fe/W(110) obtained with a Cr-coated tungsten tip. (a) topography and (b) corresponding dI/dV map. STM image parameters: $250 \text{ nm} \times 250 \text{ nm}$, $V_{\text{Bias}} = -100 \text{ mV}$, $I_{\text{T}} = 1 \text{ nA}$, 5 K .

show a strong bias voltage dependency with Fig. 6.7e showing a reversed contrast when compared to either Fig. 6.7d or f. This contrast reversal indicates a change in local spin polarization. Additionally to the OOP domains, IP domain walls are visible in Fig. 6.7d as dark bands. However, since no alternating contrast is observed, the visibility of the domain walls is a result of the additional SOI contribution similar to Fig. 6.3b.

As explained in section 2.5 the height difference between neighboring domains can be used to estimate the effective spin polarization of the tip-sample junction [35]:

$$P_{\text{eff}} = \frac{\exp(A\sqrt{\phi}\Delta s) - 1}{\exp(A\sqrt{\phi}\Delta s) + 1} \quad (6.3)$$

with several natural constant simplified to $A \approx 1 \text{ eV}^{-1/2} \text{ \AA}^{-1}$, the mean local tunnel barrier height usually assumed as $\phi \approx 4 \text{ eV}$. Thus line profiles were taken at the positions indicated by the color coded lines in the topography images in Fig. 6.7a-c and at the respective position for the dI/dV-maps. Fig. 6.8a shows the line profiles of the topography images and reveals a total height difference between neighboring domains of roughly 25 pm for Fig. 6.7a and b, and 10 pm for Fig. 6.7c. Δs in Eq. 6.3 denotes the difference between average and maximum or minimum domain height respectively [35] as shown for the black curve in Fig. 6.8a. This leads to an effective spin polarization of 12.4% in the cases of $V_{\text{Bias}} = \pm 100 \text{ mV}$ and 5% for $V_{\text{Bias}} = 700 \text{ mV}$ respectively.

Thus, the line profiles in Fig. 6.8a reveal a highly energy dependent effective spin polarization P_{eff} (Eq. 2.18) of the tip-sample junction. The higher effective spin polarization

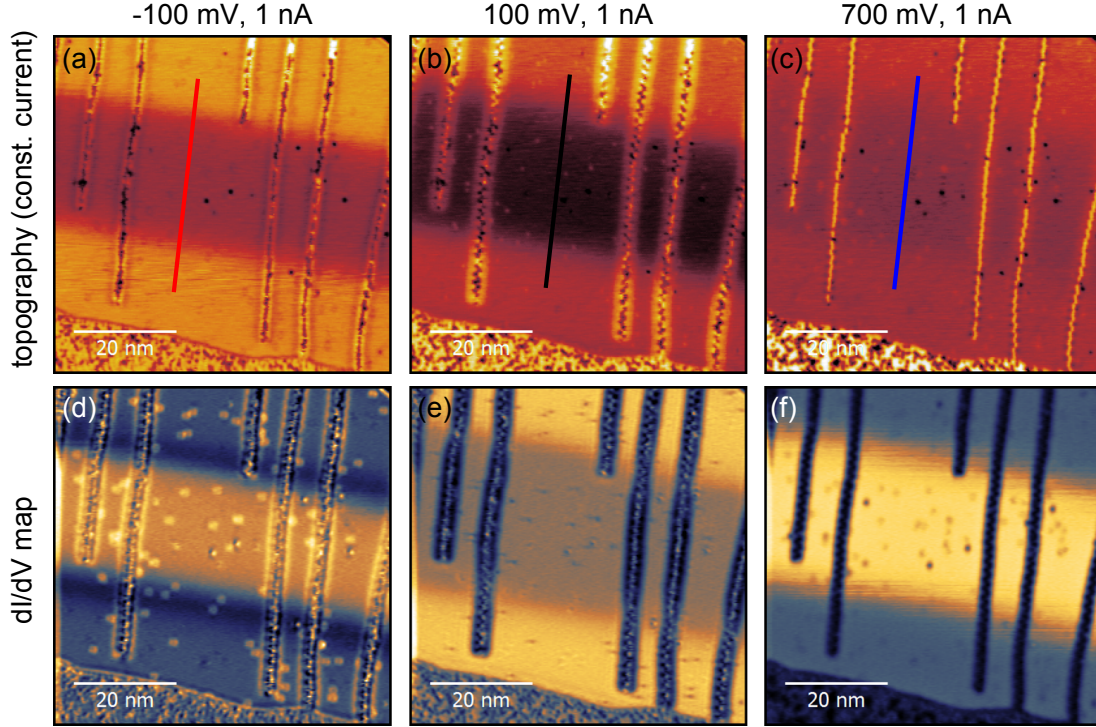


Figure 6.7: Area marked by black square in Fig. 6.6a imaged with different bias voltages. STM image parameters are given in the image. All images are $65\text{ nm} \times 65\text{ nm}$ and were measured at 5 K.

at low bias voltages can be understood by considering the electrode materials (*i.e.* tip and sample) DOS. Iron exhibits a strongly spin-polarised DOS at the Fermi level. Chromium is a $3d$ antiferromagnetic material and consequently, a free-standing layer of Cr or the surface layer of a Cr-coated tip, exhibits a high spin polarization at the Fermi level too. Although previous reports [103] revealed that the d_{z^2} -like state at 700 mV is highly spin polarized in itself, the effective spin polarization at this energy is rather low.

This behaviour can be understood by investigating the dI/dV lineprofiles in Fig. 6.8b. The dI/dV -maps were recorded with the same lock-in amplifier settings ($30\text{ mV}_{\text{RMS}}$, 4111 Hz) and thus are directly comparable. The change in signal varies between 10 % for Fig. 6.7d and e, and roughly 100% for Fig. 6.7f. This confirms the high degree of spin polarization in the energy intervall around 700 mV as reported in [103]. The low effective spin polarization can be understood by comparing Fig. 6.7e and f. While the central domain in Fig. 6.7e is dark, it is bright in Fig. 6.7f. Thus, a reversal of spin polarization in the energy interval [100 mV, 700 mV] can be concluded ³. The integration over states with opposite spin polarization leads to a low effective spin polarization in the 700 mV case.

³It should be noted, that SP-STM images are highly tip dependent. Thus a direct comparison between different experiments is generally difficult. For example the SP-STs measurements in Fig. 6.2c show opposite spin contrast for -100 mV and 700 mV, whereas the images in Fig. 6.7 show the same contrast.

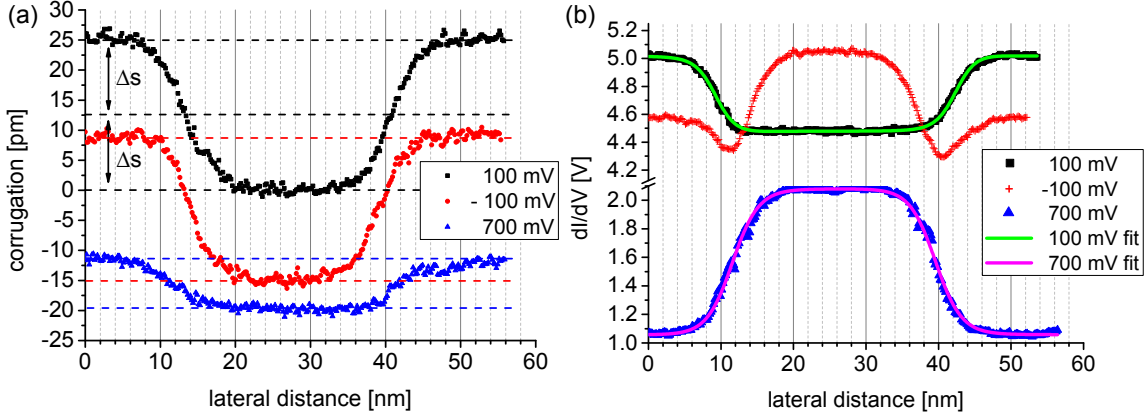


Figure 6.8: (a) Line profiles obtained from the topography images in Fig. 6.7a-c. (b) Line profiles from the dI/dV-maps in Fig. 6.7d-f as well as the results of the fit using Eq. 6.4.

Furthermore the dI/dV line profiles in Fig. 6.8b allow to estimate the magnetization direction of the tip and the domain wall width by fitting the experimental data with the following formula [103]:

$$I(x) = I_0 + I_{\text{sp}} \cdot \cos \left(\theta + \sum_{i=1}^2 \arccos \left[\tanh \frac{x - x_i}{w/2} \right] \right) \quad (6.4)$$

I_0 and I_{sp} denote the spin averaged and spin polarized contribution to the dI/dV signal. w is the domain wall width and x_i the lateral position of the respective domain wall. If we consider the measurement to be performed along the x -direction and the tip to be positioned above the sample in z -direction, θ denotes the angle between surface normal and tip magnetization direction projected onto the $x - z$ plane. As a result the azimuthal component of the tip magnetization direction is neglected [140]. By neglecting the azimuthal component Eq. 6.4 tends to underestimate the true angle between tip magnetization direction and surface normal as has been shown in [107]. Nevertheless Eq. 6.4 gives a good approximation of the tip magnetization direction.

The absence of pronounced domain walls in the dI/dV lineprofiles indicates already a nearly complete OOP tip magnetization. The dI/dV lineprofiles obtained at $V_{\text{Bias}} = 100$ mV and $V_{\text{Bias}} = 700$ mV can be very nicely fitted with Eq. 6.4 (green and magenta lines in Fig. 6.8b) and confirm this conjecture. The qualitative agreement between experimental data and fit for $V_{\text{Bias}} = 100$ mV is shown in Fig A.3 in the appendix. The results for θ , w , y_0 and y_{sp} as well as the standard error of the fit procedures are listed in Table 6.1.

In the cases of A1 and B1 all fit parameters in Eq. 6.4 were free. This leads in A1 to a domain wall width w of 7.1 nm which is in excellent agreement with previous literature [103, 140] and a nearly complete OOP tip magnetization direction of 1.4° . In B1, a domain wall width w of 5.4 nm and a tip magnetization direction of 6.7° is found. Surprisingly, the obtained values for θ and w in A1 and B1 do vary from each other outside of their respective standard errors. Since w and θ do not depend on the energy in Eq. 6.4, deviations of both

case	V_{Bias}	w	θ	I_0	I_{sp}
A1	700 mV	7.1 ± 0.1 nm	$1.4 \pm 1.1^\circ$	1.56	0.51
B1	100 mV	5.4 ± 0.1 nm	$6.7 \pm 1.1^\circ$	4.74	0.27
B2	100 mV	fixed at 7 nm	$4.5 \pm 1.4^\circ$	4.75	0.28

Table 6.1: Results of fitting the experimental data with Eq. 6.4. w denotes the domain wall width, θ the angle between surface normal and tip magnetization direction. I_0 and I_{sp} denote the spin averaged and spin polarized contribution to the line profile. The standard error for I_0 and I_{sp} was lower than $2 \cdot 10^{-3}$ in all cases. In the cases A1 and B1, all parameters of Eq. 6.4 were free, while in B2 the domain wall width was explicitly set to 7 nm. A1 and B1 are plotted in Fig. 6.8b as magenta and green line respectively.

quantities with varying bias voltages are not expected. Similar observations have been made in [149], where they suggested different decay lengths of the contributing electronic states.

The deviation in θ can be explained by plotting Eq. 6.4 for different values of θ (Fig. A.2a,b in the appendix). For small values these curves deviate only very little. Thus small deviations in θ might still lead to reasonable fits. If one sets the domain wall width to the expected value of 7 nm [103, 140] as done in case B2 in table 6.1, the resulting curve still fits within 1 % deviation to the experimental data (Fig. A.3 in the appendix). Furthermore fit B2 yields $\theta = 4.5^\circ$ which almost agrees to the value found in A1 within the standard error. A considerable change of the tip magnetization direction during experiment can be ruled out in this particular case.

In the case of $V_{\text{Bias}} = -100$ mV it was not possible to achieve a reasonable agreement between fit and experimental data due to the additional dips at the domain wall positions. The dips are attributed to the additional SOI contribution to the DOS in domain walls at this particular bias voltage [147]. In this sense, a small additional SOI contribution at $V_{\text{Bias}} = 100$ mV or $V_{\text{Bias}} = 700$ mV could possibly also explain the differences in θ and w derived by the fits in Table 6.1.

As a result of all previous observations the suitability of Cr-coated tips for the following SP-STM experiments is established. A strong OOP magnetization direction and a high effective spin polarization make Cr-coated tips ideal tools for investigating the spin dependent hybridization of TPT on DL Fe/W(110).

6.4 Conclusion

The Fe/W(110) system exhibits compelling electronic and magnetic properties. It is an excellent choice for studying the spin dependent hybridization of aromatic molecules with magnetic surfaces by SP-STM.

In order to understand the properties of such hybrid systems, detailed knowledge of the substrate's properties are required. Thus this chapter introduced the growth mode and topography of Fe/W(110) in section 6.1 and discussed in the following section the electronic

and magnetic properties.

The low coverage regime of first and second layer Fe/W(110) exhibits elements with IP and OOP magnetization. Thus Fe/W(110) is ideal for an *in situ* characterization of SP-STM tips. In section 6.2 Fe/W(110) was investigated with different tips. Depending on the their respective magnetization direction Fe/W(110) can appear considerably different.

Fe-coated tips were found to exhibit a magnetization direction with a strong IP component. Although full magnetic sensitivity was achieved, the strong IP magnetization direction is not ideal for investigating OOP magnetized structures as is intended in the following chapter. In contrast Cr-coated tips revealed a strong OOP magnetization and a high effective spin polarization. Thus the suitability of Cr-coated tips for SP-STM investigation of TPT on the OOP magnetized domains of the DL Fe/W(110) in the next chapter could be established.

Chapter 7

TPT on Fe/W(110)

The spin dependent hybridization of molecules with magnetic surfaces was observed for the first time by Iacovita *et al.* [65] in 2008 and has attracted considerable scientific interest since then. The idea of using molecules to design the local spin polarization at organic-ferromagnetic interfaces was proposed by Atodiresei *et al.* [16] in 2010. Since then the topic has been picked up by experimentalists and theoreticians worldwide. Key reports on the spin dependent hybridization of non-magnetic aromatic molecules on magnetic surfaces include the SP-STM experiments of Brede *et al.* [68], the IMR transport measurements in macroscopic devices by Raman *et al.* [17] and DFT simulations on hybrid-molecular magnets by Callsen *et al.* [48].

The investigation of the polyaromatic TPT on the DL Fe/W(110) promises new insights into the spin dependent hybridization of molecules on ferromagnetic surfaces. Understanding the spin dependent hybridization is important for tuning the spin polarization at organic-ferromagnetic interfaces and the formation of hybrid-molecular magnets. Especially the presence of different aromatic rings in one molecule has not been investigated in the context of spin dependent hybridization. Under the assumption of different coupling strengths, TPT on DL Fe/W(110) could potentially lead to a hybrid-molecular magnet with multiple individually switchable units.

A combination of SP-STM and DFT simulations was employed to thoroughly investigate the TPT/Fe/W(110) system. SP-STM allows to probe the electronic and magnetic properties of nanoscopic objects with unparalleled spatial precision. As such, it is ideally suited for studying hybrid-molecular magnets. The electronic properties were furthermore scrutinized by *ab initio* DFT simulations performed by Rico Friedrich, Vasile Caciuc and Nicolae Atodiresei in the Peter Grünberg Institute 1. In this context, DFT simulations are beneficial in explaining the STM data and potentially reveal additional effects which STM might not be able to. The combination of both methods allows a deep understanding of the TPT/Fe/W(110) system which is bigger than the sum of its parts.

The first step in investigating the TPT/Fe/W(110) system is determining the general adsorption properties such as the adsorption position and its dependency on the substrate temperature in section 7.1.1. Interestingly a highly non-symmetric adsorption geometry is found, which leads to the formation of chiral hybrid-molecular magnets. DFT simulations

were used to calculate the adsorption energies of multiple adsorption geometries.

After the adsorption position and geometry is determined, the second section investigates the spin-integrated electronic properties of TPT on DL Fe/W(110). The electronic properties give insights into the hybridization strength and reveal a first impression of the highly site dependent DOS of the hybrid-molecular magnet.

The third section shows TPT on DL Fe/W(110) imaged by SP-STM. The appearance of TPT on opposite magnetic domains is significantly different, which is a clear indication for a spin dependent hybridization. In order to compare molecules on opposite domains the respective adsorption position needs to be determined again. Furthermore, potential interactions between the magnetic substrate and hybrid-molecular magnet with different chirality are investigated.

In the following section, high resolution SP-STM images of TPT on opposite magnetic domains are used to investigate the site and energy dependent effective spin polarization of the hybrid-molecular magnet. A comparison with DFT simulations reveals a qualitative agreement. The results showcase the possibilities of designing the spin polarization of organic-ferromagnetic interfaces.

7.1 Adsorption of TPT on Fe/W(110)

Studying the adsorption characteristics of TPT on Fe/W(110) is a prerequisite for the investigation of the system’s electronic and magnetic properties. The adsorption position and geometry was characterized by high resolution STM images and compared with DFT calculations.

7.1.1 Adsorption characteristics

TPT was originally deposited on the Fe/W(110) substrate held at room temperature. STM images from such samples showed that TPT on the ML appears to be randomly oriented, whereas on the DL it is only found at dislocation lines (Fig. 7.1a). Since evaporation should lead to an homogenous distribution, this observation reveals that TPT is mobile on DL Fe/W(110) at room temperature and moves to the more reactive dislocation lines. In the case of dioxin ($\text{C}_4\text{O}_2\text{H}_4$) DFT calculations showed that the adsorption energy on the ML Fe/W(110) (3.2 eV) is considerably higher than for the DL Fe/W(110) (2.29 eV) [150]. Although diffusion does not depend on the adsorption energy, but on the energy difference ΔE necessary to move from one position to another, the adsorption energy usually gives a good indication for the mobility of adsorbates. A similar behaviour for TPT/Fe/W(110) could explain the increased mobility on the DL Fe/W(110).

For reproducible results it is necessary to study TPT on a defect-free surface. When deposited on a pre-cooled Fe/W(110) substrate (roughly 170 K) TPT was found on defect-free DL areas in-between dislocation lines. Fig. 7.1b shows the resulting morphology. Even after TPT evaporation samples are very clean and intact TPT molecules are easily identified by their "Y"-shape. Virtually no molecule fragments are observed which shows the high purity of the original TPT powder and confirms a high thermal stability up to the

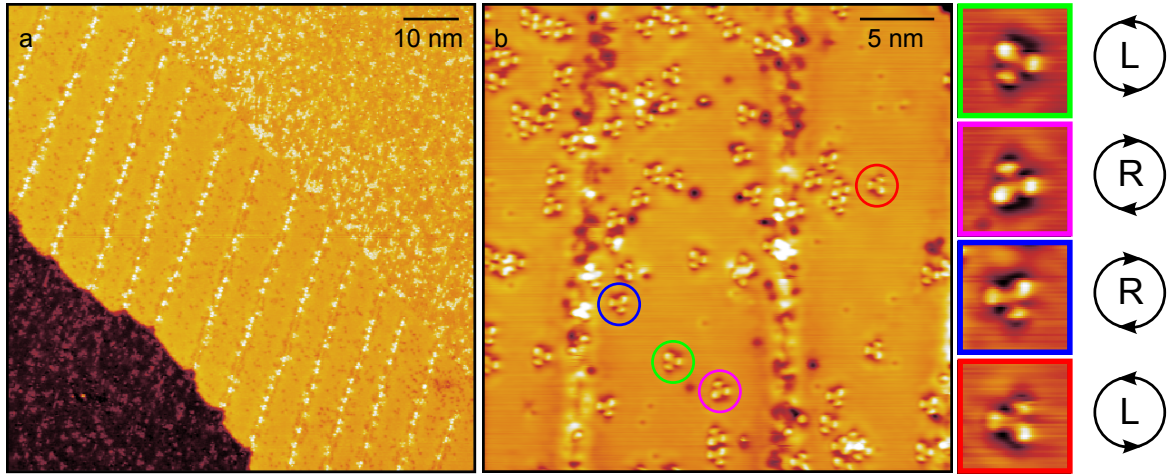


Figure 7.1: STM images of the adsorption of TPT on Fe/W(110). (a) TPT deposited with the substrate hold at room temperature. TPT sticks to the dislocation lines and step edges on the DL. STM image parameters: $80 \text{ nm} \times 80 \text{ nm}$, $V_{\text{Bias}} = 50 \text{ mV}$, $I_{\text{T}} = 1 \text{ nA}$, 78 K . (b) TPT deposited with the substrate cooled down to 170 K . Here TPT is less mobile and adsorbs between dislocation lines. Four different adsorption orientations were found (marked by green, magenta, blue and red circles). Zooms ($2.5 \text{ nm} \times 2.5 \text{ nm}$) of the color coded molecules and their respective sense of rotation are shown right of (b). STM image parameters: $30 \text{ nm} \times 30 \text{ nm}$, $V_{\text{Bias}} = -100 \text{ mV}$, $I_{\text{T}} = 1 \text{ nA}$, 5 K

sublimation temperature. When samples were warmed up, TPT was found attached to the dislocation lines again.

A close inspection of the adsorbed TPT reveals differences in brightness and shape of all three phenyl rings. These differences must stem from the interaction with the surface since in gas phase all phenyl rings are equal and exhibit the same electronic properties [151]. The electronic properties of an isolated gas phase TPT molecule near the Fermi level are shown in Fig. A.5 in the appendix. An explanation for this behavior will be given in the next section.

The central triazine ring appears considerably lower than the surrounding phenyl rings and is hardly distinguished. The observation of the triazine ring appearing lower was made for all bias voltages in the interval $[-1 \text{ V}, 1 \text{ V}]$. One reason for this behavior is certainly the higher electronegativity of nitrogen ($\chi_{\text{N}} = 3.04$ on the Pauling scale) compared to carbon ($\chi_{\text{C}} = 2.55$ on the Pauling scale). The higher electronegativity reduces the extent of the electronic states of the triazine rings into the vacuum and thus leads to a reduced LDOS at the tip position.

In general, previous studies on the electronic properties of aromatic rings with varying nitrogen content deposited on surfaces reported considerable differences in the respective DOS [59]. Furthermore, the symmetry of the HOMO changes from π - in benzene (C_6H_6) to σ -symmetry in pyridine ($\text{C}_5\text{N}_1\text{H}_5$) and pyrazine ($\text{C}_4\text{N}_2\text{H}_4$). DFT calculation by Rico Friedrich showed that the HOMO of an isolated TPT is of σ -symmetry located on the

triazine ring (Fig. A.5 in the appendix). The first occupied π -orbitals are delocalized over the whole molecule. However, the conclusions drawable from the electronic properties of a molecule in gas-phase compared to the same molecule adsorbed on a reactive surface seem very limited. To reveal the reason for the triazine rings lower appearance in STM images the electronic properties of all aromatic rings of TPT on DL Fe/W(110) are scrutinized in section 7.2.

The differences in ring brightness and shape give rise to four different, equally distributed adsorption orientations on the DL Fe/W(110). All four orientations are shown as color coded zooms next to (Fig. 7.1b). A closer investigation reveals that these four positions can not be transformed into each other by rotation, but only by mirroring about the $[001]$ or $[1\bar{1}0]$ direction.

The phenomenon that objects of identical composition are only transferrable into each other by mirroring is named chirality, the both mirror images are called enantiomers. If the sense of rotation is defined by going from the biggest and brightest phenyl ring to the smallest phenyl ring, the four positions split into two groups: left-rotating and right rotating. The sense of rotation for all adsorption orientations is indicated by the symbols next to the zoom images in Fig. 7.1. In the following the different enantiomers will be called "L-type" and "R-type". Both members of each group can be transformed into each other by rotation of 180° . The members of opposite groups can be only transformed into each other by mirroring.

The observation of a chiral geometry was initially surprising, because both TPT and Fe surface separately are non-chiral objects. However, both exhibit different rotation symmetries, *i.e.* 2-fold for the Fe-surface and 3-fold for TPT. The formation of a chiral molecule-surface hybrid arises apparently from the impossibility of finding an adsorption geometry which satisfies the symmetries of both systems with respect to each other. The formation of chiral molecule-surface hybrids has been observed before, *e.g.* CoPc on DL Fe/W(110) [139] and was reported to result in interesting effects regarding their electronic properties and self organization [152].

7.1.2 Adsorption position and geometry

The determination of the TPT adsorption position and geometry on an atomic level possibly reveals further information into the origin of the differences in ring shape and brightness and the formation of a chiral system. Furthermore the adsorption geometry is used as input for DFT calculations.

All attempts to achieve atomic resolution of the bare DL Fe/W(110) or TPT on DL Fe/W(110) in constant current mode (CCM) failed. However, atomic resolution for both cases was achieved by using very high tunneling currents in constant height mode (CHM). In CHM the tip is stabilized at a certain tip-sample separation given by V_{Bias} and I_T . Subsequently the tip-sample separation is reduced by Δz and the surface is scanned without feedback loop. Figure 7.2a shows a CHM image with atomic resolution of the bare DL Fe/W(110). The degree of distinctness in the atomic lattice depends strongly on the tip-sample distance and the resulting amount of tunneling current. The strong distinctness of the atomic lattice in Fig. 7.2a could be only achieved by very high tunneling currents of

up to - 245 nA. The measured lattice constants agree with the the expected values in [001] direction with $a_{\text{exp}} = 2.9 \pm 0.1 \text{ \AA}$ and $a_{\text{lit}} = 2.87 \text{ \AA}$.

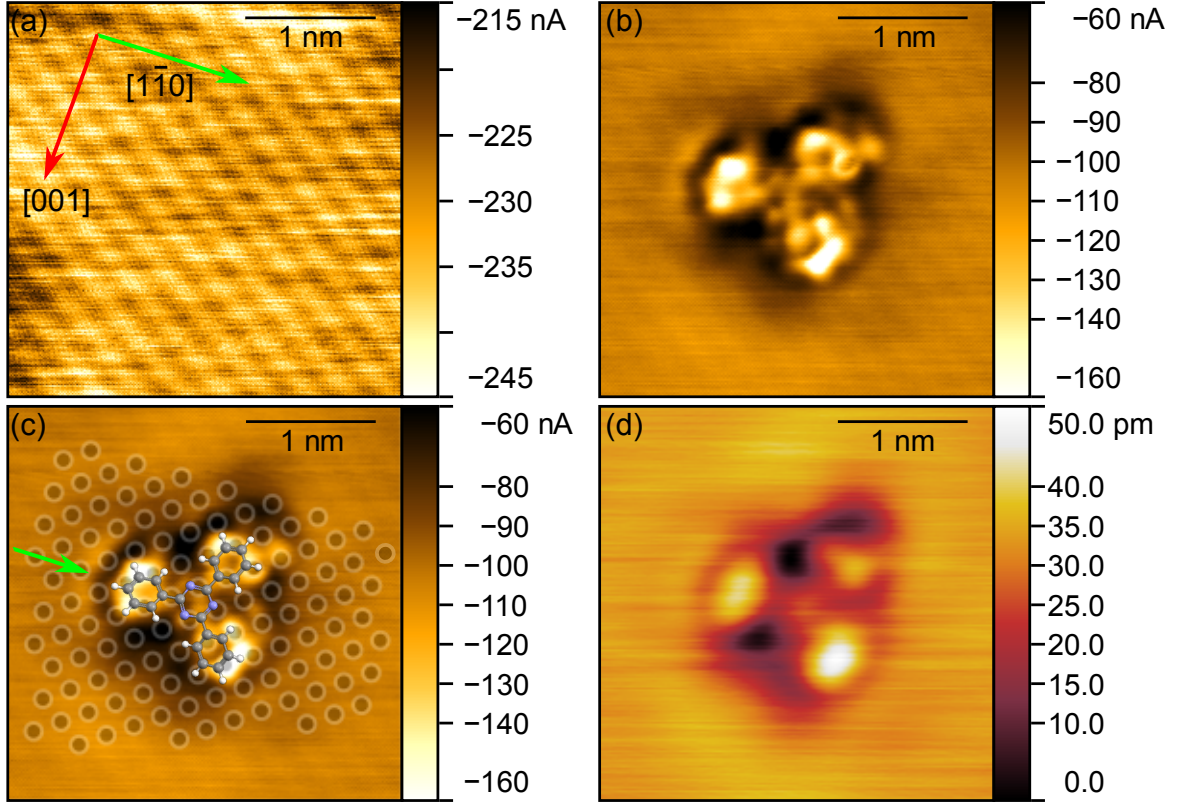


Figure 7.2: High resolution CHM (a-c) and CCM (d) STM images. a) Atomic resolution of a defect-free DL Fe area. STM image parameters: $3 \text{ nm} \times 3 \text{ nm}$, stabilized at $V_{\text{Bias}} = -100 \text{ mV}$, $I_{\text{T}} = 1 \text{ nA}$, then $\Delta z = -240 \text{ pm}$, 5 K . b) TPT on defect-free Fe DL. c) Same as b) but overlaid with appropriately scaled TPT in gas phase geometry and atomic Fe lattice, giving a reasonable approximation for the adsorption position and geometry on an atomic scale. STM image parameters: $3 \text{ nm} \times 3 \text{ nm}$, stabilized at $V_{\text{Bias}} = -100 \text{ mV}$, $I_{\text{T}} = 1 \text{ nA}$, then $\Delta z = -210 \text{ pm}$, 5 K . d) High resolution constant current image of the same molecule to allow comparisons between CHM and CCM images. STM image parameters: $3 \text{ nm} \times 3 \text{ nm}$, $V_{\text{Bias}} = -100 \text{ mV}$, $I_{\text{T}} = 1 \text{ nA}$, 5 K .

Figure 7.2b shows a high resolution CHM image of TPT with atomic resolution of the underlying Fe DL substrate. In order to avoid tip-sample interaction it was necessary to increase the tip-sample separation by 30 pm compared to Fig. 7.2a. Thus the level of distinctness for the atomic resolution is slightly weaker. The three phenyl rings of TPT are easily identified. In comparison to CCM topography images (Fig. 7.2d) the differences in shape and brightness of the phenyl rings are even stronger pronounced and a highly complicated internal structure is revealed. The central triazine ring appears again with lower intensity. The observation of the internal structure is attributed to the high tunneling

currents resulting from the by 2 Å lower tip-sample separation compared to typical CCM images.

Figure 7.2c shows the same image as Fig. 7.2b, but overlaid with a TPT molecule in gas phase geometry scaled to the appropriate size and an atomic lattice, revealing a complicated, highly non-symmetric adsorption geometry. While the two upper phenyl rings of the overlaid TPT agree reasonably well with the measured geometry, the lower ring seems slightly shifted. This shift indicates that TPT changes its geometry when adsorbed on DL Fe/W(110) compared to its gas phase geometry.

Furthermore Fig. 7.2c shows that each phenyl ring has a different binding geometry to the substrate. This offers an explanation for the different phenyl ring shapes and sizes. While the two bright rings seem to be in contact with only three Fe atoms, the small top ring is hybridized with four iron atoms. The stronger hybridization presumably reduces the decay length of these states into the vacuum and lead to different ring brightnesses in STM images. The three nitrogen atoms of the triazine ring appear to sit on top of Fe atoms. It seems that one mirror axis of the molecule lies along the $[1\bar{1}0]$ -direction of the substrate, indicated by the green arrow in Fig. 7.2c.

One should keep in mind that there is a small degree of freedom for positioning the iron lattice in Fig. 7.2c since the level of distinctness of the atomic resolution is not completely unambiguous. Nevertheless, this experimentally derived adsorption geometry allows to understand the differences in brightness for the phenyl rings and is considered as starting geometry for DFT simulations in the following section.

Fig. 7.2d shows a high resolution CCM image of the same molecule for comparison with the previous data and confirms this particular TPT molecule to be of L-type. Again, different phenyl ring shapes and brightnesses are clearly seen in this image. The molecule is surrounded by a dark halo with especially dark regions surrounding the left phenyl ring and above of the top phenyl ring. These dark areas could be a sign of charge transfer from the substrate to the molecule. The central triazine ring is easily identified in Fig. 7.2d. Quite surprisingly it appears even lower than the surrounding iron substrate, revealing a significantly smaller LDOS and than the surrounding phenyl rings.

7.1.3 Comparison with DFT

The TPT/Fe/W(110) system was modelled with DFT by Rico Friedrich, Vasile Caciuc and Nicolae Atodiresei from PGI-1. The goal of this study was to improve the understanding of the experimental data and to potentially hint to other interesting, previously undiscovered, properties. Since the electronic properties of TPT on DL Fe/W(110) depend on the position and geometry of the adsorbed molecule, the first step in this study was to determine both the geometry and position of the adsorbed TPT molecule. Both quantities are determined by putting TPT in its gas phase geometry in different starting positions on top of DL Fe/W(110) and allowing the molecular geometry to relax until the atomic forces are smaller than a predefined value. Since the adsorption of molecules on surfaces has been repeatedly studied by DFT [49, 59, 16, 92], reasonable starting positions can be guessed.

The starting positions were chosen to retain the highest possible symmetry which proved to be a good strategy in the past [151]. These were named (Table 7.1) after the

position of the nitrogen atoms of the central triazine ring in regard to the iron lattice. Besides these purely theoretic starting positions, a non-symmetric position derived from experiment (Fig. 7.2c) was also considered. After TPT was positioned on top of the substrate all respective structures were allowed to relax until the atomic forces were smaller than 10 meV/Å. Chemical and long-range vdW interactions were considered in this DFT simulation.

Subsequently, the adsorption energy of the relaxed positions, listed in table 7.1, was calculated. The highest value was obtained for the experimental derived starting geometry with 3.9 eV. This result highlights the benefits of experimental inputs to DFT. Especially in cases with low symmetry it is more difficult to guess good starting positions. The energy difference to the geometry with the next highest adsorption energy (80 meV) is significant. It is interesting to note, that all considered starting positions lead to different adsorption energies. This observation shows that the adsorption energy exhibits many local minima in dependence on the adsorption geometry.

The adsorption of benzene on DL Fe/W(110) has been previously studied by DFT [16]. Benzene adsorbs on a hollow site with an adsorption energy of 978 meV. TPT exhibits three benzene-like phenyl rings and one triazine ring and exhibits a nearly exactly four times higher adsorption energy (3.9 eV), which appears reasonable. The influence of replacing carbon with nitrogen in organic compounds on the adsorption energy has also been investigated. However, no clear trend was found, since both increasing [92] and decreasing adsorption energies [59] have been reported.

geometry	symmetry	adsorption energy (eV)
experimental	non-symmetric	3.9
N on bridge 90°	high-symmetric	3.82
N on top	high-symmetric	3.63
N shifted 90°	high-symmetric	3.55
N on bridge	high-symmetric	3.19

Table 7.1: Adsorption energies of different adsorption positions and geometries calculated by DFT. The experimental found geometry exhibits the highest adsorption energy. The DFT geometries will be published in the PhD thesis of Rico Friedrich.

The calculated DFT adsorption position and geometry is shown in Fig. 7.3a. It is very similar (although not identic) to the experimental geometry in Fig. 7.2c. The minor differences can be attributed to the small degree of freedom in placing the atomic lattice in Fig. 7.2c. The phenyl rings of TPT are found to occupy hollow-like sites, similar to benzene on DL Fe/W(110) [16]. However, the exact benzene-like configuration can not be realized, because the more complicated geometry of TPT does not allow this position. Consequently, each phenyl ring occupies a slightly different position. The triazine ring occupies a hollow site too with the nitrogen atoms on top of iron atoms.

In addition to the determination of adsorption geometries, DFT allows to calculate the electronic properties of such systems. A simulated STM topography image at V_{Bias}

$= -100$ mV for the geometry in Fig. 7.3a is shown in Fig. 7.3b. The agreement to an experimental image in Fig. 7.3c is good. The different appearance and size of the TPT rings is nicely reproduced. The lower intensity of the triazine ring observed in experiments is not reproduced by DFT. Overall this comparison shows that DFT simulations and STM experiments are in a good qualitative agreement.

Finding the same adsorption position and geometry in experiment and theory confirms the validity of comparisons between STM and DFT. This result thus lays the foundation for comparisons between STM and DFT in the following sections, promising a better understanding of the experiment through theory.

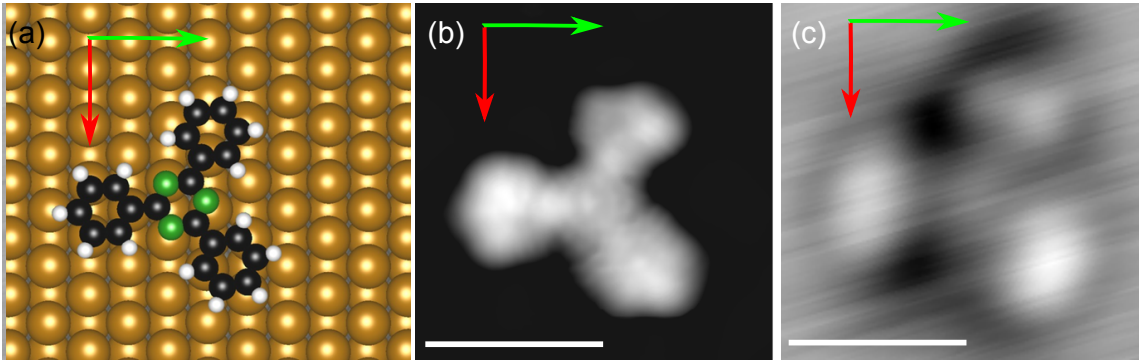


Figure 7.3: a) Adsorption position and geometry of TPT/Fe/W(110) with the highest adsorption energy determined by DFT calculations. b) Simulated STM topography image of the geometry shown in a) at $V_{\text{Bias}} = -100$ mV. c) Experimental STM topography image of TPT in the same orientation (L-type) as a). STM image parameters: $2 \text{ nm} \times 2 \text{ nm}$, $V_{\text{Bias}} = -100$ mV, $I_{\text{T}} = 1 \text{ nA}$, 5 K . The green (red) arrow indicates the $[\bar{1}\bar{1}0]$ ($[001]$) direction. White bars in b) and c) represent 1 nm .

7.2 Electronic properties of TPT/Fe/W(110)

Studying the electronic properties of TPT on Fe/W(110) reveals additional information about the adsorption characteristics and hybridization processes. As described in the previous section four different adsorption orientations have been found. Thus, the first section in this chapter investigates whether all orientations have the same electronic properties.

STS measurements are the result of a convolution of tip and sample DOS (Eq. 2.8 in section 2.3). In reality STM tips usually exhibit a non-constant DOS which will lead to contributions in the tunnel spectra. In order to reliably determine the electronic properties of an unknown sample, the influence of tip states needs to be established. Afterwards the LDOS of all aromatic rings is studied by STS in section 7.2.2.

Another possibility of investigating the electronic properties are energy-integrated topography images and energy-resolved dI/dV -maps. Images with varying bias voltages probe different energy intervals and help visualizing the spatial distribution of the LDOS. Topog-

raphy images and dI/dV -maps are compared with images obtained from DFT calculations and discussed in section 7.2.3.

7.2.1 Influence of adsorption orientation

This section investigates whether all four adsorption orientations have the same electronic properties. Spectra of TPT were always taken in small scale topography images similar to Fig. 7.4a in order to select specific TPT rings with high spatial resolution. Reference spectra of the DL Fe/W(110) were taken before and after measuring TPT to monitor tip changes during the experiment.

As seen in section 6.2 two peaks at +700 mV and at -80 mV are characteristic for STS measurements of DL Fe/W(110) [103, 107, 138, 139]. Depending on the tip DOS peaks at other energies can occur, which are named "tip states" in the following. If STS measurements show considerable tip states, one can try to change the tip's geometry or its elemental composition by pulsing the bias voltage or crashing the tip gently into the substrate. However, achieving a tip with constant DOS by these methods has proven to be almost impossible in the experiment. Thus, one usually has to compromise by using a tip which affects the measurement as little as possible, by *e.g.* having tip states at energies which are of less importance for the experiment.

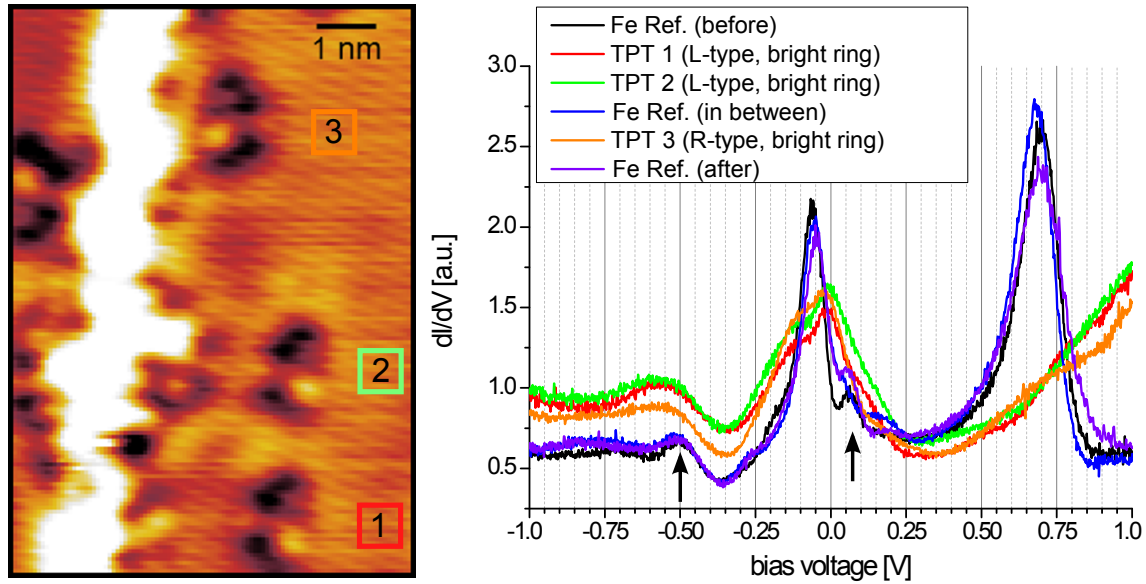


Figure 7.4: a) STM topography image of TPT on the DL Fe/W(110) showing the three TPT molecules investigated by STS. The color scale was chosen for best contrast of the TPT molecules. Thus, the dislocation line appears white. STM image parameters: $V_{\text{Bias}} = -100$ mV, $I_T = 1$ nA, 5 K. b) STS of TPT and Fe reference. Fe reference spectra were taken before, in-between and after the measurements of TPT. The spectra for TPT were taken above the bright lobe. STS parameters: $V_{\text{Stab}} = -100$ mV, $I_{\text{Stab}} = 1$ nA.

Fig. 7.4a shows a typical small scale image used for acquiring STS data with three TPT

molecules adsorbed on defect-free DL Fe/W(110). The bright lobe of the TPT molecules (TPT 1 and TPT 2) at the bottom and in the middle of Fig 7.4a is easily identified in the bottom right corner of the molecules. The darkest lobe, although hardly visible in Fig 7.4a is located at the top right corner. Thus, according to the definition in Fig 7.1 they are left-rotating ("L-type"). The sense of rotation of the uppermost TPT molecule (TPT 3) is of R-type. STS spectra were taken on each molecule always on the brightest lobe. DL Fe/W(110) reference spectra were taken before, in-between and after the TPT spectra to ensure that no significant tip changes occurred during the measurements.

The respective STS measurements are shown in Fig. 7.4b. The DL Fe/W(110) reference spectra (black, blue and purple lines in Fig. 7.4b) agree to previous reports [103, 107, 138, 139]. Small tip states at 100 meV and in the interval [-600 meV, -300 meV] are detected (indicated by black arrows in Fig. 7.4b). Since the main iron peaks are well reproduced the tip seems suitable for STS measurements. The reference spectra are basically unchanged in most parts of the investigated energy interval with minor changes only occurring at 100 meV. Therefore the TPT spectra recorded in-between are considered to be comparable.

The spectra of the different mirror images (red (L-type), green (L-type) and ocher (R-type) lines in Fig. 7.4b) are very similar and are assumed identical within the accuracy of the experiment. The electronic properties of all other rings were studied in the same manner and similarly, no differences were observed.

This experiment proves that all four adsorption orientations originate from one adsorption position along with its respective geometry. Furthermore, it confirms the expected behaviour concerning the electronic properties of enantiomers. As chirality in chemical systems is defined as a broken symmetry, different properties in enantiomers arise only when probed with symmetry breaking operations [153]. Since spin-integrated STS is not a symmetry breaking operation, the measurement thus confirms the expected behavior. Differences might however arise in SP-STM. This issue will be scrutinized in section 7.3.3.

7.2.2 Site dependent LDOS of TPT

In this section the LDOS of all individual rings of TPT are investigated and compared. The electronic properties give additional information about the hybridization mechanisms of TPT with the DL Fe/W(110) substrate.

Before a meaningful discussion of the electronic properties is possible, one of the main challenges in STS, the separation of tip and sample DOS, needs to be addressed. The tip DOS is affected by the apex geometry and chemical composition. Unfortunately, both aspects can not be reliably controlled. Since tips often change during experiment it is difficult to directly compare STS measurements. Thus, the only way of obtaining meaningful results is to monitor tip changes by regularly comparing with reference spectra reported in literature.

STS measurements on TPT on DL Fe/W(110) with different tips revealed that the spectra depend considerably more on tip states than the iron reference spectra. This behavior is illustrated in Fig. 7.5. All TPT rings were investigated by STS and reference spectra were taken before, in-between and afterwards. Fig. 7.5 shows measurements from two consecutive days with the same tip. The reference spectra however reveal differences

which must result from different tip DOS. Additionally, such comparisons strongly depend on the measurement parameters. All measurements in Fig. 7.5 have been stabilized at -100 mV and 1 nA. Thus no differences are expected at this energy.

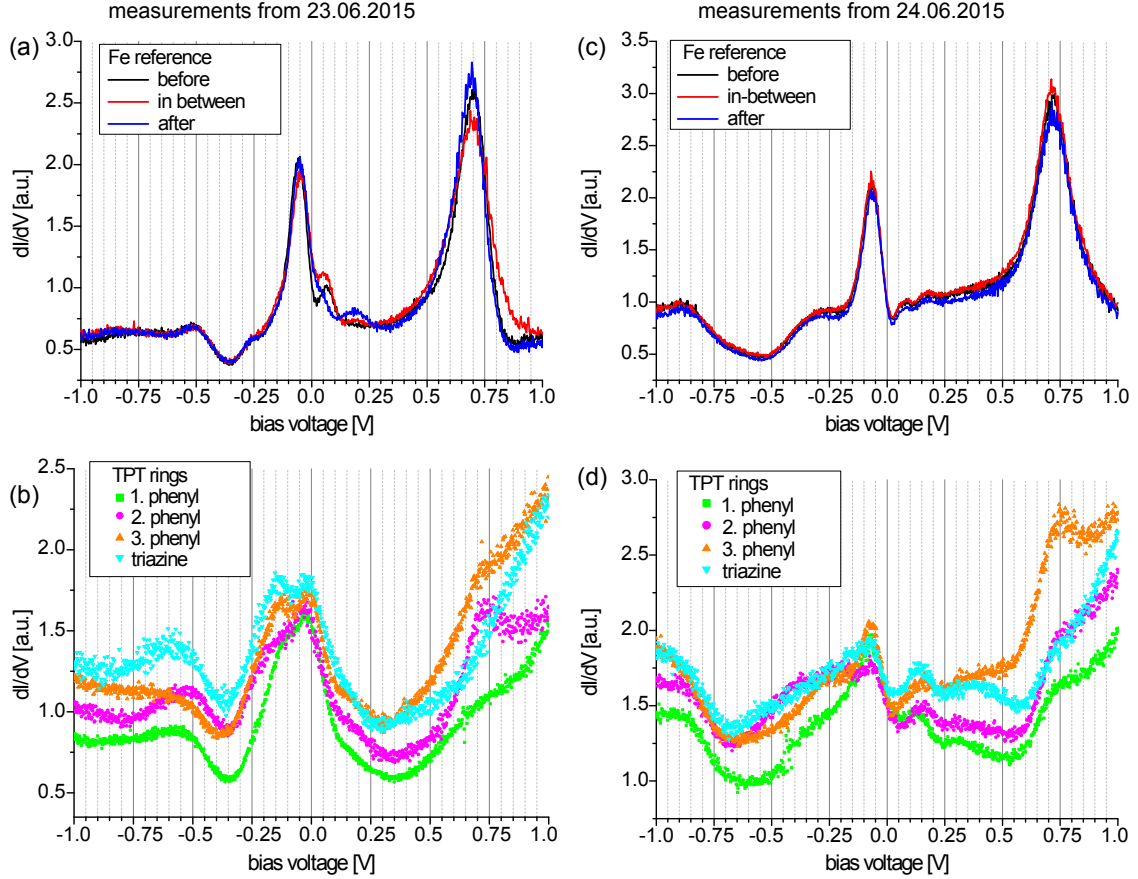


Figure 7.5: Comparing STS measurements with different tip conditions in order to estimate the influence of tip states in TPT spectra. a) [b)] shows Fe reference spectra before, in-between and after the TPT ring measurements in c) [d)]. The STS measurements of the aromatic rings of TPT in c) and d) show some similarities but also differences although the reference spectra are close to literature. The phenyl rings were numbered after their brightness: 1 - bright, 2 - intermediate, 3 - dark. STS parameters: $V_{\text{Stab}} = -100$ mV, $I_{\text{Stab}} = 1$ nA.

Fig. 7.5a shows the same DL Fe/W(110) reference spectra as Fig. 7.4b. A reasonable agreement with literature [103, 107, 138, 139] was already established in the last section. Tip states were identified at 100 meV and in the interval [-600 meV, -300 meV]. During spectroscopy measurements only minor changes are observed confirming the comparability of the measurements in-between.

Fig. 7.5b shows spectra taken above each respective TPT aromatic ring. Generally only broad electronic features are observed. Since no molecular-like states are present, a strong

chemisorption is deduced. Furthermore, the electronic properties of all rings are rather similar with small differences. This behaviour is interesting from two perspectives.

First, only a small difference, where one would expect a significant difference, between the phenyl rings and triazine ring is observed. DFT calculations on a gas phase TPT (Fig. A.5 in the appendix) revealed that the HOMO is strongly localized on the triazine ring. The adsorption on the surface leads to strongly broadened hybrid states delocalized over the whole molecule.

Second, all phenyl rings, which exhibit the same electronic properties in gas phase show a different DOS when adsorbed on DL Fe/W(110). While this observation was already made in the previous sections, Fig. 7.5b reveals that these differences are not limited to certain energies or energy intervals, but affect the whole DOS near the Fermi level. Consequently, the TPT on DL Fe/W(110) system highlights the importance of the adsorption geometry on the electronic properties of molecule-surface hybrids.

Comparing the TPT spectra to the DL Fe/W(110) reference spectra reveals that the TPT rings show peaks or shoulders at the iron peak energies, which again showcases the strong hybridization between molecule and substrate. The interval from -250 mV to -1000 mV is similar in both iron and TPT spectra and indicates that this interval is dominated by the tip DOS. The prevalence of tip states when probing occupied sample states is well known and has been discussed in section 2.4.

A comparison of each individual TPT ring with the iron reference and the projected DOS (PDOS) for states with π -symmetry calculated by DFT is shown in Fig. A.6 in the appendix. DFT reveals even stronger differences for the individual rings. However, a direct comparison between the LDOS measured by STM and the PDOS calculated by DFT is generally difficult. Nevertheless, all peak positions identified in the STS experiments were also found by DFT.

The measurements in Fig. 7.5a,b were repeated on the following day with the same tip. The DL Fe/W(110) reference spectra in Fig. 7.5c are similar to the ones from the previous day (Fig. 7.5a) and show both d_{z^2} -like states (refer to section 6.2). However, minor differences in the spectra showcase the influence of tip states in STS experiments. While the general shape of the spectra is rather similar, many minor differences can be found, *e.g.* in the intervals [-1000 meV,-250 meV], [0 meV,200 meV] and around 900 meV.

After the suitability of the tip for STS was established, spectra of each TPT ring were recorded. The TPT spectra are again very broad and have peaks or shoulders at the iron peak positions. However, besides the qualitative agreement, the spectra in Fig. 7.5b and d are rather different. This observation shows that in comparison to the DL Fe/W(110), the TPT spectra are considerably stronger affected by tip states.

While the TPT spectra seem highly dependent on the tip DOS and thus appear not very reproducible, quantitative differences between the aromatic rings are reproduced between Fig. 7.5b and Fig. 7.5d by the sequence of the respective colors (*i.e.* the dI/dV signal for the brightest phenyl ring is always lowest, triazine is highest for unoccupied states).

In conclusion, the absence of narrow molecular orbitals reveals a strong hybridization of TPT with the substrate. Thus one requirement for the formation of hybrid-molecular magnets could be established by this section. The strong hybridization could possibly also explain why a non-constant tip DOS might be more prevalent in broad TPT spectra than

in iron spectra with sharper features. The different electronic properties of each individual TPT ring are a result of the non-symmetric adsorption geometry and could give rise to interesting magnetic properties of the hybrid-molecular magnet.

7.2.3 Topography images and dI/dV maps

Another way of investigating the electronic properties of samples are energy-integrated topography images and energy-resolved dI/dV-maps. The first row of Fig. 7.6 shows topography images of TPT on DL Fe/W(110) at different bias voltages. As can be seen from Fig. 7.6a-d TPT itself shows only a small dependence on the bias voltage. However, the contrast in comparison to the DL Fe/W(110) substrate is subject to significant changes. The clearest change in TPT appearance is observed when switching between positive and negative bias voltages. For all investigated bias voltages, except -100 mV, a bright halo surrounds the molecule. At -100 mV pronounced depressions are observed on the iron substrate directly neighboring the TPT molecule, indicating possibly a charge depletion zone on the substrate directly next to the molecule.

The second row of Fig. 7.6 shows DFT images for comparison with the topography images. The DFT images show considerably more details and differences depending on the bias voltage are stronger pronounced. Since STM measures a slightly smeared out LDOS it is generally difficult to reproduce highly detailed DFT images. The general TPT shape is always reproduced, confirming that DFT is able to reasonably simulate the TPT on DL Fe/W(110) system. However, DFT is not able to reproduce the strong influence of TPT on the surrounding substrate seen in Fig. 7.6a-d. Thus DFT can not offer more insight on the origin of these phenomena.

The dI/dV-maps in the third row reveal considerable spatial changes of the energy resolved DOS depending on the bias voltages. Fig. 7.6i was taken at an energy related to one of the d_{z^2} -like peaks of the iron substrate. Thus the substrate is characterized by a high LDOS, while the molecules appear as negative images without any detail. In Fig. 7.6j, the shape of TPT is resolved, but appears again as a negative image. Interestingly substrate areas not directly bond to TPT show significant changes in conductivity too.

This situation is even stronger pronounced in Fig. 7.6k. In contrast to the previous images TPT is brighter than the substrate. The conductivity of the substrate is considerably affected by the adsorption of TPT, even at a distance of up to 1 nm. Generally, the conductivity of the substrate is increased left and right of TPT, while above and below the conductivity is decreased. Thus this image especially showcases that the adsorption affects the electronic properties of both molecule and substrate. In Fig. 7.6l TPT can not be distinguished from the substrate. In the previous section it was found that the occupied sample states are largely affected by tip states, thus possibly explaining this behavior.

The dI/dV-maps in the third row of Fig. 7.6 reflect the same information as the spectra shown in Fig. 7.5. However, these images directly show the spatial distribution of the conductivity and allow immediate comparisons of individual aromatic rings or to the clean substrate. The significant influence of TPT on the surrounding substrate was revealed by these maps.

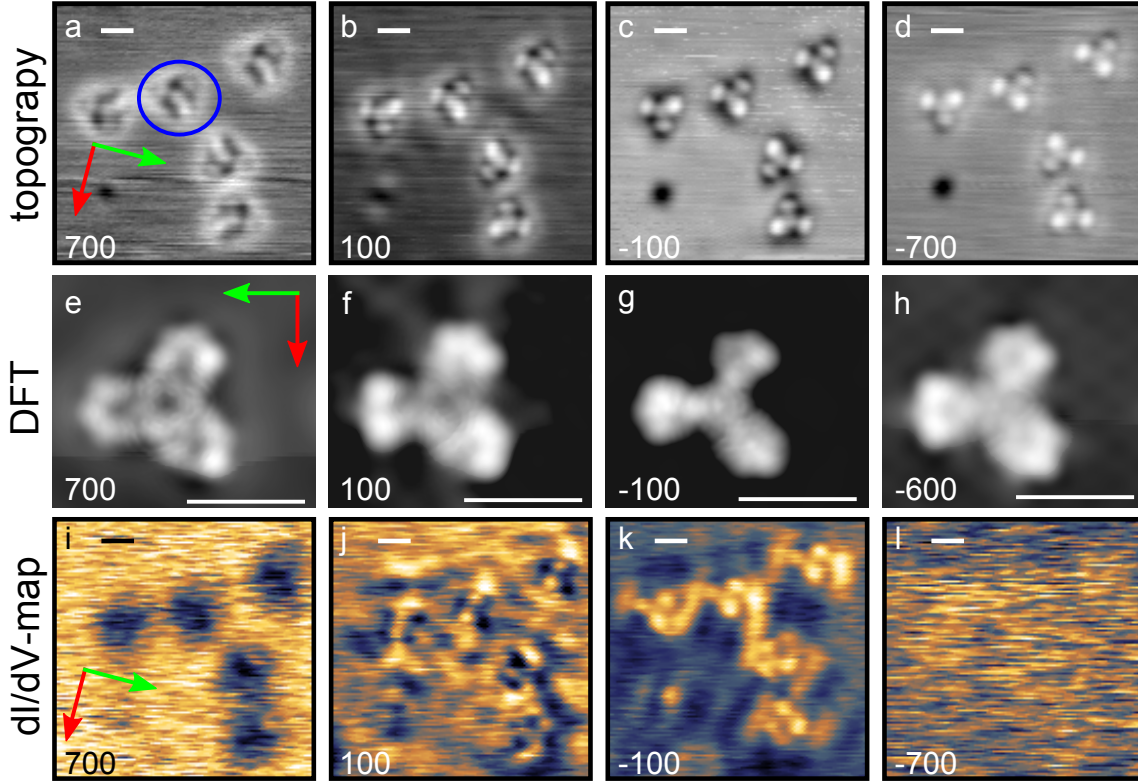


Figure 7.6: Comparison of (spin-integrated) STM topography images (first row) with simulated topography STM images from DFT (second row). The third row shows the simultaneously recorded dI/dV maps. STM image parameters: $7.8 \text{ nm} \times 7.8 \text{ nm}$, V_{Bias} is given in the respective image, $I_T = 1 \text{ nA}$, 5 K . Black and white bars equal 1 nm . The red arrow indicates the $[001]$ and the green arrow the $[110]$ direction. The blue circle in a) marks a TPT molecule with the same orientation as shown in the DFT images.

7.3 TPT on Fe/W(110) imaged by SP-STM

Spin polarized STM (SP-STM) allows to study the structural, electronic and magnetic properties of nanoscopic objects with sub-nanometer spatial resolution. Thus it is ideal for investigating the spin dependent hybridization of TPT on DL Fe/W(110). The operation of SP-STM with Cr-coated tips was successfully established in chapter 6 by the characterization of the Fe/W(110) system. All images in this section were obtained with Cr-coated tips with a strong OOP magnetization.

The SP-STM investigation starts with qualitatively comparing the TPT appearance on opposite magnetic domains of DL Fe/W(110) substrate. A clear difference in TPT appearance both in topography images and dI/dV -maps is found and confirms a spin-dependent hybridization. The orientations of hybrid-molecular magnets on opposite domains could be determined by reversing the tip magnetization by pulsing the bias voltage. This knowledge eventually allows a more quantitative investigation of the hybrid-molecular

magnet. Potential interactions arising from the chirality of the hybrid-molecular magnets with the magnetic properties of the DL Fe/W(110) substrate are investigated in 7.3.3.

7.3.1 Spin dependent hybridization

In spin-integrated STM images TPT looks the same regardless of the orientation of the magnetic domain it is adsorbed on. In contrast the appearance of TPT on opposite OOP magnetic domains of DL Fe/W(110) is considerably different when imaged by SP-STM. Thus a spin dependent hybridization is revealed.

Fig. 7.7 shows topography images (a and e) and dI/dV-maps (b-d and f-h) at two bias voltages obtained with a Cr-coated tip. All images were taken at same position and show two opposite magnetic domains of DL Fe/W(110). Depending on which domain TPT is adsorbed, it appears clearly different, both in topography images and dI/dV-maps.

The TPT appearance in the topography images on the "dark" domain is similar to that of previous spin-integrated images. In contrast, TPT on the "bright" domain is hardly identified and appears as mostly dark spot with one brighter lobe. Similar to the spin-integrated topography images in Fig. 7.6, changing the sign of the bias voltage leads to additional changes in TPT appearance. Most notably the bright halo around TPT in Fig. 7.7e is not observed in Fig. 7.7a. Both molecules marked by the black circles in Fig. 7.7a are shown Fig. 7.10 for different bias voltages. In the area of the domain wall (green circle in Fig. 7.7a), a gradual transition between TPT appearances is observed.

Different appearances of molecules on opposite magnetic domains have been observed in [16] for H₂Pc on DL Fe/W(110) (Fig. 3.9) or on CoPc on Co/Ir(111) [66] as already discussed in section 3.2.2. In both studies the integrated spin polarization of the hybrid-molecular magnet was visualized by subtracting the "bright" image (*i.e.* tip and sample magnetization are parallel) from the "dark" image (*i.e.* tip and sample magnetization are antiparallel). These difference images are ideal for visualizing the spatial variation of the energy-integrated spin polarization of the hybrid-molecular magnet. Applying this method to TPT would be very rewarding, since the non-symmetric adsorption position promises a highly site dependent spin polarization. The necessary prerequisites for obtaining difference images are discussed in the following section.

The dI/dV-maps (Fig. 7.7b and f show a similar behavior than already seen in the topography images. However the differences between TPT on opposite domains are even stronger pronounced, showing that the spin dependent hybridization is highly energy dependent. To scrutinize these observations color coded zooms of the dI/dV-maps are shown in Fig. 7.7c and d and Fig. 7.7g and h respectively¹. When comparing the zooms in Fig. 7.7c and g to the respective spin-integrated dI/dV-maps in Fig. 7.6 a good agreement between both is found, similar to the SP-STM topography images. The dI/dV-maps additionally reveal spin dependent changes in the electronic properties of the substrate induced by the adsorption of TPT. The oscillating variation of the substrate DOS close to TPT in Fig. 7.7g and h especially emphasize this effect.

¹It should be noted that that the molecules in Fig. 7.7c and d (and g and h respectively) do not have the same orientation.

In conclusion, SP-STM images show a clear spin-dependent hybridization of TPT on DL Fe/W(110). The comparison between spin-resolved and spin-integrated STM images suggests that the appearance of TPT in spin-integrated STM is mostly dominated by one spin species. Due to the lack of magnetic fields in the LT-STM, an experimental determination of which spin species is dominant is not possible.

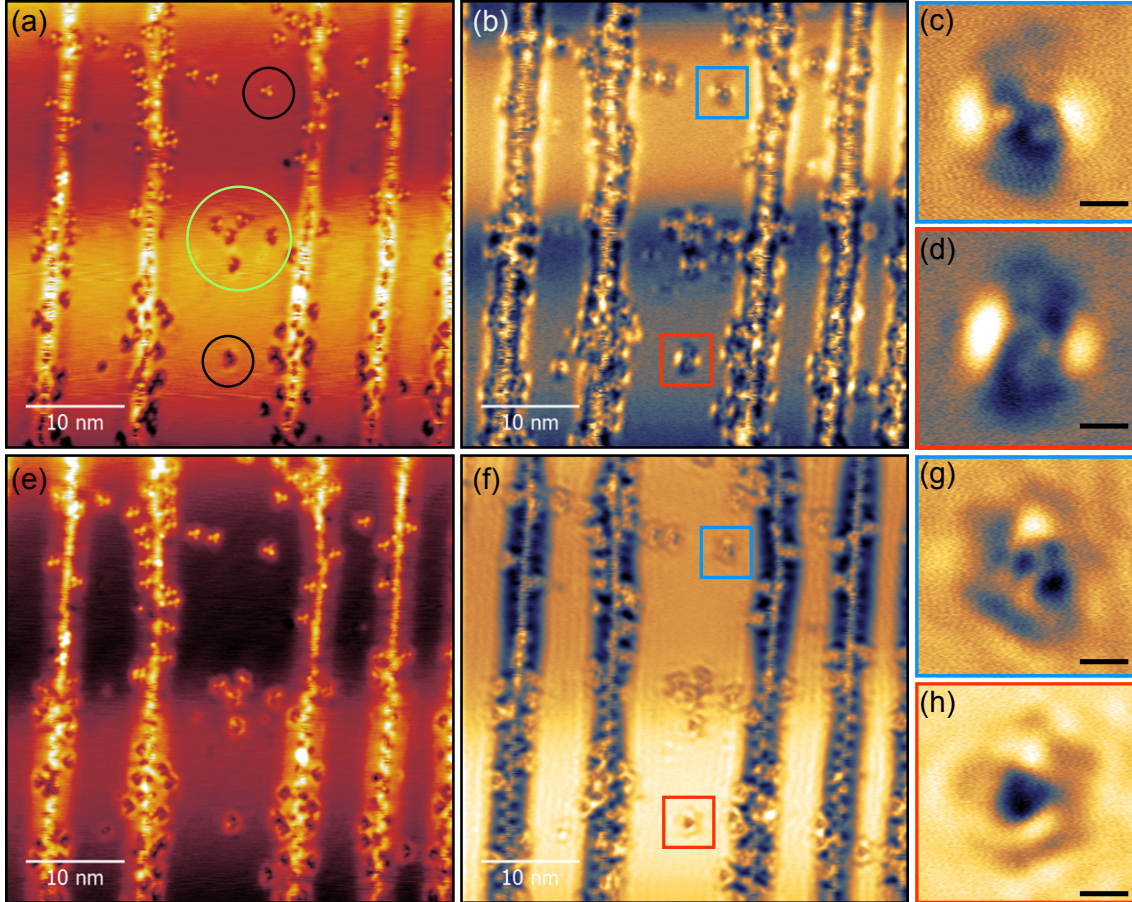


Figure 7.7: SP-STM images of TPT on opposite DL Fe/W(110) domains. (a) topography image and (b) simultaneously recorded dI/dV-map of TPT on two opposite DL Fe/W(110) domains ($45 \text{ nm} \times 45 \text{ nm}$) (c) and (d) show color coded dI/dV-map zooms of the TPT molecules in (b) ($4.6 \text{ nm} \times 4.6 \text{ nm}$). (e) topography image and (f) simultaneously recorded dI/dV-map of the same area as (a) with different V_{Bias} ($45 \text{ nm} \times 45 \text{ nm}$). (g) and (h) show color coded dI/dV-map zooms of the TPT molecules in (f) ($4.6 \text{ nm} \times 4.6 \text{ nm}$). Black bars in the dI/dV-map zooms equal 1 nm. STM image parameters: (a)-(d) $V_{\text{Bias}} = -100 \text{ mV}$, $I_T = 1 \text{ nA}$, (e)-(f) $V_{\text{Bias}} = 100 \text{ mV}$, $I_T = 1 \text{ nA}$.

7.3.2 Adsorption orientation of TPT in SP-STM

For obtaining difference images ideally only one hybrid-molecular magnet is studied and its magnetization direction is switched by applying an external magnetic field [16]. This method avoids possible electronic differences due to different adsorption positions or orientations and ensures that both images are directly comparable.

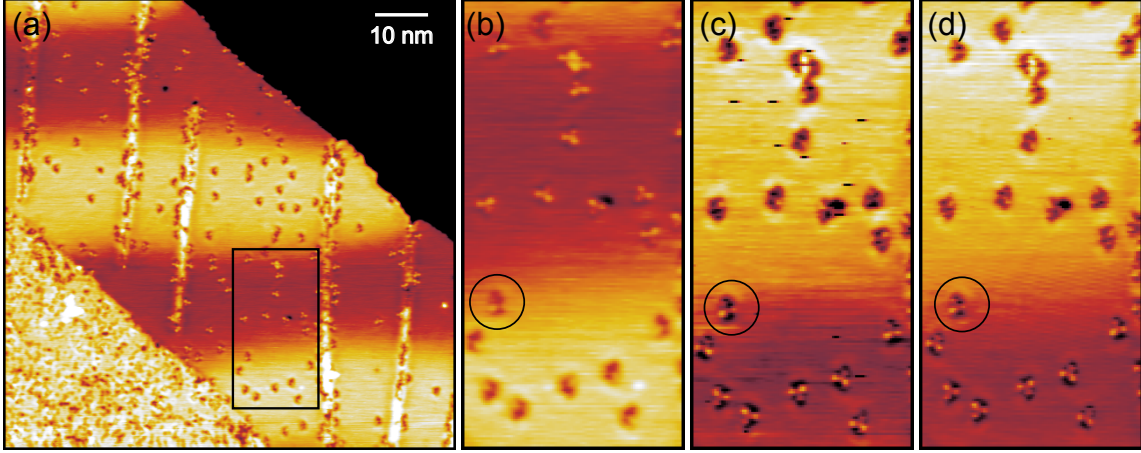


Figure 7.8: SP-STM images of TPT/Fe/W(110). (a) Overview image showing multiple OOP domains. TPT looks considerably different on opposite domains. Image parameters: 80 nm \times 80 nm, $V_{\text{Bias}} = -100$ mV, $I_T = 1$ nA, 5 K. (b) zoom of (a), highlighting the differences in appearance of TPT on opposite domains. 15 nm \times 30 nm. (c) shows the same area as (b), but with reversed magnetization due to a tip change. The appearance of TPT is also reversed, clarifying the adsorption orientation. Image parameters: 15 nm \times 30 nm, $V_{\text{Bias}} = -100$ mV, $I_T = 1$ nA, 5 K. (d) Same position as (b) and (c), but with higher tunneling current. Image parameters: 15 nm \times 30 nm, $V_{\text{Bias}} = -100$ mV, $I_T = 5$ nA, 5 K. The black circle in (b)-(d) marks a TPT adsorbed on a domain wall.

Unfortunately, the LT-STM from Omicron used for this investigation is not capable of applying external magnetic fields. Thus, to determine the spin polarization of TPT on DL Fe/W(110), more experimental work needs to be done. Since TPT appears very different in the images at these particular bias voltages shown in Fig. 7.7, it is not clear how these adsorption orientations relate to each other. One easy method would be to find a bias voltage where no spin polarization is observed and compare the adsorption orientations. However, all images within the bias voltage interval $[-1 \text{ V}, 1 \text{ V}]$ were not suitable for an unambiguous determination.

Thus, another method was required. Fig. 7.8a shows an overview STM image with several magnetic domains, where the different TPT appearance is clearly observed. Fig. 7.8b shows the area of (a) marked by the black rectangle, where the TPT appearance on opposite domains is difficult to relate to each other. By applying gentle voltage pulses to the tip, a tip magnetization reversal could be induced (Fig. 7.8c). Additionally the general imaging properties of the tip were not significantly altered, which allowed to identify corresponding

adsorption orientations: The bright lobe of TPT on the "dark" domain relates to the only lobe observed for TPT on the "bright" domain. The TPT molecule indicated by the black circle in Fig. 7.8b and c is adsorbed on a domain wall and does not significantly change its appearance after tip magnetization reversal, as expected.

Another open question concerns the origin of these differences in appearance. The height difference of neighboring domains in SP-STM of up to 25 pm at $V_{\text{Bias}} = -100$ mV (Fig. 6.8a) could possibly contribute to the different TPT appearance. Consequently the tunneling current was increased from 1 nA to 5 nA in Fig. 7.8d. This increase should reduce the tip-sample separation by roughly 30 pm. Since Fig. 7.8c and d look virtually similar, a significant contribution from the height differences of opposite magnetic domains in SP-STM to the different TPT appearance can be ruled out.

The determination of the orientation of TPT on opposite magnetic domains allows to directly compare SP-STM images. Thus the creation of difference images for visualizing the spatial variation of the spin polarization is possible. Difference images for multiple bias voltages will be analyzed in section 7.4.

7.3.3 Possible interaction of chirality and magnetism

Chirality in chemical systems represents a broken symmetry which can be probed in combination with another symmetry breaking operation. Obvious means for probing the different interactions of mirror-like enantiomers are polarized light, magnetic fields or spin polarized electrons [153]. Recent experiments on electron scattering through molecular films have shown that chiral molecules can be efficient sources of polarized electrons even in the absence of heavy nuclei as source of strong spin-orbit interaction [154, 155].

At the end of this dissertation, our theoretical colleagues raised the question if one observes a difference for L- and R-type enantiomers of the hybrid-molecular magnet on the same magnetic domain. Since the DFT calculations considered only chemical and vdW interactions and no relativistic corrections, no different electronic properties for the enantiomers could be found in the DFT model system.

SP-STM uses spin polarized electrons to probe the surface. Thus if a difference arises SP-STM should be in principle able to detect it. However, SP-STM images like Fig. 7.8 do not show obvious differences. To scrutinize this issue line profiles of different enantiomers were taken and compared in Fig. 7.9. Fig. 7.9b reveals differences of up to a few picometer. Since such height differences are of the order of the accuracy of the experiment itself, it is not possible to draw an unambiguous conclusion. Considering that the spin-orbit coupling, the origin of the potential variations, in carbon and nitrogen is very small, the differences might be very subtle or not even detectable by SP-STM. With a significant better statistics of the measurements shown in Fig. 7.9 one might be able to estimate if chirality dependent effects on a height scale of a few picometer are present or not.

Another possibility for observing a different interaction between the enantiomers and the magnetic substrate could arise from slightly different respective adsorption energies. An indication for such an effect might be an unbalanced distribution of R- and L-enantiomers on opposite domains. In Fig. 7.8 one counts on both bright domains 11 L-enantiomers and 14 R-enantiomers. On both dark domains one counts 12 L-enantiomers and 11 R-enantiomers.

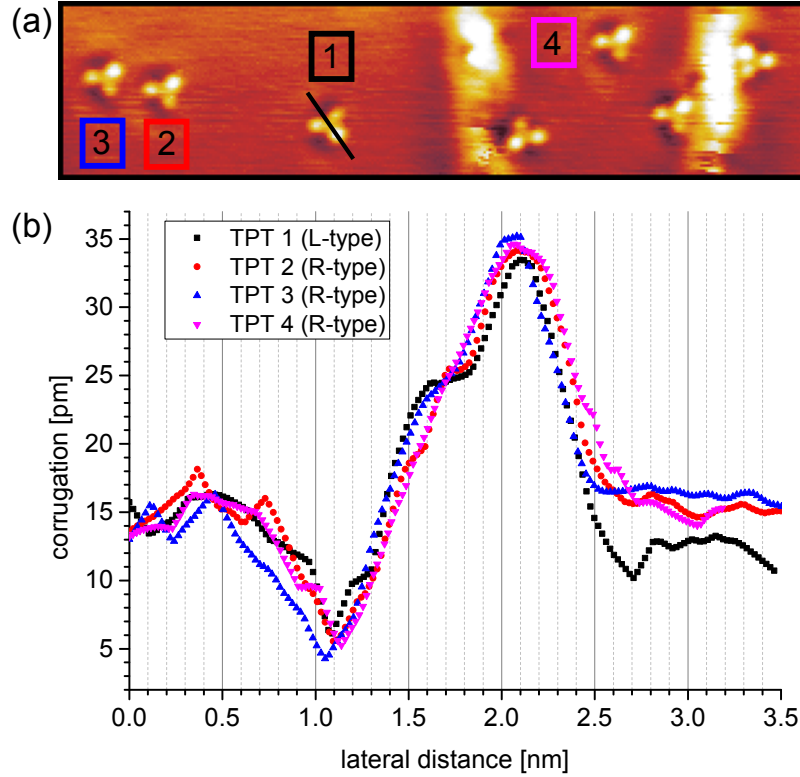


Figure 7.9: a) SP-STM image showing both R- and L-enantiomers on one magnetic domain. This figure is a zoom of the upper, "dark" domain of Fig. 7.8a. Image parameters: $15 \text{ nm} \times 30 \text{ nm}$, $V_{\text{Bias}} = -100 \text{ mV}$, $I_T = 5 \text{ nA}$, 5 K . b) Color coded line profiles of four TPT molecules. The black line on TPT 1 indicates where the respective line profiles were taken.

Unfortunately, not enough data is available to considerably improve the statistics.

Since without an external magnetic field it is not possible to determine the actual domain orientation, only SP-STM images taken with the same tip (and same tip magnetization direction) are comparable. Unfortunately most SP-STM images were not aimed at providing statistics about molecular orientation. In principle this analysis can be performed with spin-integrated STM images too, because domain walls are visible for particular bias voltages. Since the magnetization direction of the domain is unknown, only single images can be evaluated. Thus spin-integrated STM images can not help to improve the statistics. With the currently available data no unambiguous conclusions can be drawn. Since the difference in adsorption energy is also expected to be very small (less than 1 meV), it might be helpful to cool down the Fe/W(110) substrate to even lower temperatures.

Preliminary theoretical calculations by Rico Friedrich including spin-orbit coupling on a simplified chiral hybrid-molecular magnet show that the total energy of such systems only deviates on an energy scale of 1 meV . Since these questions concerning chirality dependent properties arose at the end of this thesis, it is challenging to give an unambiguous answer at this point. However, several possibilities have been suggested to scrutinize this question in

future experiments.

7.4 Energy and site dependent spin polarization

By the observations described in section 7.3.2 the relation of TPT orientations on opposite magnetic was determined. Subsequently, the two marked TPT molecules in Fig. 7.7a were repeatedly imaged with 100 mV steps in the bias voltage interval [-1 V, 1 V]. The two molecules are adsorbed on opposite magnetic domains of the DL Fe/W(110) substrate and thus are ideal for visualizing the variation of site dependent spin polarization by difference images. Applying this method to images acquired at different bias voltages gives additionally insight on the energy dependence of the spin polarization. Previous reports showed that difference images of both topography and dI/dV maps are useful tools for visualizing the energy-integrated and energy-resolved spin polarization respectively [16, 66].

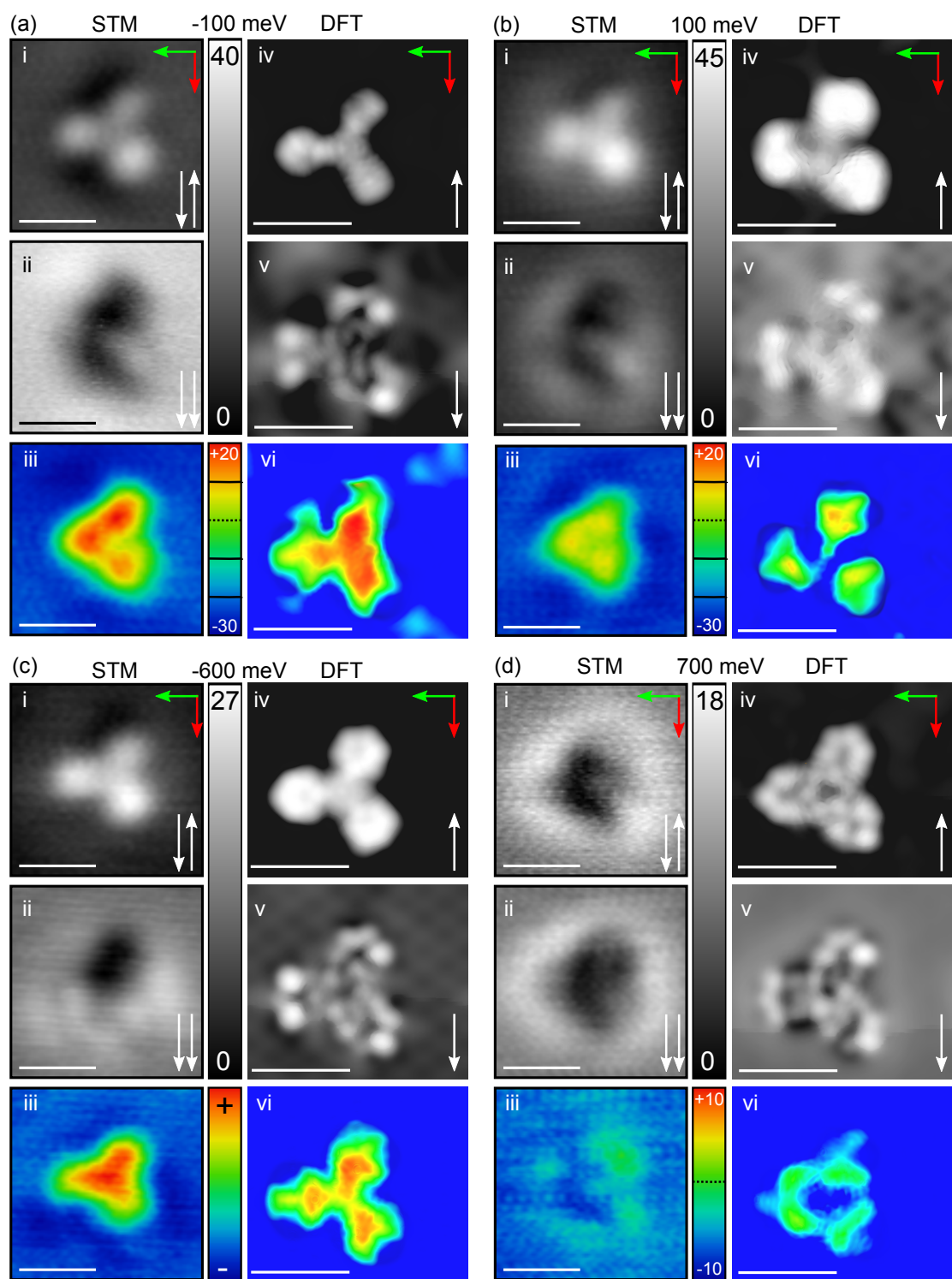
Fig. 7.10 shows an extensive comparison of the two marked molecules in Fig. 7.7a for four different bias voltages compared with the respective DFT images. Both STM topography and DFT images were used for creating difference images.

All images in Fig. 7.10a were obtained at $V_{\text{Bias}} = -100$ mV, similar to most previous images. a-i) and a-ii) show TPT adsorbed on opposite magnetic domains. The white arrows in the respective bottom right corner denote the orientation of tip-sample magnetization, *i.e.* parallel or antiparallel, in the investigated energy interval. In the antiparallel case the TPT looks very similar to the spin-integrated image obtained at the same bias voltage in Fig. 7.3c. In contrast, TPT looks very different in the parallel case. It is characterized by a dark depression with just one brighter lobe. When comparing a-ii) to a-i) a considerable lower LDOS for the a-ii) spin channel of the hybrid-molecular magnet can be deduced. a-i) and a-ii) use the same color scale for the topography given next to images in units of picometer.

One should keep in mind that STM measures both channels weighted with the spin polarization of the tip. Thus both images in a-i) and a-ii) contain some information of the opposite spin channel. The effective spin polarization of the tip-sample junction was calculated for certain bias voltages in section 6.3.3².

Fig. 7.10a-iii) shows the difference image obtained from subtracting [a-i)]-[a-ii)] similar to the procedure described in [16]. The surrounding clean DL Fe/W(110) substrate shows a negative spin polarization as expected. In contrast, the effective spin polarization of the hybrid-molecular magnet is positive and inverse in regard to the substrate. Interestingly the outer phenyl rings exhibit different degrees of spin polarization. The highly non-symmetric adsorption geometry found in section 7.1.2, leading to different binding geometries and electronic properties for each phenyl ring, is considered to be causing this behavior. The triazine ring is not distinguishable due to its lower LDOS. A strong hybridization of TPT was established in the section 7.2.2. The observation of an inversed spin polarization is thus in agreement to the model derived in [51] and previous experiments, *e.g.* H₂Pc on DL

²The effective spin polarization of the junction depends significantly on the tip DOS. Since the measurements leading to the calculations in chapter 6 were performed with the same tip the calculated values are applicable to this particular case.



Fe/W(110) [16].

Since the topography images a-i) and a-ii) are individual images (*i.e.* not zooms of one image), they do not necessarily use the same point of reference for their respective height scales. The height difference of opposite magnetic domains was determined in Fig. 6.8 for particular bias voltages. Thus the height values in the difference image a-iii) for the iron substrate were set to match the respective values obtained in Fig. 6.8. Consequently, the height scale for the difference image is shifted to -30 pm for the DL Fe substrate and reaches +20 pm for the hybrid-molecular magnet. These values can be used to determine the effective spin polarization according to Eq. 2.23. One obtains roughly +10 % for the hybrid-molecular magnet. Due to chosen reference point one obtains an effective spin polarization of -12.4 % for the iron substrate as already determined in section 6.3.3. The total range of the height scale itself is not affected by this method. The black bars in the color scale of a-iii) are arranged in distances of 10 pm with the dotted line indicating 0.

Fig. 7.10a-iv) to a-vi) show the respective DFT images. These images were obtained by only evaluating one spin species (up = majority or down = minority) for the construction of the PDOS isosurface. Similarly to a-i) the spin up DFT image agrees well with the spin-integrated DFT image in Fig. 7.3b. A good agreement between the topography image in a-i) and the DFT image a-iv) is found.

The spin down DFT image in a-v) is considerably different than the spin up DFT image. It is characterized by a significant lower DOS. Consequently the typical "Y" shape of TPT is barely reproduced. In both observations the spin down DFT image agrees qualitatively with the "parallel" SP-STM topography image.

The DFT difference image in Fig. 7.10a-iv) shows a negative spin polarization for substrate as expected and confirms the inversed spin polarization of the hybrid-molecular magnet. Similarly to the experiment the strongest inversion is observed on the phenyl rings. The values of spin polarization for the respective phenyl rings is not exactly identical between DFT and STM. Nevertheless, a good agreement is observed for this particular bias voltage.

In Fig. 7.10b, all images were obtained at $V_{\text{Bias}} = 100$ mV. As already discussed in the context of Fig. 7.6 and Fig. 7.7, changing the bias voltage from negative to positive sign results in minor changes, mostly affecting the halo surrounding TPT. TPT in b-i) is easily identified and appears similar to the spin-integrated case. In comparison to a-i) it appears brighter, indicating a higher LDOS at this energy. Interestingly this trend is reproduced

Figure 7.10 (*preceding page*): Extensive comparison of two hybrid-molecular magnets adsorbed on opposite magnetic domains by SP-STM and DFT. SP-STM topography image parameters: $2.4 \text{ nm} \times 2.4 \text{ nm}$, V_{Bias} given in each block, $I_{\text{T}} = 1 \text{ nA}$, 5 K, gently Gauss filtered (over 2 pixel). The green and red arrows denotes the $[1\bar{1}0]$ -direction and the $[001]$ -direction respectively. White arrows in STM images represent parallel or antiparallel tip-sample magnetization alignment in the respective energy interval. White arrows in DFT represent respective spin species, up or down. Bars in all images equal 1 nm. Height scales are in units of picometer.

by the spin up DFT image in b-iv). The topography image in b-ii) is characterized by a low DOS and TPT appears as negative featureless spot. In contrast to a-ii) a bright halo surrounds TPT in b-ii). The spin down DFT image in b-v) shows also a significant lower DOS than the spin up image in b-iv).

The reference point for the height scale in the difference image in b-iii) was set according to procedure used in a-iii). Consequently both images use the same height scale. Again, the substrate is characterized by a negative spin polarisation. However, the spin polarisation for the hybrid-molecular magnet is different than in a-iii). Both the spatial variation as well as the total degree of effective spin polarization vary. Again, the inversion of spin polarization is strongest on the phenyl rings but reaches now only values of up to 5 %.

All DFT difference images in Fig. 7.10 also use the same respective color scale to allow comparisons between individual images. The DFT difference image in b-vi) reproduces both the qualitative as well as the quantitative behavior of the experimental difference image b-iii). This observation highlights the good agreement between STM and DFT energies close the Fermi level.

All images in Fig. 7.10c were obtained at $V_{\text{Bias}} = -600$ mV. Experimentally a strong influence of tip states was found for large negative bias voltages while DFT predicted hybridized molecular states at this energy (Fig. A.6 in the appendix). Thus a comparison at this energy seems worthwhile. c-i) shows a similar behavior when compared to a-i) and b-i). In contrast c-ii) is different, in that the previously visible bright ring at the right bottom corner now also vanished. The DFT image c-iv) shows very pronounced phenyl rings and c-v) shows a higher DOS compared to the previous spin down DFT images. The similarities between the SP-STM images and the DFT images in Fig. 7.10a-c suggest, that also the appearance of TPT in spin-integrated images is largely dominated by majority spin electrons.

The height scale in c-iii) could not be corrected, because no reference measurement for this bias voltage was recorded. Thus only a qualitative analysis is possible. The spatial variation of spin polarization largely reproduces the "Y"-shape of TPT with no significant intra-molecular differences. This situation is qualitatively reproduced by the DFT difference image.

All images in Fig. 7.10d were obtained at $V_{\text{Bias}} = 700$ mV. At this energy the DL Fe/W(110) substrate exhibits a d_{z^2} -like peak. Thus the spin dependent hybridization of TPT with the substrate might be especially interesting at this energy. However, the high DOS of the DL Fe/W(110) substrate is reflected in both SP-STM images and TPT appears as nearly featureless depression. A similar situation was encountered for the spin-integrated dI/dV -maps at this voltage in Fig. 7.6 but not for the topography images. The DFT images show a behavior similar to the previous cases. A comparison between DFT and STM is not possible at this particular bias voltage. A reference point for the experimental difference image was available and used for d-iii). However, in order to observe structures in d-iii) the color scale was reduced to ± 10 pm. Surprisingly, some sort of agreement is present in the STM and DFT difference image. Whether the influence of the tip is reduced in difference images or this agreement is just by chance can not be unambiguously answered at this point.

In conclusion, the site and energy dependent spin polarization of the hybrid-molecular magnet TPT on DL Fe/W(110) was investigated by SP-STM and DFT. This investigation

revealed a strong inversion of the spin polarization of the hybrid-molecular magnet in regard to the clean iron surface. Furthermore, the non-symmetric adsorption geometry induces significant intra-molecular variations in the spin polarization. A good agreement between experiment and DFT is especially found close to the Fermi level. The comparison between both allows to deduce that the appearance of TPT in spin-integrated STM measurements is largely dominated by majority spin electrons.

7.5 Conclusion

The properties of TPT/Fe/W(110) system were studied by a combination of STM, SP-STM and DFT calculations. As first step of the investigation the adsorption position and geometry of TPT on DL Fe/W(110) were determined with STM. The different rotation symmetries of the iron substrate and the TPT molecule lead to a highly non-symmetric and chiral adsorption geometry. Consequently each aromatic ring in TPT couples differently to the iron substrate. Especially the phenyl rings, which are all equal in gas phase show different brightnesses and shapes in STM experiments.

The adsorption position and geometry was also investigated with DFT by Rico Friedrich, Vasile Caciuc and Nicolae Atodiresei from the PGI-1. Several high-symmetric and the experimentally derived non-symmetric starting geometries were evaluated. The highest adsorption energy was found for the experimentally derived geometry. Thus a good initial agreement between DFT and STM was established.

Subsequently the electronic properties of TPT on DL Fe/W(110) were studied. Spin-integrated STS measurements revealed the same electronic properties for all adsorption orientations as expected. A strong chemisorption was confirmed by only observing broad hybrid states, thus establishing a prerequisite for the formation of a hybrid-molecular magnet. The non-symmetric adsorption geometry leads to intra-molecular differences in the LDOS, which were found to exist over large bias voltage intervals near the Fermi level.

SP-STM topography images and dI/dV-maps finally reveal a spin dependent hybridization by showing significantly different appearances of TPT on opposite magnetic domains. How the adsorption orientations of TPT on opposite magnetic domains relate to each other was determined by reversing the tip magnetization direction by pulsing the bias voltage. A preliminary study concerning an interaction between the chirality of the hybrid-molecular magnet and the magnetic properties of the DL Fe/W(110) was inconclusive. However, several methods to conduct such experiments in future have been suggested.

Finally the site and energy dependent spin polarization of the hybrid-molecular magnet is investigated. SP-STM difference images reveal a highly site and energy dependent spin polarization. A comparison with images obtained by DFT shows both qualitative and quantitative agreement close to Fermi level. Mostly majority spin electrons contribute to the TPT appearance in STM.

The results obtained by studying the TPT/Fe/W(110) system highlight the possibilities of tuning the properties of organic-ferromagnetic interfaces. Besides using different molecules, the properties of organic-ferromagnetic interfaces can be also designed by realizing varying adsorption geometries. TPT on DL Fe/W(110) shows impressively that even intra-molecular

differences in adsorption geometry lead to considerable variations regarding the electronic properties as well as the spin polarization.

Chapter 8

Summary and Outlook

Single-molecule magnets and hybrid-molecular magnets are ideal building blocks for the realization of molecular spintronic devices. While considerable progress has been made, their widespread use is still inhibited by many obstacles. The controlled deposition on suitable surfaces and understanding the related adsorption phenomena is one of the biggest challenges. Thus finding and evaluating strategies for overcoming these obstacles is a major goal of fundamental research.

For this task, the interaction of single-molecule magnets with surfaces and the formation of hybrid-molecular magnets have been investigated in this dissertation. Since surfaces are prone to contamination, these studies have been conducted in ultra-high vacuum. The structural and electronic properties of both systems have been analysed by STM and STS with sub-nanometer spatial resolution.

The interaction between SMMs and surfaces was exemplarily studied by depositing $\{\text{Ni}_4\}$ on Au(111). $\{\text{Ni}_4\}$ is a recently synthesized SMM where a cubane $\{\text{Ni}_4^{\text{II}}(\mu_3\text{-Cl})_4\}$ core is responsible for the magnetic properties [1]. The magnetic core is protected by organic ligands exhibiting a thioether surface functionalization. Since thioether functionalized ligands had been widely neglected in earlier experiments, the deposition of $\{\text{Ni}_4\}$ on Au(111) from solution and the resulting adsorption phenomena were studied by XPS and STM. Both methods revealed strong evidence for a ligand detachment during adsorption. The magnetic core however might be still structurally intact as indicated by XPS. Attempts to desorb the detached ligands and to subsequently image the magnetic core with STM by *in-situ* post-annealing were unsuccessful. Instead the post-annealing lead to the decomposition of the magnetic core and to a most likely sulfur induced reconstruction of the Au(111) surface. Future XMCD measurements will hopefully reveal the magnetic properties of the isolated $\{\text{Ni}_4\}$ core in the as-deposited state.

The case of $\{\text{Ni}_4\}/\text{Au}(111)$ highlights the importance of the molecule-surface interaction. As a result of the XPS and STM investigation on $\{\text{Ni}_4\}/\text{Au}(111)$ it was possible to derive new strategies for avoiding a ligand detachment in future experiments. These strategies are:

1. strengthening of the metal-ligand bonds by introducing strong π -backbonding organic ligands and/or strongly negatively charged chelating (redox) ligands and
2. reduction of the number of ligands/anchoring groups per complex so that all of them

can bind to the substrate surface with no significant molecular deformation or ligand decoordination.

In contrast, in the case of hybrid-molecular magnets, the interaction between a magnetic surface and non-magnetic molecules is exploited for the formation of a molecule-surface hybrid with magnetic properties. A frequently used approach for fabricating hybrid-molecular magnets is depositing organic molecules on ferromagnetic thin films. The characterization of hybrid-molecular magnets requires a method which is sensitive to the magnetic properties of such nanoscopic systems. In this regard SP-STM is ideal since it allows to probe the structural, electronic and magnetic properties on a sub-nanometer length scale. However, SP-STM is a highly sophisticated experimental technique and needs to be reliably established first.

The low coverage regime of Fe/W(110) was chosen as ferromagnetic substrate for the formation of hybrid-molecular magnets and was simultaneously used for establishing SP-STM operation. The fabrication of suitable magnetic tips for SP-STM is a well known challenge due to its poor predictability and reproducibility. Magnetic tips were eventually successfully prepared by coating standard tungsten tips with iron or chromium. The characterization of these tips by measurements on the Fe/W(110) system reveals that Cr-coated tips exhibit the necessary out-of-plane magnetization direction for the following experiments on hybrid-molecular magnet systems. Furthermore an effective spin polarization of up to 12.4% for the tip-sample tunnel junction was found.

Triphenyl-triazine (TPT) was chosen for studying the spin dependent hybridization on Fe/W(110). TPT is a flat organic molecule which exhibits different aromatic rings. Molecules comprising different aromatic rings have not yet been studied in the context of spin dependent hybridization and could potentially lead to the formation of several individually switchable units. The TPT/Fe/W(110) system was investigated by SP-STM and STS as well as DFT calculations made by Rico Friedrich, Vasile Caciuc and Nicolae Atodiresei from PGI-1.

After depositing TPT on Fe/W(110) by sublimation the adsorption position and geometry were determined by STM. A highly non-symmetric and chiral adsorption geometry was found. The experimentally determined adsorption position and geometry were confirmed by DFT to be highest in adsorption energy. This observation highlights the importance of experimental input to DFT and establishes an initial good agreement between theory and experiment. Subsequently the electronic properties of TPT on Fe/W(110) were scrutinized. The observation of broad electronic states confirms a strong interaction between molecule and substrate and thus establishes one prerequisite for the formation of a hybrid-molecular magnet. Differences in the electronic properties of the individual phenyl rings arise from the highly non-symmetric adsorption position.

SP-STM finally reveals a highly site and energy dependent spin polarization and showcases the tuneability of organic-ferromagnetic interfaces. Difference images were used to visualize the spatial variation of the effective spin polarization. These images revealed differences for individual phenyl rings. Since all phenyl rings in TPT are forced to realize different adsorption geometries, the influence of adsorption position and geometry on electronic properties and spin polarization can be studied in such systems. A good

qualitative and quantitative agreement with DFT calculation was found close to Fermi level. No impact of the chirality of the hybrid-molecular magnet and magnetism of the Fe/W(110) substrate were experimentally found. However, several methods to conduct such experiments in future have been suggested.

The results obtained by studying the TPT/Fe/W(110) system highlight the possibilities of tuning the properties of organic-ferromagnetic interfaces. Besides using different molecules, the properties of organic-ferromagnetic interfaces can be also designed by realizing varying adsorption geometries. TPT on DL Fe/W(110) shows impressively that even intra-molecular differences in adsorption geometry lead to considerable variations regarding the electronic properties as well as the spin polarization.

In conclusion both approaches to nanoscopic magnets in molecular spintronic have been investigated. Concerning the question whether one approach is ultimately superior, the only answer can be: It depends. SMMs show an enormous variety and have already been studied for two decades. Thus their properties are generally well understood, with the molecule-surface interaction due to its complexity being one exception. If the need for low temperatures is not an exclusion criterion, SMMs show appealing properties for a wide range of applications.

If operation close to or above room temperature is of utmost importance, hybrid-molecular magnets are certainly better suited. The operation of devices using hybrid-molecular magnets at 250 K has been successfully demonstrated [17] and eventually reaching room temperature operation seems plausible. Perhaps the biggest asset of this approach is the basically unlimited variety in designing the properties of organic-ferromagnetic interfaces by depositing suitable molecules on magnetic surfaces. Combined with the possibility of room-temperature operation this approach is very likely to be used for future devices.

Besides studying the general interaction of molecules with surfaces, future experiments on the switching behavior of SMMs and hybrid-molecular magnets are of high importance. Switching such nanoscopic magnets collectively by external magnetic fields has been repeatedly demonstrated [84, 68]. However, for most applications, such as high density storage or quantum computing, it is important to be able to switch nanoscopic magnets independently. While single atoms on surfaces [70] and magnetic nanoparticles [69] could be successfully manipulated by injecting spin-polarized currents in SP-STM, similar experiments on molecular magnets have not been reported yet.

Such experiments appear very rewarding, but are also highly sophisticated. If one wants to perform this experiment with SP-STM, a complete *in-situ* sample preparation is strongly recommended. However, only few SMMs are sublimable. Furthermore, in order for SP-STM to detect the magnetization direction of the SMM, its spin polarized molecular states have to participate in electric transport. Last but not least the blocking temperature needs to be high enough for typical low temperature STMs.

Also investigating the design of the properties of organic-ferromagnetic interfaces by using varying molecules appears rewarding. Especially studies with molecules where one constituent is systematically replaced would certainly enhance the understanding of the spin dependent hybridization.

As can be seen molecular spintronics is a fascinating multi disciplinary research area. Only by combined efforts of chemists and experimental and theoretical physicists, the many

remaining challenges can be overcome.

Appendices

Appendix A

A.1 Electrochemical analysis of a Ni₄-functionalized gold electrode

The cyclic voltammogram was measured by Claire Besson and Frank Matthes und published in the supplemental material of [80].

Fig. A.1 compares the cyclic voltammogram of a gold electrode, which is functionalized by the same treatment applied to the Au crystal for the *in-situ* measurements, with that of a glassy carbon electrode in a solution of {Ni₄} after the {Ni₄} has undergone one-electron, non-reversible oxidation during the first cycle. In both cases we observe correlated oxidation and reduction waves at -1.3 ± 0.1 V and -0.2 ± 0.2 V *versus* Ag⁺/Ag, respectively (vertical dashes in Fig. A.1). The comparison indicates that the species deposited on the gold is distinct from the intact {Ni₄} complex and that the ligand decoordination process observed upon absorption is most likely initiated by electron transfer from the molecule to the metallic substrate and, hence, gives additional evidence for a ligand decoordination upon interaction with the gold surface.

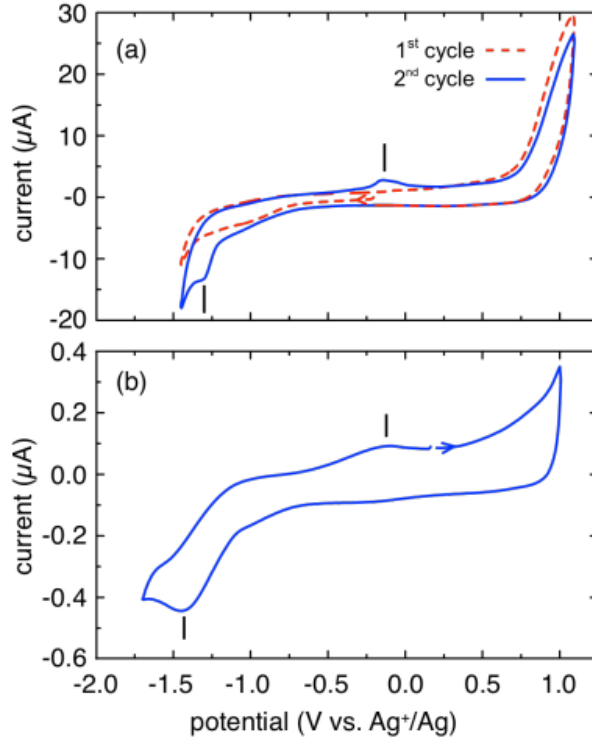


Figure A.1: Cyclic voltammetry of (a) a 1 mM solution of $\{\text{Ni}_4\}$ using a glassy carbon electrode and (b) a gold electrode preliminarily functionalized by dunking for one hour in a 0.6 mM dichloromethane solution of $\{\text{Ni}_4\}$ and rinsing for one hour in dichloromethane. In both cases the electrolyte is 0.25 M in ${}^n\text{Bu}_4\text{NClO}_4$ in dichloromethane, the counter electrode a platinum wire, and the reference electrode a silver wire in contact with a 0.01 M AgNO_3 and 0.1 M ${}^n\text{Bu}_4\text{NClO}_4$ acetonitrile solution. The scanning speed is 0.1 Vs1.

A.2 Domain wall fitting

In section 6.3.3 the following equation was used to fit the line profiles of domain walls [103]:

$$I(x) = I_0 + I_{\text{sp}} \cdot \cos \left(\theta + \sum_{i=1}^2 \arccos \left[\tanh \frac{x - x_i}{w/2} \right] \right) \quad (\text{A.1})$$

Line profiles were obtained with different bias voltages. The fits using Eq. A.1 yielded different results for the tip magnetization direction θ and the domain wall width w . In order to see how meaningful these deviations are Eq. A.1 was plotted for different parameters.

Fig. A.2a shows the resulting curves for varying values of θ over two domain walls, similar to the line profiles in Fig. 6.8. Fig. A.2b shows the same plot zoomed into one single domain wall. Especially in the cases of very small angles (*i.e.* 0° , 5° , 15°) the resulting curves vary only slightly. This behaviour indicates that the variation in angles obtained from the fits in section 6.3.3 might be rather the result of measurement inaccuracy then

from a true physical origin.

A similar evaluation was performed for varying domain wall widths w . Again, Fig. A.2c shows the resulting curves for varying values of w over two domain walls, similar to the line profiles in Fig. 6.8. Fig. A.2d shows the same plot zoomed into one single domain wall. The curves do vary only slightly. However, the width of domain walls in DL Fe/W(110) is well documented [103, 140] and should considerably deviate from 7 nm.

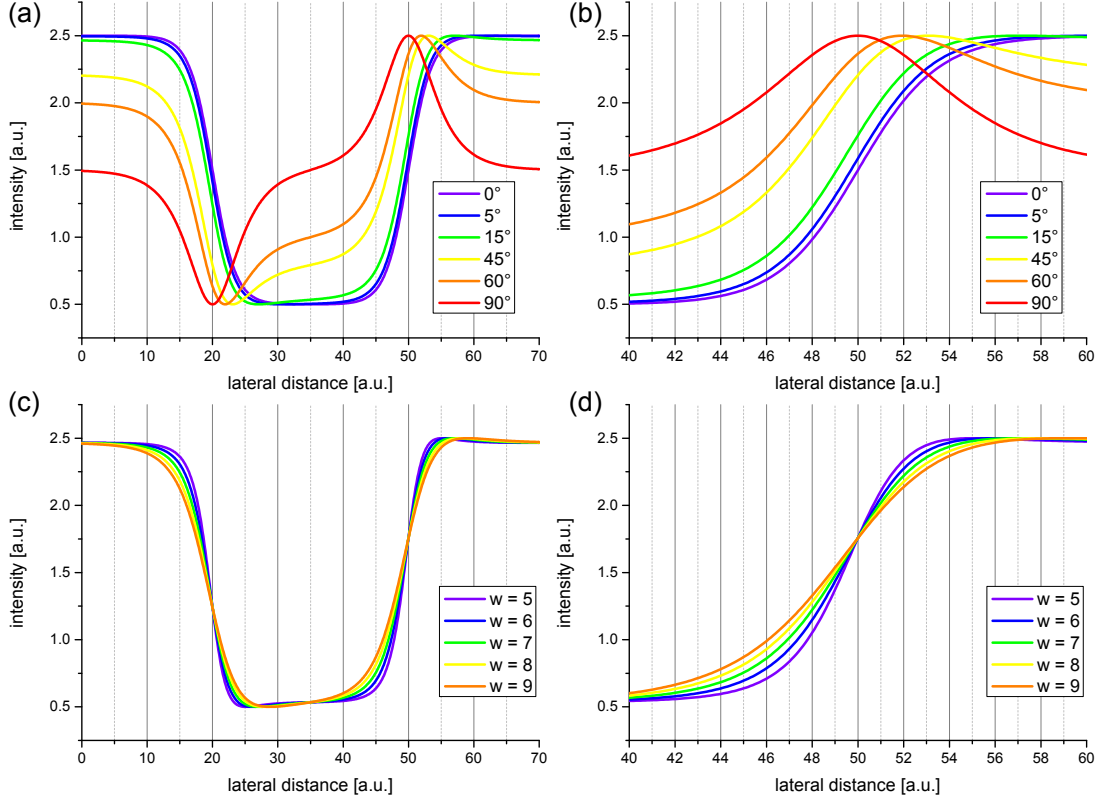


Figure A.2: Equation A.1 plotted for different parameters: $x_1 = 20$, $x_2 = 50$, $I_0 = 1.5$, $I_{sp} = 1$. a) and b) $w = 7$ and varying values for θ given in the legend. c) and d) $\theta = 15^\circ$ and varying values for w given in the legend.

The deviation in θ and w is understood by plotting both fits B1 and B2 (w fixed at 7 nm) together with the experimental data. Both fits agree within 1 % deviation to the experimental data, indicating that the different values for θ and w obtained from the plots are results of the fitting procedure and not due to a physical effect.

In some cases reasonable fits of the domain wall were not possible, due to an additional spin-orbit-interaction at domain walls for certain bias voltages [147]. Since this additional contribution is not accounted for by Eq. A.1, a reasonable domain wall fit is inhibited.

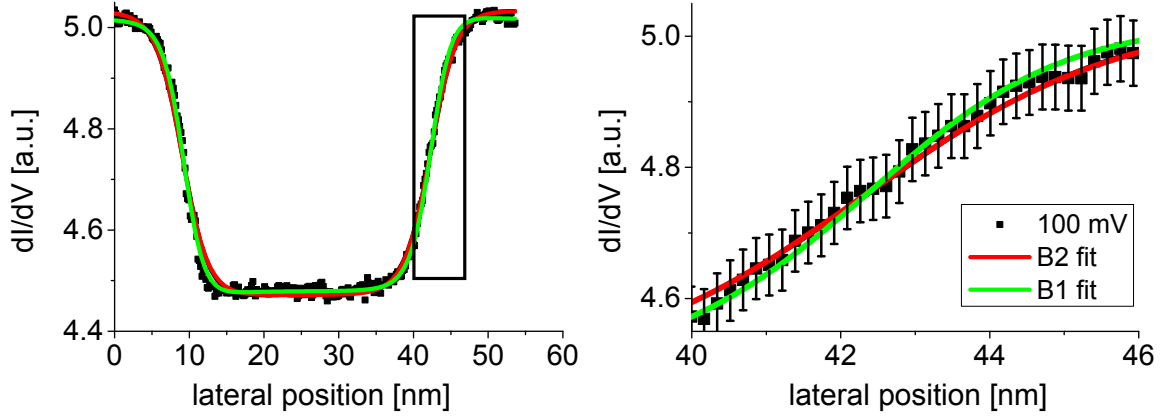


Figure A.3: Experimental data at $V_{\text{Bias}}=100$ mV plotted together with fits B1 and B2 from table 6.1. The right diagram is a zoom of the interval indicated by the black box in the left diagram. Error bars equal 1% of each experimental value.

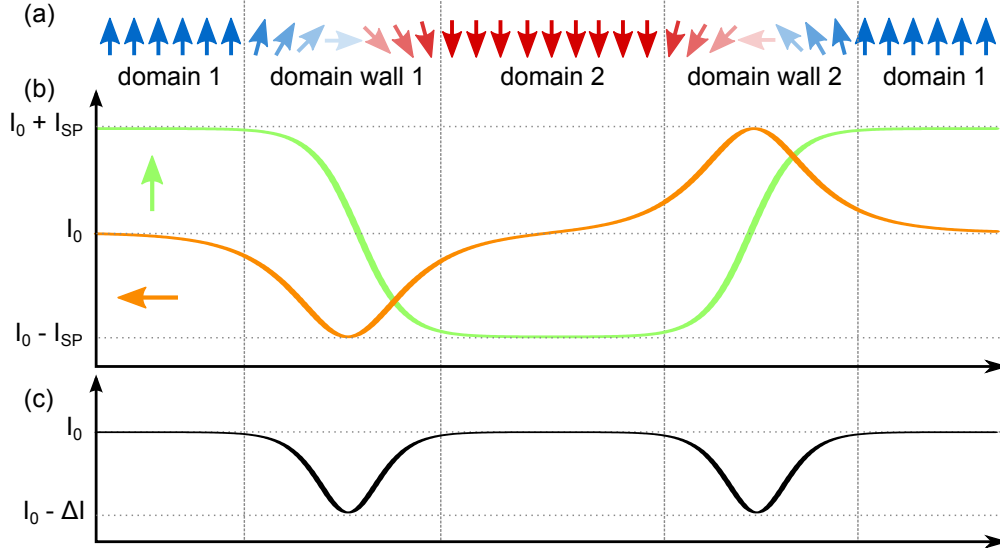


Figure A.4: Expected line profiles at domain walls: a) Magnetic structure of three domains DL Fe/W(110) b) Imaged with magnetic tips: green - OOP, orange - IP, c) Additional spin-orbit interaction at domain walls for certain bias voltages for any tip.

A.3 Electronic properties of isolated TPT

Fig. A.5 shows the energetic position and symmetry of molecular orbitals near the Fermi level of an isolated TPT molecule in gas phase. The σ -HOMO is located on the central triazine ring. The HOMO-1 is a π -molecular orbital delocalized over the whole molecule.

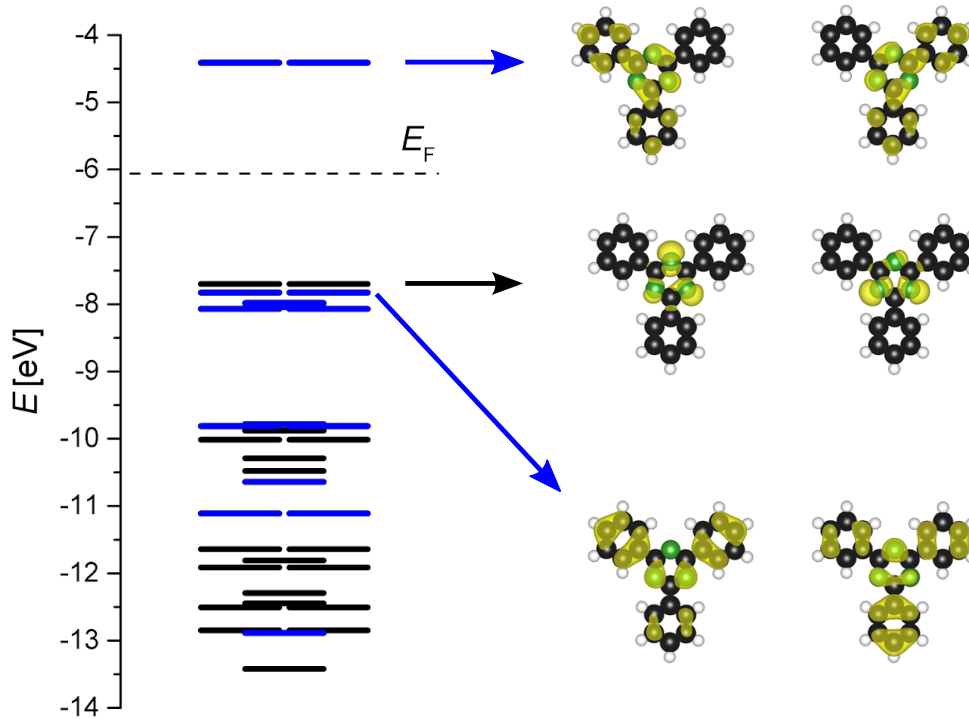


Figure A.5: Molecular orbitals of an isolated TPT molecule in gas phase. Black bars depict orbitals with σ -symmetry. Blue bars depict orbitals with π -symmetry. The HOMO is of σ -symmetry, while the LUMO has π -symmetry. Obtained by DFT simulations from Rico Friedrich.

A.4 Site dependent LDOS and PDOS of TPT/Fe/W(110)

Fig. A.6 shows a comparison of each individual TPT ring together with the iron reference and the projected DOS (PDOS) of states with π -symmetry calculated by DFT. The PDOS is calculated by considering a small sphere around the nuclei of the respective rings atoms and summing over all states in this sphere. In contrast, STM measures the LDOS. As such the PDOS does not consider varying decay lengths of the states into vacuum or tunnel matrix elements.

As seen in Fig. 7.5a-d, the LDOS for negative bias voltages in the interval [-1000;-250] meV seems to be largely dominated by tips states. However, the TPT peak at -600 meV found for all rings in varying intensity is reflected in the DOS. The agreement around the Fermi level appears good, with a broad peak of TPT, which most likely stems from the hybridization with the irons d_{z^2} -like state at this energy.

The TPT peak in the PDOS around 250 meV appears in varying intensity in the PDOS, but is not experimentally observed. The reasons for this particular behavior are unknown. However, one of the aforementioned reasons of low decay length or forbidden tunneling matrix element seem plausible. The TPT peak or shoulder at 700 meV is again most likely

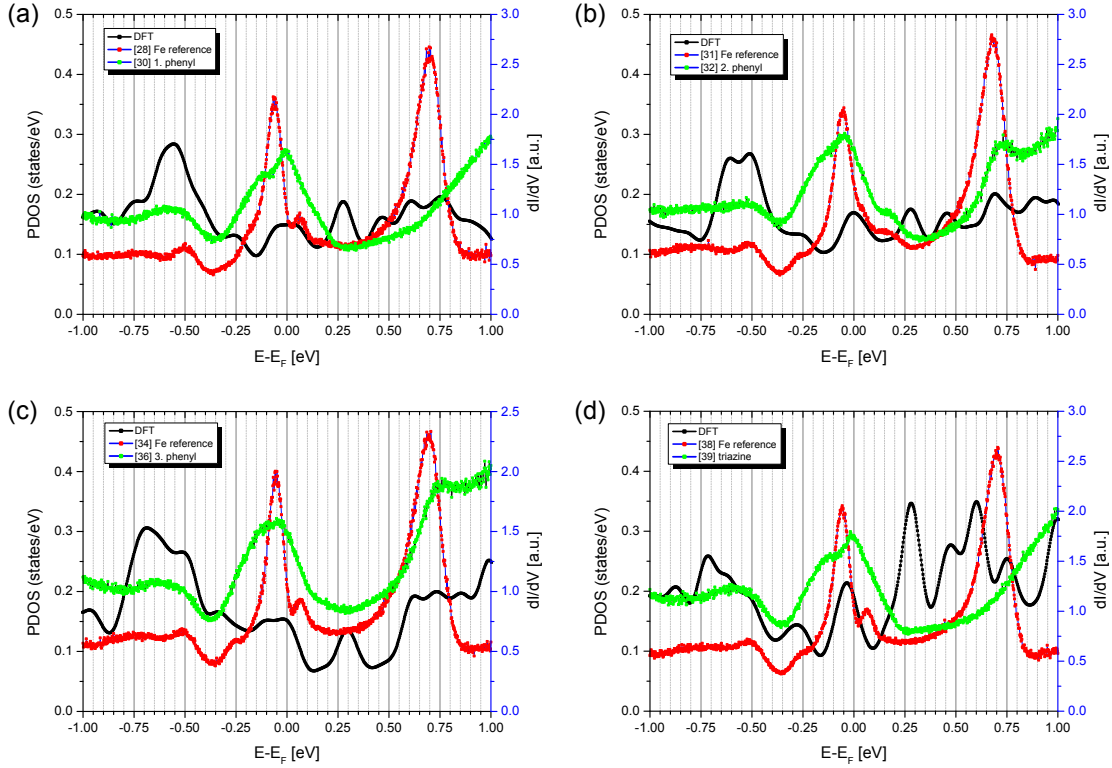


Figure A.6: TPT spectra from Fig. 7.5c with respective Fe reference measurements. The calculated PDOS of states with π -symmetry is plotted as black line for all respective aromatic rings to allow a comparison of theory and experiment. Left y-axis belongs to the calculated PDOS (black line). Right y-axis belongs to STS measurements (green and red lines). STS parameters: $V_{\text{Stab}} = -100$ mV, $I_{\text{Stab}} = 1$ nA.

a result of the hybridization with DL Fe/W(110) substrate. It is partially reproduced in calculated PDOS *e.g.* in Fig. 7.5b and c.

A closer inspection of the spectra reveals a better agreement than visible at the first sight. One has to keep in mind, that the DFT calculations lead to a PDOS very close to the atoms. In STS one conducts a transport experiment several angstrom away from the surface. Thus both quantities can not be compared directly. However, all STS peak positions are reproduced by the PDOS. The opposite case would however question the comparability of theory and experiment. The case of strongly hybridized molecules is additionally more difficult than in the case of weakly interacting or partially decoupled molecules, as *e.g.* in [118].

Chapter 9

Bibliography

- [1] Ghisolfi, A. *et al.* A comparative synthetic, magnetic and theoretical study of functional M_4Cl_4 cubane-type Co(II) and Ni(II) complexes. *Dalton T.* **43**, 7847–7859 (2014). iii, v, 3, 35, 36, 49, 54, 101
- [2] Reed, M. A., Zhou, C., Muller, C., Burgin, T. & Tour, J. Conductance of a molecular junction. *Science* **278**, 252–254 (1997). 1
- [3] Park, J. *et al.* Coulomb blockade and the Kondo effect in single-atom transistors. *Nature* **417**, 722–725 (2002). 1
- [4] Choi, S. H., Kim, B. & Frisbie, C. D. Electrical resistance of long conjugated molecular wires. *Science* **320**, 1482–1486 (2008). 1
- [5] Kido, J., Kimura, M. & Nagai, K. Multilayer white light-emitting organic electroluminescent device. *Science* **267**, 1332–1334 (1995). 1
- [6] Hoppe, H. & Sariciftci, N. S. Organic solar cells: An overview. *Journal of Materials Research* **19**, 1924–1945 (2004). 1
- [7] Kong, J. *et al.* Nanotube molecular wires as chemical sensors. *Science* **287**, 622–625 (2000). 1
- [8] Bogani, L. & Wernsdorfer, W. Molecular spintronics using single-molecule magnets. *Nat. Mater.* **7**, 179–186 (2008). 1, 2, 17, 18, 20, 21, 22, 33
- [9] Baibich, M. N. *et al.* Giant magnetoresistance of (001)Fe/(001)Cr magnetic superlattices. *Phys. Rev. Lett.* **61**, 2472–2475 (1988). 1, 17
- [10] Binasch, G., Grünberg, P., Saurenbach, F. & Zinn, W. Enhanced magnetoresistance in layered magnetic structures with antiferromagnetic interlayer exchange. *Phys. Rev. B* **39**, 4828–4830 (1989). 1, 17
- [11] Sanvito, S. Molecular spintronics. *Chemical Society Reviews* **40**, 3336–3355 (2011). 2, 17, 18

- [12] Sessoli, R. *et al.* High-spin molecules: $[\text{Mn}_{12}\text{O}_{12}(\text{O}_2\text{CR})_{16}(\text{H}_2\text{O})_4]$. *Journal of the American Chemical Society* **115**, 1804–1816 (1993). 2
- [13] Ishikawa, N., Sugita, M., Ishikawa, T., Koshihara, S.-y. & Kaizu, Y. Mononuclear lanthanide complexes with a long magnetization relaxation time at high temperatures: A new category of magnets at the single-molecular level. *The Journal of Physical Chemistry B* **108**, 11265–11271 (2004). 2, 18
- [14] Leuenberger, M. N. & Loss, D. Quantum computing in molecular magnets. *Nature* **410**, 789–793 (2001). 2, 20
- [15] Mannini, M. *et al.* XAS and XMCD investigation of Mn_{12} monolayers on gold. *Chem-Eur. J.* **14**, 7530–7535 (2008). 2, 34
- [16] Atodiressei, N. *et al.* Design of the local spin polarization at the organic-ferromagnetic interface. *Phys. Rev. Lett.* **105**, 066601 (2010). 2, 29, 31, 32, 63, 68, 75, 80, 81, 89, 91, 94, 96
- [17] Raman, K. V. *et al.* Interface-engineered templates for molecular spin memory devices. *Nature* **493**, 509–513 (2013). 2, 18, 28, 30, 31, 36, 75, 103
- [18] Binnig, G., Rohrer, H., Gerber, C. & Weibel, E. Surface studies by scanning tunneling microscopy. *Phys. Rev. Lett.* **49**, 57 (1982). 5
- [19] Binnig, G., Rohrer, H., Gerber, C. & Weibel, E. Tunneling through a controllable vacuum gap. *Applied Physics Letters* **40**, 178–180 (1982). 5
- [20] Binnig, G., Rohrer, H., Gerber, C. & Weibel, E. 7×7 reconstruction on Si(111) resolved in real space. *Phys. Rev. Lett.* **50**, 120–123 (1983). 6
- [21] Chen, C. J. *Introduction to Scanning Tunneling Microscopy* (Oxford University Press, 2007). 8
- [22] Bardeen, J. Tunnelling from a many-particle point of view. *Phys. Rev. Lett.* **6**, 57 (1961). 9
- [23] Giaever, I. Energy gap in superconductors measured by electron tunneling. *Phys. Rev. Lett.* **5**, 147–148 (1960). 9
- [24] Tersoff, J. & Hamann, D. Theory and application for the scanning tunneling microscope. *Phys. Rev. Lett.* **50**, 1998 (1983). 10, 14
- [25] Brune, H. *et al.* Interaction of oxygen with Al(111) studied by scanning tunneling microscopy. *The Journal of chemical physics* **99**, 2128–2148 (1993). 10
- [26] Chen, C. J. Tunneling matrix elements in three-dimensional space: The derivative rule and the sum rule. *Phys. Rev. B* **42**, 8841 (1990). 10
- [27] Ukraintsev, V. A. Data evaluation technique for electron-tunneling spectroscopy. *Phys. Rev. B* **53**, 11176–11185 (1996). 10, 11, 12

- [28] Hamers, R. Atomic-resolution surface spectroscopy with the scanning tunneling microscope. *Annual Review of Physical Chemistry* **40**, 531–559 (1989). 12
- [29] Feenstra, R., Stroscio, J. A. & Fein, A. Tunneling spectroscopy of the Si(111) 2×1 surface. *Surf. Sci.* **181**, 295–306 (1987). 12
- [30] Stroscio, J. A., Feenstra, R. M. & Fein, A. P. Electronic structure of the Si(111) 2×1 surface by scanning-tunneling microscopy. *Phys. Rev. Lett.* **57**, 2579–2582 (1986). 12
- [31] Tedrow, P. M. & Meservey, R. Spin-dependent tunneling into ferromagnetic nickel. *Phys. Rev. Lett.* **26**, 192–195 (1971). 13
- [32] Julliere, M. Tunneling between ferromagnetic films. *Physics letters A* **54**, 225–226 (1975). 13
- [33] Slonczewski, J. C. Conductance and exchange coupling of two ferromagnets separated by a tunneling barrier. *Phys. Rev. B* **39**, 6995–7002 (1989). 13
- [34] Wortmann, D., Heinze, S., Kurz, P., Bihlmayer, G. & Blügel, S. Resolving complex atomic-scale spin structures by spin-polarized scanning tunneling microscopy. *Phys. Rev. Lett.* **86**, 4132–4135 (2001). 15
- [35] Wiesendanger, R., Güntherodt, H.-J., Güntherodt, G., Gambino, R. & Ruf, R. Observation of vacuum tunneling of spin-polarized electrons with the scanning tunneling microscope. *Phys. Rev. Lett.* **65**, 247 (1990). 15, 31, 70
- [36] Bode, M. Spin-polarized scanning tunnelling microscopy. *Reports on Progress in Physics* **66**, 523 (2003). 15, 46
- [37] Wiesendanger, R. Spin mapping at the nanoscale and atomic scale. *Reviews of Modern Physics* **81**, 1495 (2009). 15, 46, 68
- [38] Heinze, S. *et al.* Spontaneous atomic-scale magnetic skyrmion lattice in two dimensions. *Nature Physics* **7**, 713–718 (2011). 15
- [39] Oka, H. *et al.* Spin-dependent quantum interference within a single magnetic nanostructure. *Science* **327**, 843–846 (2010). 15
- [40] Bickel, J. E. *et al.* Magnetic properties of monolayer Co islands on Ir(111) probed by spin-resolved scanning tunneling microscopy. *Phys. Rev. B* **84**, 054454 (2011). 15
- [41] Pierce, D. T. & Meier, F. Photoemission of spin-polarized electrons from GaAs. *Phys. Rev. B* **13**, 5484–5500 (1976). 17
- [42] Tserkovnyak, Y., Brataas, A. & Bauer, G. E. W. Enhanced gilbert damping in thin ferromagnetic films. *Phys. Rev. Lett.* **88**, 117601 (2002). 17
- [43] Sandweg, C. W. *et al.* Spin pumping by parametrically excited exchange magnons. *Phys. Rev. Lett.* **106**, 216601 (2011). 17

- [44] D'yakonov, M. & Perel, V. Possibility of orienting electron spins with current. *Soviet Journal of Experimental and Theoretical Physics Letters* **13**, 467 (1971). 17
- [45] Gajek, M. *et al.* Tunnel junctions with multiferroic barriers. *Nature Mater.* **6**, 296–302 (2007). 17
- [46] Khajetoorians, A. A., Wiebe, J., Chilian, B. & Wiesendanger, R. Realizing all-spin-based logic operations atom by atom. *Science* **332**, 1062–1064 (2011). 18
- [47] Urdampilleta, M., Klyatskaya, S., Cleuziou, J.-P., Ruben, M. & Wernsdorfer, W. Supramolecular spin valves. *Nature Mater.* **10**, 502–506 (2011). 18
- [48] Callsen, M., Caciuc, V., Kiselev, N., Atodiresei, N. & Blügel, S. Magnetic hardening induced by nonmagnetic organic molecules. *Phys. Rev. Lett.* **111**, 106805 (2013). 18, 28, 29, 75
- [49] Lazić, P., Caciuc, V., Atodiresei, N., Callsen, M. & Blügel, S. First-principles insights into the electronic and magnetic structure of hybrid organic-metal interfaces. *Journal of Physics: Condensed Matter* **26**, 263001 (2014). 19, 24, 80
- [50] Lis, T. Preparation, structure, and magnetic properties of a dodecanuclear mixed-valence manganese carboxylate. *Acta Crystallographica Section B: Structural Crystallography and Crystal Chemistry* **36**, 2042–2046 (1980). 22
- [51] Galbiati, M. *et al.* Spininterface: Crafting spintronics at the molecular scale. *MRS Bulletin* **39**, 602–607 (2014). 23, 24, 26, 27, 28, 36, 94
- [52] Perrin, M. L. *et al.* Large tunable image-charge effects in single-molecule junctions. *Nature nanotechnology* **8**, 282–287 (2013). 23
- [53] Langreth, D. *et al.* A density functional for sparse matter. *Journal of Physics: Condensed Matter* **21**, 084203 (2009). 23
- [54] Neaton, J. B., Hybertsen, M. S. & Louie, S. G. Renormalization of molecular electronic levels at metal-molecule interfaces. *Phys. Rev. Lett.* **97**, 216405 (2006). 23
- [55] Garcia-Lastra, J. M., Rostgaard, C., Rubio, A. & Thygesen, K. S. Polarization-induced renormalization of molecular levels at metallic and semiconducting surfaces. *Phys. Rev. B* **80**, 245427 (2009). 23
- [56] Lennartz, M. C., Caciuc, V., Atodiresei, N., Karthäuser, S. & Blügel, S. Electronic mapping of molecular orbitals at the molecule-metal interface. *Phys. Rev. Lett.* **105**, 066801 (2010). 23
- [57] Caciuc, V., Lennartz, M., Atodiresei, N., Karthäuser, S. & Blügel, S. Fine tuning of the electronic structure of π -conjugated molecules for molecular electronics. *Nanotechnology* **22**, 145701 (2011). 23

- [58] Harutyunyan, H. *et al.* Hybridisation at the organic–metal interface: a surface-scientific analogue of Hückel’s rule? *Chemical Communications* **49**, 5993–5995 (2013). 24, 25
- [59] Atodiresei, N., Caciuc, V., Lazić, P. & Blügel, S. Chemical versus van der Waals interaction: The role of the heteroatom in the flat absorption of aromatic molecules C_6H_6 , C_5NH_5 , and $C_4N_2H_4$ on the Cu(110) surface. *Phys. Rev. Lett.* **102**, 136809 (2009). 26, 36, 77, 80, 81
- [60] Atodiresei, N., Caciuc, V., Lazić, P. & Blügel, S. Engineering the magnetic properties of hybrid organic-ferromagnetic interfaces by molecular chemical functionalization. *Phys. Rev. B* **84**, 172402 (2011). 26
- [61] Elmers, H. J. *et al.* Submonolayer magnetism of Fe(110) on W(110): Finite width scaling of stripes and percolation between islands. *Phys. Rev. Lett.* **73**, 898–901 (1994). 26, 63
- [62] Stampanoni, M., Vaterlaus, A., Aeschlimann, M., Meier, F. & Pescia, D. Magnetic properties of thin fcc iron films on Cu(001) (invited). *Journal of Applied Physics* **64**, 5321–5324 (1988). 26
- [63] Barraud, C. *et al.* Unravelling the role of the interface for spin injection into organic semiconductors. *Nature Physics* **6**, 615–620 (2010). 27
- [64] Santos, T. S. & Moodera, J. S. Observation of spin filtering with a ferromagnetic EuO tunnel barrier. *Phys. Rev. B* **69**, 241203 (2004). 28
- [65] Iacovita, C. *et al.* Visualizing the spin of individual cobalt-phthalocyanine molecules. *Phys. Rev. Lett.* **101**, 116602 (2008). 31, 63, 75
- [66] Brede, J. & Wiesendanger, R. Spin-resolved characterization of single cobalt phthalocyanine molecules on a ferromagnetic support. *Phys. Rev. B* **86**, 184423 (2012). 31, 89, 94
- [67] Kawahara, S. *et al.* Large magnetoresistance through a single molecule due to a spin-split hybridized orbital. *Nano letters* **12**, 4558–4563 (2012). 31
- [68] Brede, J. *et al.* Long-range magnetic coupling between nanoscale organic–metal hybrids mediated by a nanoskymion lattice. *Nature nanotechnology* (2014). 32, 36, 75, 103
- [69] Krause, S., Berbil-Bautista, L., Herzog, G., Bode, M. & Wiesendanger, R. Current-induced magnetization switching with a spin-polarized scanning tunneling microscope. *Science* **317**, 1537–1540 (2007). 32, 103
- [70] Khajetoorians, A. A. *et al.* Current-driven spin dynamics of artificially constructed quantum magnets. *Science* **339**, 55–59 (2013). 32, 103

- [71] Tanaka, H. *et al.* Network of Tris(porphyrinato)cerium(iii) arranged on the herringbone structure of an Au(111) surface. *Langmuir* **26**, 210–214 (2009). 33
- [72] Pérez León, C. *et al.* STM investigation of large π -conjugated oligomers and tetrahydrofuran codeposited on Cu(111) by pulse injection. *The Journal of Physical Chemistry C* **113**, 14335–14340 (2009). 33
- [73] Rauschenbach, S. *et al.* Electrospray ion beam deposition of clusters and biomolecules. *Small* **2**, 540–547 (2006). 33
- [74] Vitali, L. *et al.* Electronic structure of surface-supported bis(phthalocyaninato)terbium(iii) single molecular magnets. *Nano letters* **8**, 3364–3368 (2008). 33
- [75] Love, J. C., Estroff, L. A., Kriebel, J. K., Nuzzo, R. G. & Whitesides, G. M. Self-assembled monolayers of thiolates on metals as a form of nanotechnology. *Chemical reviews* **105**, 1103–1170 (2005). 34
- [76] Noh, J. & Hara, M. Nanoscopic evidence for dissociative adsorption of asymmetric disulfide self-assembled monolayers on Au(111). *Langmuir* **16**, 2045–2048 (2000). 34, 35
- [77] Baber, A. E., Tierney, H. L. & Sykes, E. C. H. A quantitative single-molecule study of thioether molecular rotors. *ACS Nano* **2**, 2385–2391 (2008). 34
- [78] Jensen, S. C., Baber, A. E., Tierney, H. L. & H. Sykes, E. C. Dimethyl sulfide on Cu(111): Molecular self-assembly and submolecular resolution imaging. *ACS Nano* **1**, 423–428 (2007). 34, 35
- [79] Pineider, F. *et al.* Deposition of intact tetrairon(III) single molecule magnet monolayers on gold: an STM, XPS, and ToF-SIMS investigation. *J. Mater. Chem.* **20**, 187–194 (2010). 34
- [80] Heß, V. *et al.* Adsorption phenomena of cubane-type tetranuclear Ni(II) complexes with neutral, thioether-functionalized ligands on Au(111). *Surf. Sci.* **641**, 210–215 (2015). 34, 35, 42, 50, 107
- [81] Poirier, G. & Pylant, E. The self-assembly mechanism of alkanethiols on Au(111). *Science* **272**, 1145–1148 (1996). 34, 57
- [82] Dishner, M. H., Hemminger, J. C. & Feher, F. J. Direct observation of substrate influence on chemisorption of methanethiol adsorbed from the gas phase onto the reconstructed Au(111) surface. *Langmuir* **13**, 2318–2322 (1997). 34
- [83] Ito, E., Noh, J. & Hara, M. Adsorption states and thermal desorption behaviors of thiophene derivative self-assembled monolayers on Au(111). *Surf. Sci.* **602**, 3291–3296 (2008). 34
- [84] Mannini, M. *et al.* Quantum tunnelling of the magnetization in a monolayer of oriented single-molecule magnets. *Nature* **468**, 417–421 (2010). 34, 55, 103

- [85] Mannini, M. *et al.* Magnetic memory of a single-molecule quantum magnet wired to a gold surface. *Nat. Mater.* **8**, 194–197 (2009). 34, 55
- [86] Parks, J. *et al.* Mechanical control of spin states in spin-1 molecules and the under-screened Kondo effect. *Science* **328**, 1370–1373 (2010). 35
- [87] Dreiser, J. *et al.* Reduction of Mn₁₉ coordination clusters on a gold surface. *The Journal of Physical Chemistry C* **119**, 3550–3555 (2015). 35
- [88] Rodriguez-Douton, M. J. *et al.* One-step covalent grafting of Fe₄ single-molecule magnet monolayers on gold. *Chemical Communications* **47**, 1467–1469 (2011). 35
- [89] Cornia, A., Mannini, M., Saintavit, P. & Sessoli, R. Chemical strategies and characterization tools for the organization of single molecule magnets on surfaces. *Chemical Society Reviews* **40**, 3076–3091 (2011). 35
- [90] Troughton, E. B. *et al.* Monolayer films prepared by the spontaneous self-assembly of symmetrical and unsymmetrical dialkyl sulfides from solution onto gold substrates: structure, properties, and reactivity of constituent functional groups. *Langmuir* **4**, 365–385 (1988). 35, 49, 55
- [91] Scheurer, A. *et al.* Synthesis, magnetic properties, and STM spectroscopy of cobalt(II) cubanes [Co₄^{II}(Cl)₄(HL)₄]. *Chemistry-A European Journal* **16**, 4784–4792 (2010). 35
- [92] Friedrich, R., Caciuc, V., Kiselev, N. S., Atodiresei, N. & Blügel, S. Chemically functionalized magnetic exchange interactions of hybrid organic-ferromagnetic metal interfaces. *Phys. Rev. B* **91**, 115432 (2015). 36, 80, 81
- [93] Van Hove, M. *et al.* The surface reconstructions of the (100) crystal faces of iridium, platinum and gold: I. experimental observations and possible structural models. *Surf. Sci.* **103**, 189–217 (1981). 41
- [94] Bode, M., Krause, S., Berbil-Bautista, L., Heinze, S. & Wiesendanger, R. On the preparation and electronic properties of clean W(110) surfaces. *Surface science* **601**, 3308–3314 (2007). 42, 43
- [95] Bode, M., Pascal, R. & Wiesendanger, R. STM study of carbon-induced reconstructions on W(110): strong evidence for a surface lattice deformation. *Surface science* **344**, 185–191 (1995). 42, 43
- [96] Balden, M., Lehwald, S. & Ibach, H. Substrate and hydrogen phonons of the ordered *p* (2×1) and (2×2) phase and of the anomalous (1×1) phase of hydrogen on w(110). *Phys. Rev. B* **53**, 7479–7491 (1996). 42, 43
- [97] Esat, T. private communication. 44
- [98] Ibe, J. *et al.* On the electrochemical etching of tips for scanning tunneling microscopy. *Journal of Vacuum Science & Technology A* **8**, 3570–3575 (1990). 44, 45

- [99] Ekvall, I., Wahlström, E., Claesson, D., Olin, H. & Olsson, E. Preparation and characterization of electrochemically etched w tips for STM. *Measurement Science and Technology* **10**, 11 (1999). 44, 45
- [100] Cavallini, M. & Biscarini, F. Electrochemically etched nickel tips for spin polarized scanning tunneling microscopy. *Review of Scientific Instruments* **71**, 4457–4460 (2000). 46
- [101] Koltun, R., Herrmann, M., Güntherodt, G. & Brabers, V. Enhanced atomic-scale contrast on fe₃o₄ (100) observed with an fe STM tip. *Applied Physics A* **73**, 49–53 (2001). 46
- [102] Kubetzka, A., Bode, M., Pietzsch, O. & Wiesendanger, R. Spin-polarized scanning tunneling microscopy with antiferromagnetic probe tips. *Phys. Rev. Lett.* **88**, 057201 (2002). 46, 64, 68
- [103] Schlenhoff, A., Krause, S., Herzog, G. & Wiesendanger, R. Bulk Cr tips with full spatial magnetic sensitivity for spin-polarized scanning tunneling microscopy. *Applied Physics Letters* **97**, 083104 (2010). 46, 61, 63, 64, 65, 68, 71, 72, 73, 83, 84, 85, 108, 109
- [104] Bassi, A. L. *et al.* Bulk cr tips for scanning tunneling microscopy and spin-polarized scanning tunneling microscopy. *Applied Physics Letters* **91**, 173120 (2007). 46
- [105] Yamada, T. K., Bischoff, M., Mizoguchi, T. & van Kempen, H. Use of voltage pulses to detect spin-polarized tunneling. *Applied physics letters* **82**, 1437–1439 (2003). 46
- [106] Berbil-Bautista, L., Krause, S., Bode, M. & Wiesendanger, R. Spin-polarized scanning tunneling microscopy and spectroscopy of ferromagnetic Dy(0001)/W(110) films. *Phys. Rev. B* **76**, 064411 (2007). 46, 68
- [107] Fahrenndorf, S. *Single NdPc₂ Molecules on Surfaces: Adsorption, Interaction, and Molecular Magnetism*. Ph.D. thesis (2012). 47, 64, 72, 83, 84, 85
- [108] Noh, J., Murase, T., Nakajima, K., Lee, H. & Hara, M. Nanoscopic investigation of the self-assembly processes of dialkyl disulfides and dialkyl sulfides on Au(111). *J. Phys. Chem. B* **104**, 7411–7416 (2000). 49, 55
- [109] Weidner, T. *et al.* Tripodal binding units for self-assembled monolayers on gold: A comparison of thiol and thioether headgroups. *J. Phys. Chem. C* **113**, 19609–19617 (2009). 50, 51
- [110] Castner, D. G., Hinds, K. & Grainger, D. W. X-ray photoelectron spectroscopy sulfur 2p study of organic thiol and disulfide binding interactions with gold surfaces. *Langmuir* **12**, 5083–5086 (1996). 50
- [111] Ishida, T. *et al.* High-resolution x-ray photoelectron spectra of organosulfur monolayers on Au(111): S (2p) spectral dependence on molecular species. *Langmuir* **15**, 6799–6806 (1999). 50

- [112] Zhong, C.-J. & Porter, M. D. Evidence for carbon-sulfur bond cleavage in spontaneously adsorbed organosulfide-based monolayers at gold. *Journal of the American chemical society* **116**, 11616–11617 (1994). 50
- [113] Zhong, C.-J., Brush, R. C., Andereg, J. & Porter, M. D. Organosulfur monolayers at gold surfaces: reexamination of the case for sulfide adsorption and implications to the formation of monolayers from thiols and disulfides. *Langmuir* **15**, 518–525 (1999). 50
- [114] Tolman, C. A., Riggs, W. M., Linn, W. J., King, C. M. & Wendt, R. C. Electron spectroscopy for chemical analysis of nickel compounds. *Inorg. Chem.* **12**, 2770–2778 (1973). 53
- [115] Matienzo, J., Yin, L. I., Grim, S. O. & Swartz, W. E. X-ray photoelectron spectroscopy of nickel compounds. *Inorg. Chem.* **12**, 2762–2769 (1973). 53
- [116] Gottschalck, J. & Hammer, B. A density functional theory study of the adsorption of sulfur, mercapto, and methylthiolate on Au(111). *J. Chem. Phys.* **116**, 784–790 (2002). 54
- [117] Sexton, B. A vibrational and TDS study of the adsorption of pyrrole, furan and thiophene on Cu(100): Evidence for π -bonded and inclined species. *Surf. Sci.* **163**, 99 – 113 (1985). 54
- [118] Fahrenndorf, S. *et al.* Structural integrity of single bis(phthalocyaninato)-neodymium(III) molecules on metal surfaces with different reactivity. In *SPIN*, vol. 4, 1440007 (World Scientific, 2014). 55, 112
- [119] Zobbi, L. *et al.* Isolated single-molecule magnets on native gold. *Chem. Commun.* 1640–1642 (2005). 55
- [120] Noh, J. & Hara, M. Final phase of alkanethiol self-assembled monolayers on Au(111). *Langmuir* **18**, 1953–1956 (2002). 55
- [121] Huang, L., Zeppenfeld, P., Chevrier, J. & Comsa, G. Surface morphology of Au(111) after exposure to oxygen at high temperature and pressure. *Surf. Sci.* **352**, 285–289 (1996). 56
- [122] Rossel, F., Brodard, P., Patthey, F., Richardson, N. V. & Schneider, W.-D. Modified herringbone reconstruction on Au(111) induced by self-assembled azobenzene islands. *Surf. Sci.* **602**, L115–L117 (2008). 56
- [123] Merz, L. *et al.* Reversible phase transitions in a buckybowls monolayer. *Angew. Chem. Int. Edit.* **48**, 1966–1969 (2009). 57
- [124] Vericat, C. *et al.* Following adsorption kinetics at electrolyte/metal interfaces through crystal truncation scattering: sulfur on Au(111). *Phys. Rev. Lett.* **90**, 075506 (2003). 58

- [125] Biener, M. M., Biener, J. & Friend, C. M. Sulfur-induced mobilization of Au surface atoms on Au(111) studied by real-time STM. *Surf. Sci.* **601**, 1659–1667 (2007). 59
- [126] Lay, M. D., Varazo, K. & Stickney, J. L. Formation of sulfur atomic layers on gold from aqueous solutions of sulfide and thiosulfate: studies using EC-STM, UHV-EC, and TLEC. *Langmuir* **19**, 8416–8427 (2003). 59
- [127] Fang, X., Kögerler, P., Speldrich, M., Schilder, H. & Luban, M. A polyoxometalate-based single-molecule magnet with an $S = 21/2$ ground state. *Chem. Commun.* **48**, 1218–1220 (2012). 60
- [128] Naitabdi, A. *et al.* Grafting and thermal stripping of organo-bimetallic clusters on Au surfaces: Toward controlled Co/Ru aggregates. *Chemistry-A European Journal* **14**, 2355–2362 (2008). 60
- [129] Gradmann, U. & Waller, G. Periodic lattice distortions in epitaxial films of Fe (110) on W (110). *Surf. Sci.* **116**, 539–548 (1982). 61, 62
- [130] Berlowitz, P., He, J.-W. & Goodman, D. Overlayer growth and chemisorptive properties of ultra-thin Fe films on W (110) and W (100). *Surf. Sci.* **231**, 315–324 (1990). 61
- [131] Bethge, H., Heuer, D., Jensen, C., Reshöft, K. & Köhler, U. Misfit-related effects in the epitaxial growth of iron on W(110). *Surface science* **331**, 878–884 (1995). 61, 62
- [132] Bode, M., Pascal, R. & Wiesendanger, R. Scanning tunneling spectroscopy of Fe/W(110) using iron covered probe tips. *Journal of Vacuum Science & Technology A* **15**, 1285–1290 (1997). 61
- [133] Hauschild, J., Elmers, H. & Gradmann, U. Dipolar superferromagnetism in monolayer nanostripes of Fe(110) on vicinal W(110) surfaces. *Phys. Rev. B* **57**, R677 (1998). 61, 63
- [134] Hauschild, J., Gradmann, U. & Elmers, H. Perpendicular magnetization and dipolar antiferromagnetism in double layer nanostripe arrays of Fe(110) on W(110). *Applied physics letters* **72**, 3211–3213 (1998). 61, 64
- [135] Donnay, J. & Ondik, H. Crystal data, vol. ii: Inorganic compounds. *National Bureau of Standards, Washington, DC* (1973). 61
- [136] Mezey, L. & Giber, J. The surface free energies of solid chemical elements: calculation from internal free enthalpies of atomization. *Japanese Journal of Applied Physics* **21**, 1569 (1982). 62
- [137] Przybylski, M., Kaufmann, I. & Gradmann, U. Moessbauer analysis of ultrathin ferromagnetic Fe(110) films on W(110) coated by Ag. *Phys. Rev. B* **40**, 8631 (1989). 62

- [138] Pietzsch, O., Kubetzka, A., Bode, M. & Wiesendanger, R. Real-space observation of dipolar antiferromagnetism in magnetic nanowires by spin-polarized scanning tunneling spectroscopy. *Phys. Rev. Lett.* **84**, 5212 (2000). 64, 83, 84, 85
- [139] Brede, J. *Spin-Polarized Scanning Tunneling Microscopy and Spectroscopy of Phthalocyanine Molecules on Surfaces*. Ph.D. thesis (2011). 64, 78, 83, 84, 85
- [140] Kubetzka, A., Pietzsch, O., Bode, M. & Wiesendanger, R. Spin-polarized scanning tunneling microscopy study of 360° walls in an external magnetic field. *Phys. Rev. B* **67**, 020401 (2003). 64, 72, 73, 109
- [141] Meckler, S. *et al.* Real-space observation of a right-rotating inhomogeneous cycloidal spin spiral by spin-polarized scanning tunneling microscopy in a triple axes vector magnet. *Phys. Rev. Lett.* **103**, 157201 (2009). 64, 65, 66
- [142] Heide, M., Bihlmayer, G. & Blügel, S. Dzyaloshinskii-Moriya interaction accounting for the orientation of magnetic domains in ultrathin films: Fe/W(110). *Phys. Rev. B* **78**, 140403 (2008). 64, 65
- [143] Dzyaloshinskii, I. E. Thermodynamic theory of weak ferromagnetism in antiferromagnetic substances. *Sov. Phys. JETP* **5**, 1259–1262 (1957). 64
- [144] Moriya, T. Anisotropic superexchange interaction and weak ferromagnetism. *Phys. Rev.* **120**, 91–98 (1960). 64
- [145] Meckler, S. *Non-Collinear Magnetism in Fe on W(110)*. Ph.D. thesis (2010). 65
- [146] Ferriani, P. *et al.* Atomic-scale spin spiral with a unique rotational sense: Mn monolayer on W(001). *Phys. Rev. Lett.* **101**, 027201 (2008). 65
- [147] Bode, M. *et al.* Spin-orbit induced local band structure variations revealed by scanning tunnelling spectroscopy. *Journal of Physics: Condensed Matter* **15**, S679 (2003). 66, 73, 109
- [148] Wiesendanger, R. & Bode, M. Nano-and atomic-scale magnetism studied by spin-polarized scanning tunneling microscopy and spectroscopy. *Solid state communications* **119**, 341–355 (2001). 68
- [149] Kubetzka, A., Pietzsch, O., Bode, M. & Wiesendanger, R. Determining the spin polarization of surfaces by spin-polarized scanning tunneling spectroscopy. *Applied Physics A* **76**, 873–877 (2003). 73
- [150] Rico Friedrich, N. A., Vasile Caciuc & Blügel, S. Molecular induced skyhook effect for magnetic interlayer softening. *Phys. Rev. B* **92**, 195407 (2015). 76
- [151] Friedrich, R. private communication. 77, 80
- [152] Mugarza, A. *et al.* Orbital specific chirality and homochiral self-assembly of achiral molecules induced by charge transfer and spontaneous symmetry breaking. *Phys. Rev. Lett.* **105**, 115702 (2010). 78

- [153] Yeganeh, S., Ratner, M. A., Medina, E. & Mujica, V. Chiral electron transport: scattering through helical potentials. *The Journal of chemical physics* **131**, 014707 (2009). 84, 92
- [154] Medina, E., López, F., Ratner, M. A. & Mujica, V. Chiral molecular films as electron polarizers and polarization modulators. *EPL* **99**, 17006 (2012). 92
- [155] Göhler, B. *et al.* Spin selectivity in electron transmission through self-assembled monolayers of double-stranded DNA. *Science* **331**, 894–897 (2011). 92

Acknowledgements

Diese Dissertation ist während meiner dreijährigen Tätigkeit am Peter Grünberg Institut 6 im Forschungszentrum Jülich entstanden. Zum Gelingen der Experimente und der anschließenden Auswertung haben natürlich viele Mitarbeiter des PGI-6 beigetragen.

Zuallererst möchte ich meinem Doktorvater, PD Dr. Daniel Bürgler, meinen herzlichen Dank aussprechen. Daniel, ohne deine unermüdliche Unterstützung hätte ich die Vielzahl an Herausforderungen während dieser Doktorarbeit nicht bewältigen können.

Bei unserem Institutsdirektor, Prof. Schneider, möchte ich mich für die Möglichkeit zur Teilnahme an Konferenzen und für die tolle Ausstattung unseres Labors bedanken. Der Arbeitsalltag wurde auch durch etliche Anekdoten während Kaffeepausen ungemein bereichert.

Prof. Michely möchte ich für seine Tätigkeit als Zweitgutachter danken.

Bei Prof. Kögerler möchte ich mich für die umfangreiche Bereitstellung von $\{\text{Ni}_4\}$ Molekülen sowie einer guten Zusammenarbeit bedanken. Meinen vierwöchigen Aufenthalt an der Iowa State University verdanke ich ebenso Prof. Kögerler.

Dr. Frank Matthes möchte ich für die umfangreiche Unterstützung im Laboralltag und bei meinen Experimenten danken. Insbesondere die konstanten Hinweise die Spitze doch nochmal zu pulsen oder mit höherem Strom zu scannen, führten letzten Endes zu vielen beeindruckenden Bildern. Taner Esat, ebenfalls ein SP-STM Leidensgenosse, hat mich in allen Fragen des Labor- und Experimentalltags sowie mental am Ende meiner Doktorarbeit unterstützt. Samuel Königshofen hat mich ebenfalls bei Experimenten unterstützt, meinen Büroalltag erleichtert sowie meinen Musikgeschmack signifikant erweitert.

Während ich mein erstes Paper schrieb, hat insbesondere Kai Zhu die erfolgreiche Präparation von Fe/W(110) vorangetrieben. Die ersten erfolgreichen SP-STM Experimente zusammen mit Kai waren sehr spannend.

Die Unterstützung in technischen Fragen, insbesondere durch Thomas Jansen, hat erheblich zum Gelingen dieser Doktorarbeit beigetragen. Die technische Unterstützung durch Heinz Pfeifer, Norbert Schnitzler, Bernd Küpper und Jürgen Lauer war ebenso wertvoll.

Am Gelingen der $\{\text{Ni}_4\}$ Experimente hat Dr. Claire Besson signifikanten Anteil. Die für Physiker verständlichen Erklärungen zu Problemen und Konzepten der Chemie waren sehr wichtig. Dr. Kirill Monakhov hat mich beim Verständnis und der Auswertung der $\{\text{Ni}_4\}$ Experimente unterstützt.

Die XPS Messungen am Delta wären ohne die Unterstützung von Dr. Sven Döring und Mathias Gehlmann nicht möglich gewesen.

Das Verständnis des TPT/Fe/W(110) Systems wurde durch die DFT Simulationen von Rico Friedrich, Dr. Vasile Caciuc und Dr. Nicolae Atodiresei signifikant verbessert. Das TPT Projekt geht auf eine Idee von Karthik Raman zurück, dessen kurzer Besuch am PGI-6 auch zum Gelingen dieser Arbeit beitrug.

Allen anderen Mitarbeitern des PGI-6, die mir namentlich hier zu erwähnen nicht möglich ist, möchte ich ebenfalls für die gute Arbeitsatmosphäre, für die zahlreichen Kaffeerunden, Ausflüge und Weihnachtfeiern danken.

Zum Schluss möchte ich auch meinen Eltern und meiner Familie danken, ohne deren Unterstützung ich nicht in der Lage gewesen wäre, diese Doktorarbeit zu verfassen.

Erklärung

Ich versichere, dass ich die von mir vorgelegte Dissertation selbständig angefertigt, die benutzten Quellen und Hilfsmittel vollständig angegeben und die Stellen der Arbeit - einschließlich Tabellen, Karten und Abbildungen -, die anderen Werken im Wortlaut oder dem Sinn nach entnommen sind, in jedem Einzelfall als Entlehnung kenntlich gemacht habe; dass diese Dissertation noch keiner anderen Fakultät oder Universität zur Prüfung vorgelegen hat; dass sie - abgesehen von unten angegebenen Teilpublikationen - noch nicht veröffentlicht worden ist sowie, dass ich eine solche Veröffentlichung vor Abschluss des Promotionsverfahrens nicht vornehmen werde. Die Bestimmungen der Promotionsordnung sind mir bekannt. Die von mir vorgelegte Dissertation ist von PD Dr. Daniel E. Bürgler betreut worden.

Teilpublikationen: V. Heß *et al.*, Adsorption phenomena of cubane-type tetranuclear Ni(II) complexes with neutral, thioether-functionalized ligands on Au(111). *Surf. Sci.* **641**, 210-215 (2015)

Jülich, den 26.11.2015

Curriculum Vitae

Volkmar Heß

Röntgenstraße 4, 52428 Jülich

personal data

birthday 30.07.1987
birthplace Erfurt
marital status single

school

August 1999 – June 2006
Lyonel-Feininger-Gymnasium in Mellinger, Thuringia
final grade: Abitur (1,4)

civilian service

June 2006 – February 2007
assisted transport at Sophien-Hufeland-Klinik in Weimar

university

October 2007 – November 2010 Heinrich-Heine-Universität Düsseldorf
Bachelor Physics, final grade: 1,5
subsidiary subject : computer science
title of bachelor thesis: „Elektronische Regelung für den Ätzprozess von STM-Spitzen“, grade: 1,0

December 2010 – November 2012 HHU Düsseldorf
Master of Science in Physics, final grade: 1,5
specialization: solid state physics, surface and nano physics, magnetism,
title of master thesis: „Oberflächenmodifikation von Gadolinium-schichten durch Wasserstoffabsorption“ (surface modifications of thin Gd films by Hydrogen absorption), grade: 1,3

internships

May 2014
research assistant for 4 weeks at Iowa State University, Ames, IA, USA

working experience

student assistant (SHK):
– Oktober 2010 – February 2011, Institute of Applied Physics:
corrector for exercise sheets in solid state physics lecture
– April 2011 – Juli 2011, Institut für physikalische Grundpraktika:
supervision of students in the experimental courses "physics for medicine students"
– Oktober 2011 – Februar 2012, Institut für physikalische Grundpraktika:
supervision of students in the experimental course "physics for biology students"

PhD student: January 2013 – December 2015
Peter-Grünberg-Institut 6, Forschungszentrum Jülich
– fundamental research on surface nano physics and magnetism